공학박사 학위논문

Multifunctional Inorganic Nanoparticles for Modulation of Hypoxic Inflammatory Microenvironments

저산소 염증성 미세환경의

조절을 위한 다기능성

무기나노입자에 관한 연구

2019년 2월

서울대학교 대학원

화학생물공학부

김 종 훈

Abstract

Multifunctional Inorganic Nanoparticles for Modulation of Hypoxic Inflammatory Microenvironments

Jonghoon Kim
School of Chemical and Biological Engineering
The Graduate School
Seoul National University

Due to their unique physicochemical properties, inorganic nanoparticles (NPs) have emerged as novel imaging, diagnostic, and therapeutic agents for the future biomedical field. In particular, hypoxic inflammatory microenvironments, which is often found at disease sites in the body, can be easily controlled using inorganic NPs with various combinations. Catalytic inorganic NPs continuously generate oxygen

using intracellular hydrogen peroxide in the hypoxic microenvironment. They can also control the phenotype of macrophages in the inflammatory microenvironment, alleviating the inflammation in inflamed tissues. Moreover, immune cell can be targeted using the NPs functionalized with targeting moieties, enabling the delivery of the functional NPs to inflammatory microenvironments. This thesis describes the applications of multifunctional inorganic NPs for modulation of hypoxic and inflammatory microenvironments.

Firstly, biocompatible manganese ferrite NP-anchored mesoporous silica NPs (MFMSNs) were designed to overcome hypoxia, consequently enhancing the therapeutic efficiency of photodynamic therapy (PDT). By exploiting the continuous oxygen-evolving property of manganese ferrite NPs through the Fenton reaction, MFMSNs relieve hypoxic condition using a small amount of NPs and improve therapeutic outcomes of PDT for tumors *in vivo*. In addition, MFMSNs exhibit T_2 contrast effect in magnetic resonance imaging (MRI), allowing *in vivo* tracking of MFMSNs.

Secondly, manganese ferrite and ceria NP-anchored mesoporous silica NPs (MFC-MSNs) that can synergistically scavenge reactive

oxygen species (ROS) and produce oxygen for M1 macrophage reduction and M2 macrophage induction for rheumatoid arthritis (RA) treatment. MFC-MSNs exhibited a synergistic effect on O_2 generation attributed to hydroxyl complementary reaction of ceria NPs scavenging the intermediate hydroxyl radical generated by manganese ferrite NPs during the Fenton reaction in the process of O_2 generation, leading to efficient polarization of M1 to M2 macrophages both *in vitro* and *in vivo*. Intra-articular administration of MFC-MSNs to RA-suffering rats alleviated hypoxia, inflammation, and pathological features in the joint.

Finally, click reaction-assisted immune cell targeting (CRAIT) strategy was developed to deliver drug-loaded NPs into tumor interiors. Immune cell-targeting CD11b antibodies are modified with *trans*-cyclooctene to enable biorthogonal click chemistry with mesoporous silica NPs with tetrazines (MSNs-Tz). Sequential injection of modified antibodies and MSNs-Tz at intervals of 24 h results in targeted conjugation of the NPs onto CD11b+ myeloid cells, which serve as active vectors into tumor interiors. It was shown that the CRAIT strategy allows deep tumor penetration of drug-loaded NPs, resulting in enhanced therapeutic efficacy in an orthotopic 4T1 breast tumor model.

Keywords: nanoparticle, drug delivery, cancer, tumor hypoxia, click chemistry, nanomedicine

Student Number: 2013-22521

Contents

List of Figures

Chapter 1. Introduction: Multifunctional Inorganic Nanoparticles and Their Applications in Hypoxic Inflammatory Microenvironments

1.1 Introduction

Nanotechnology have emerged as one of the most important technologies, covering a variety of fields including physics, chemistry, material science, engineering, and biomedical field. The unique physicochemical properties of NPs, such as long circulation time, facile functionalization, and size-dependent properties, that cannot be found in bulk materials facilitate the application to various biomedical fields.[1] Among various nanostructured materials, inorganic nanoparticles (NPs) have been extensively studied for biomedical applications due to their intrinsic unique physicochemical properties. The combinations of

various functional NPs with different properties, functional molecules, and targeting agents offer synergistic multifunctional medical platforms, increasing the accuracy of diagnosis via multimodal imaging and theranosis that refers to the simultaneous diagnosis and therapy.[2] While a conventional molecular contrast agent is appropriate only for a single imaging modality, multimodal imaging is available by multifunctional NPs. Moreover, multifunctional NPs can be employed as a therapeutic agent for various diseases using their physical properties or endowing them with drug carrying ability.[3] Indeed, these multifunctional inorganic NPs increase the accuracy of diagnosis and reduce the side effects of therapeutics.

Hypoxic inflammatory microenvironment is a common hallmark at a disease site such as tumor and inflammatory diseases.[4] In particular, tumor microenvironment, which refers to the cellular environment in tumor, is highly hypoxic due to the poor oxygen supply to the interior part of tumor.[5] Tumor hypoxia plays an important role in tumorigenic processes such as angiogenesis and metastasis, secreting hypoxia-inducible factor (HIF) family. Angiogenesis, which is the formation of new blood vessels in tumor, is promoted by HIF family under hypoxic tumor microenvironments.[6] Since blood vessels in tumor is an escape

route for cancer cells toward other tissues in the body, hypoxia also promotes tumor metastasis. The expression of HIF family increases the metastasis and decrease the survival rate in tumors. Moreover, inflammatory cells, including macrophages, dendritic cells, myeloid-derived suppressor cells (MDSCs), and T cells, are recruited to tumor and play a role in accelerating tumor growth and metastasis.[7] As well as tumor microenvironments, macrophages play a crucial role in innate and adaptive immunity at the early stage of various inflammatory diseases.[8]

Multifunctional inorganic NPs can modulate various kinds of hypoxic inflammatory microenvironments. For example, tumor hypoxia can be attenuated using NPs for enhanced cancer therapy.[9] Different mechanisms are applicable to ameliorate tumor hypoxia using functional NPs, including improving blood flow into tumors, shuttling oxygen molecules into tumors, and generating O_2 molecules using catalytic NPs. The macrophage phenotype in inflammatory microenvironments can be also controlled by O_2-evolving and ROS-scavenging NPs. In addition, modifying the NPs with leukocyte-targeting ligands, inflammatory microenvironments can be targeted by drug-loaded NPs.

1.2 Overview of Multifunctional Inorganic Nanoparticles

Facile modification of NPs allows to develop multifunctional NPs.[10] While a traditional molecular contrast agent can be detected by single imaging modality, multifunctional NPs enable multimodal imaging. Simultaneously, the NPs can be used as therapeutic agents via employing their unique physical properties or endowing with drug delivery capability. The multifunctional NPs not only increase accuracy of diagnosis but also reduce the side effect of drugs. The multifunctionality can be achieved by combining different types of nanomaterials, functional molecules, and targeting agents. In this section, several recent examples of multifunctional NPs for multimodal imaging and theranosis will be introduced.

1.2.1 Multifunctional Inorganic Nanoparticles for Multimodal Imaging

Because each imaging modality has its own strength and weakness, multimodal imaging is required to increase the accuracy of diagnosis by obtaining complementary information from each imaging modality. Indeed, some NPs have intrinsic properties suitable for several imaging modalities. For instance, Gd_2O_3 NPs can be used for magnetic resonance imaging (MRI) and computed tomography (CT) owing to high X-ray attenuation coefficient and large number of unpaired electrons of gadolinium ion.[11] Lanthanide-based upconversion NPs have been studied for multimodal imaging agents including MRI and optical imaging.[12] The unique optical property of gold NPs allows photoacoustic tomography (PAT) as well as CT.[13] The most general method to prepare multifunctional NPs is the conjugation of functional molecules. For example, iron oxide NPs conjugated with optical or radioisotopes have been exploited for multimodal imaging including MRI/optical imaging or MRI/nuclear imaging.[14-15]

The contrast effect can be controlled either by assembly of NPs or formation of core/shell structures. For example, assembly of multiple iron oxide NPs on the surface of silica NPs enhances T_2 MRI contrast

effect.[16] Although sensitivity of MRI can be enhanced by contrast agents, it can be affected by several artifacts such as calcification, blood clots, and air bubbles. However, this can be overcome by self-confirmation using T_1-T_2 dual mode MRI contrast agents, which can be prepared by controlling the thickness of silica layer between magnetic nanoparticle and paramagnetic shell.[17] (**Figure 1.1a−1.1d**).

Since each imaging modality has different sensitivity, the ratio of related contrast agents should be optimized so that they can be detected by any modality. This is critical when preparing contrast agents for CT which requires very high dose. For example, gadolinium-complexes can be used for MRI and CT. However, because too high concentration of T_1 contrast agent suppresses its contrast effect, simultaneous imaging of MRI and CT using gadolinium-chelates is almost impossible.[18] To address this limitation, Fe_3O_4/TaO_x core/shell NPs and gold NPs coated with gadolinium chelates are proposed (**Figure 1.1e**).[19-20] These multifunctional imaging agents clearly delineate tumor-associated vessels and tumor microenvironment.

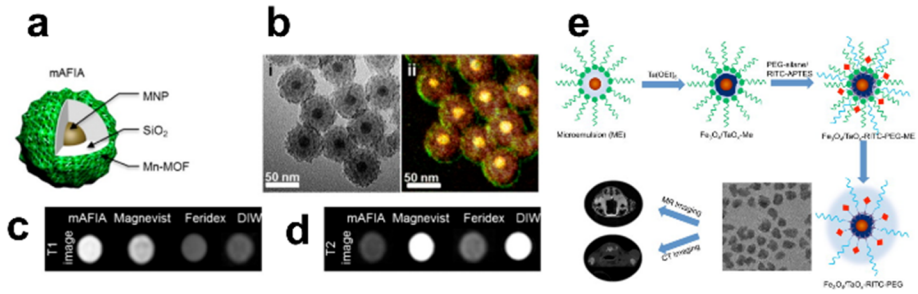

Figure 1.1 (a) Illustration of $Zn_{0.4}Fe_{2.6}O_4$/Mn-MOF core/shell NP (mAFIA). (b) (i) TEM image and (ii) energy dispersive X-ray spectroscopy (EDX) analysis of mAFIA. (c) T_1 and (d) T_2-weighted images of mAFIA compared with conventional MRI contrast agents. (e) Schematic illustration of RITC-doped Fe_3O_4/TaO_x core/shell NP for MRI/CT dual-modal imaging. (a~d) from Ref. [17] and (e) from Ref. [19].

1.2.2 Multifunctional Inorganic Nanoparticles for Theranosis

While traditional imaging and therapeutic agents generally perform single role, synergistically integrated NPs can be used for simultaneous therapy and diagnosis.[21] There are two approaches for therapeutic applications of NPs. The first is to use intrinsic properties of NPs. For example, magnetic NPs generate heat under alternating external magnetic field to induce cell death, referred to as magnetic hyperthermia.[22] On the other hand, gold nanostructures including gold nanorod,[23] nanoshell,[24] and nanocage[25] are employed in photothermal therapy (PTT), which involves NIR irradiation to induce thermal damage to tumor cells (**Figure 1.2a−1.2c**). [26] The efficiency of magnetic hypethermia is significantly enhanced by controlling size, composition, and structure of NPs.[27] Apart from gold NPs, various nanomaterials such as carbon nanotubes,[28] graphene,[29] CuS[30] NPs can efficiently convert absorbed NIR light into heat. In addition to heat generation, carbon- or titania-based nanomaterials can generate reactive oxygen species (ROS), which destroys cancer cells and blood vessels around tumor (**Figure 1.2d−1.2g**).[31-33]

The second approach is to use NPs as delivery vehicles. Owing to long circulation time and targeting capability, NPs increase delivery efficiency and decrease side effects of free drug such as nonspecific distribution. NPs can be developed as delivery carrier simply by conjugation of therapeutic agents on the surface of the NPs. For example, QD-aptamer-doxorubicin conjugates are used for intracellular drug delivery and synchronous fluorescence imaging.[34] To increase the therapeutic effect, cleavable linkers such as disulfide bond are often used.[35] However, since the conjugated molecules are exposed, they can be degraded in prior to reaching the target site. Because the pore can protect the therapeutic cargos, mesoporous silica NPs with high porosity and large surface area have been used as drug delivery vehicle.[36] Owing to facile functionalization with silane agents, various functional moieties including fluorescence dye and NPs are readily incorporated into the mesoporous silica NPs. For example, core-shell NPs, which are composed of a single iron oxide NP core and a dye-doped mesoporous silica shell, have been used not only as magnetic resonance and fluorescence imaging agents, but also as drug delivery vehicle.[37] In addition, the drug release can be controlled either via grafting stimuli-responsive functional groups or via inducing supramolecular change of

gatekeeper groups.[38] In addition to mesoporous silica NPs, polymers have been developed as delivery carriers for a long time. Although a polymer itself does not have imaging capability, incorporation of NPs allows to monitor its delivery. Since a number of NPs prepared via thermal decomposition method are hydrophobic, they can be easily incorporated within hydrophobic polymers such as ploy(lactic-co-glycolic) acid (PLGA).[39]

These two approaches are sometimes combined, resulting in synergetic therapeutic effect. For example, photodynamic therapy (PDT) uses light-sensitive photosensitizers to generate ROS. However, most photosensitizers absorb visible light, but its penetration depth is limited. Because NPs can emit visible light through multiphoton or upconversion process, a deep penetrating NIR light can be used in PDT.[40] In addition, mild heat generation by NPs increases permeability of tumor vessels, which also enhances delivery efficiency of drugs.[41]

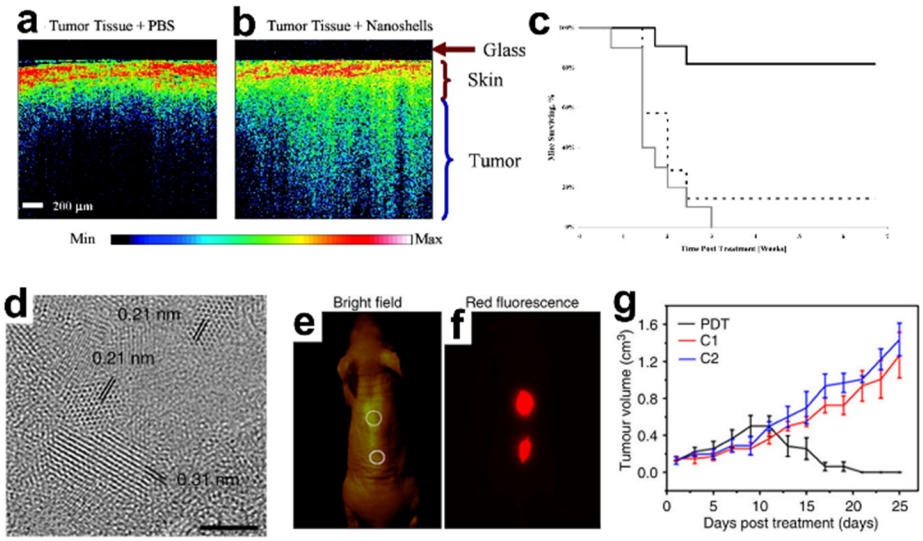

Figure 1.2 OCT images from tumors of mice intravenously administered with (a) PBS or (b) gold nanoshells. (c) Survival data from the treated groups of gold nanoshell + NIR irradiation (solid black line), PBS sham + NIR laser treatment (dashed black line), and untreated control (gray line). (d) High-resolution TEM image of graphene quantum dots (GQDs). Scale bar, 2 nm. (e) Bright-field image and (f) red-fluorscence image after subcutaneous injection of GQDs in different areas (ex/em = 502-540/695-775). (g) Time-dependent tumor growth curves (n=5) after PDT treatment compared with control groups (C1: not irradiated group, C2: not GQD-administered group). (a~c) from Ref. [26] and (e~g) from Ref. [33].

1.3 Multifunctional Inorganic Nanoparticles for Modulation of Hypoxic Inflammatory Microenvironments

1.3.1 Hypoxic Tumor Microenvironments

The tumor microenvironment refers to the cellular environment where the tumor exists. It is composed of surrounding blood vessels, fibroblasts, immune cells, bone marrow-derived inflammatory cells, lymphocytes, and extracellular matrix (ECM).[42] Tumors can affect the microenvironment by releasing extracellular signal molecules, and inducing tumor angiogenesis and immune tolerance. Since tumors are surrounded by ECM and stromal cells, the components in tumor microenvironment play a crucial role in regulation of the various tumorigenic processes, including initiation, progression, and metastasis.[43] Interestingly, tumor microenvironment helps protecting against tumorigenesis and invasion in a healthy state, but it leads to tumorigenesis by contrast in a not healthy state.

One of the major characteristics of tumor environment is hypoxia.[5] As the tumor grows quickly, the oxygen supply to the interior part of tumor is not sufficient, resulting in tumor cell oxygen deficiency, which is called tumor hypoxia. Hypoxic conditions in tumor induce gene

expressions which are associated with various hallmarks of tumorigenesis including cell proliferation, cell adhesion, and extracellular matrix production, resulting in genetic instability by inhibiting DNA repair mechanisms. Hypoxia-inducible factor (HIF) family, including HIF-1, HIF-2, and HIF-3, is largely associated with these mechanisms (**Figure 1.3**).[6] HIF-1, HIF-2, and HIF-3 proteins regulate cellular processes such as cell proliferation, glucose metabolism, angiogenesis, and tissue remodeling in a low oxygen environment. In particular, HIF-1α is a representative protein included in HIF family, which is mainly associated with the activation of metastasis and angiogenesis.[44] Under normal oxygen conditions, two proline residues in HIF-1α are hydroxylated in the presence of oxygen by prolyl-5-hydroxylase domain-containing proteins (PHDs) group, promoting binding to von Hippel-Lindau tumor suppressor (pVHL) and subsequent degradation of HIF-1α. On the other hand, HIF-1α proteins are not degraded under hypoxic conditions, regulating various cellular processes in tumor tissue.

As described above, tumor hypoxia is largely associated with angiogenesis which is a critical step in tumorigenesis.[6] Tumor angiogenesis refers to the formation of new blood vessels, which can

provide nutrients and oxygen to the tumor, from pre-existing blood vessels. Since cancer cells lost their ability to divide in a controlled manner, they need a large amount of blood supply to obtain the nutrients and oxygen. HIF-1α promotes the angiogenesis under hypoxic tumor microenvironments, inducing the secretion of pro-angiogenic factors, such as vascular endothelial growth factor (VEGF), fibroblast growth factor (FGF), platelet-derived growth factor (PDGF), and angiopoietin 2 (Ang-2).[42] The activity of angiogenic inhibitors, including thrombospondin, is also simultaneously decreased by HIF-1α.

New blood vessels in tumor play a crucial role as an escape route for cancer cells toward distant sites in the body, hypoxia is also strongly linked to the promotion of tumor metastasis.[43] Heterogeneous and permeable vasculature enable tumor cells to extravasate, circulate, and relocate to tissues. The expression of the HIF-1 and HIF-2 increases distant metastasis and poor survival rate in various tumor types, affecting the invasive and migratory property of cancer cells. Epithelial-to-mesenchymal transition (EMT), which refers to a trans-differentiation of cancer cells to obtain mobile and plastic abilities, usually occurs before the migration of cancer cells.[45] Hypoxia regulates the gene expression related to EMT by decreasing the epithelial-associated gene expression,

including E-cad, β-catenin, and increasing the mesenchymal-associated gene expression, including N-cad, CXCR4, vimentin, and SMA.[44] Besides HIF family, inhibition of CA9 protein, which is a hypoxia-inducible enzyme present in tumor, leads to the decrease in tumor growth and metastasis.[46] Likewise, a strategy targeting hypoxic cells has been extensively developed to reduce metastasis.

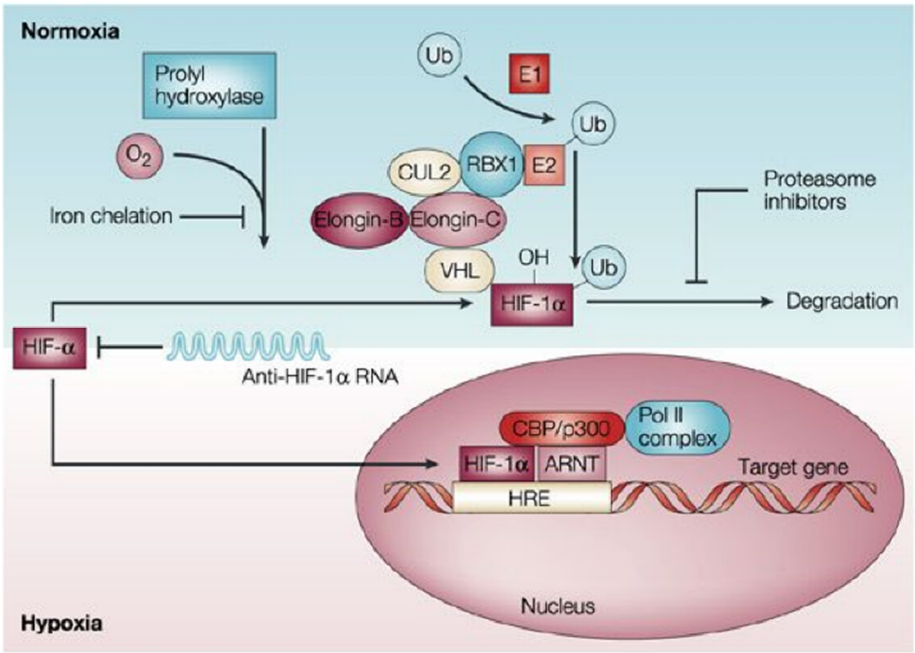

Figure 1.3 HIF-1 pathway under normoxic and hypoxic conditions. In the presence of O_2, prolyl hydroxylase modifies HIF-1α and allows it to interact with VHL complex. The ubiquitylation (Ub) modification targets HIF-1α for degradation, which can be blocked by proteasome inhibitors. However, in the absence of O_2, prolyl hydroxylase cannot modify HIF-1α, allowing it remains stable. Reproduced from Ref. [5].

1.3.2 Modulation of Hypoxic Tumor Microenvironments for Enhanced Cancer Treatment

Due to the extremely rapid growth of tumor cells and poor development of new blood vessels, the interior of tumors is lack of sufficient oxygen supply. Tumor hypoxia is one of the major hurdles in cancer therapy where oxygen plays an important role, such as chemotherapy, radiotherapy, and photodynamic therapy (PDT).[9] Chemotherapy is a type of cancer treatment that uses an anticancer drug such as doxorubicin. The therapeutic outcomes of doxorubicin are remarkably limited in a hypoxic microenvironment with poor vasculature and low vascular density.[47] In addition, HIF-1α overexpression results in upregulation of multidrug resistance related proteins (MRPs).[48] Radiotherapy is also widely applied cancer treatment method, in which oxygen is a crucial sensitizer for radiation-induced tumor cell destruction.[49] Since PDT involves the generation of cytotoxic singlet oxygen from oxygen molecules, oxygen concentration highly affects the efficiency of PDT. Recently, functional NPs for overcoming tumor hypoxia have been developed as a unique strategy to achieve enhanced efficiency of various cancer therapies.[9] Different mechanisms have been proposed to ameliorate tumor hypoxia with NPs,

including improving blood flow into tumors by decompressing the blood vessels with drugs, directly increasing the tumor oxygenation status by shuttling oxygen molecules into tumors with oxygen nanocarriers, and *in situ* oxygen generation through decomposing endogenous hydrogen peroxide by catalytic NPs. In this part, recent strategies using different mechanisms for overcoming tumor hypoxia will be introduced.

Increasing the local temperature of tumor cells by hyperthermia can effectively increase the blood flow into tumors, subsequently leading to enhanced tumor oxygenation. Core-shell structured MnSe@Bi_2Se_3 NPs were developed and applied for efficient photothermal therapy (PTT) and radiotherapy (**Figure 1.4**).[50] PTT is one of the cancer treatment method which involves cancer hyperthermia ablation by photosensitizers converting energy from near infrared (NIR) light to heat. Since mild PTT for tumors is favorable for tumor hypoxia relief, MnSe@Bi_2Se_3 NPs were employed as PTT agents and radiosensitizers simultaneously for reducing tumor hypoxia via improving tumor blood flow. The therapeutic effect of radiotherapy was significantly improved after NP mediated PTT. Moreover, antiangiogenic drugs, such as cyclophosphamide, gemcitabine, and taxane, can normalize the vascular structure of tumors, allowing the enhanced intratumoral delivery of

oxygen.[51] It is reported that paclitaxel (PTX) was attached to ^{131}I-labeled human serum albumin (HSA), leading to increased local oxygen level and suppressed hypoxia after the NPs were administered via intravenous injection.[52]

Another strategy is directly delivering oxygen into tumors by NP-based vehicles. Hemoglobin-based oxygen carriers have been proposed to increase the oxygen transport efficiency. Wang et al. reported that hemoglobin-conjugated photosensitizer, zinc phthalocyanine (ZnPc), encapsulated into polymeric micelles exhibit significantly enhanced PDT efficiency due to their oxygen self-compensating ability of hemoglobin.[53] Moreover, perfluorocarbon (PFC)-based nanomaterials have been investigated for an efficient oxygen delivery vehicle.[54] Since PFCs exhibit excellent biocompatibility and high oxygen solubility, they have been used as an ultrasound and MRI contrast agent in clinics. Recently, many researchers employed PFCs as an oxygen carrier for enhanced cancer treatment. Cheng et al. developed oxygen self-enriching PFC nanodroplets loaded with photosensitizers for PDT (**Figure 1.5a−b**).[55] Reduced therapeutic efficiency of PDT due to low oxygen concentration was enhanced by oxygen-adsorbed PFC nanodroplets. They also designed PFCs encapsulated into HAS shell

with photosensitizers for reduced self-quenching effect of photosensitizers and enhanced therapeutic efficiency of PDT.[56] Although PFCs show excellent oxygen capacity, oxygen should be easily released in tumor tissue for efficient oxygenation. Song et al. reported PFC-loaded hollow Bi_2Se_3 NPs for burst oxygen release under NIR irradiation due to the photothermal effect of the NPs.[57] Burst release of oxygen facilitates greatly improved tumor oxygenation and enhanced radiotherapy. In addition, they reported HSA-stabilized PFC nanodroplets for excellent oxygen solubility and ultrasound-triggered oxygen release.[58] In in vivo study, it was demonstrated that PFC nanodroplets adsorbed oxygen in the lung and transported oxygen to tumor, followed by oxygen release under ultrasound exposure.

In situ oxygen generation using catalytic NPs is an emerging strategy for tumor oxygenation. H_2O_2 plays a crucial role in various physiological processes, including cell growth and proliferation, it is one of the most abundant metabolite in tumor microenvironment.[59] Therefore, tumor hypoxia could be readily relieved by converting intracellular H_2O_2 to oxygen molecules using various kinds of catalytic NPs. Chen et al. designed a H_2O_2-activatable oxygen evolving NPs for highly efficient PDT under hypoxic conditions (**Figure 1.5c**).[60] In this

system, catalase and photosensitizers were encapsulated into the black hole quencher-3 (BHQ-3) doped PLGA shell. Intracellular H_2O_2 was catalyzed by catalase to generate oxygen, followed by the destruction of PLGA particles and release of photosensitizer molecules. Consequently, the therapeutic efficiency of PDT was markedly enhanced by hypoxia relief. Song et al. synthesized catalase-loaded hollow tantalum oxide NPs showing efficient tumor accumulation after intravenous administration.[61] When the NPs accumulated in tumor, endogenous H_2O_2 was decomposed to H_2O and O_2, increasing the therapeutic outcomes of radiotherapy. Huang et al. developed implanted oxygen-generating depot composed of CaO_2 and catalase to enhance the cytotoxicity of doxorubicin against malignant tumor tissues.[47] The *in situ* oxygen-generating depot effectively alleviated the hypoxia in tumor tissues and increased the chemotherapeutic effect of doxorubicin. Moreover, MnO_2 NPs have been extensively studied as an efficient oxygen generating material with high reactivity toward H_2O_2. Prasad et al. synthesized MnO_2 NPs and conjugated them with bovine serum albumin (BSA) for colloidal stability and biocompatibility.[62] BSA-conjugated MnO_2 NPs enabled obvious tumor oxygenation by catalyzing endogenous H_2O_2, consequently reducing the tumor growth after

radiotherapy. Zhu et al. also synthesized MnO_2 NPs conjugated with photosensitizer Ce6 molecules.[63] Similarly, the H_2O_2 decomposition and O_2 generation result in improved PDT even at a largely reduced dosage.

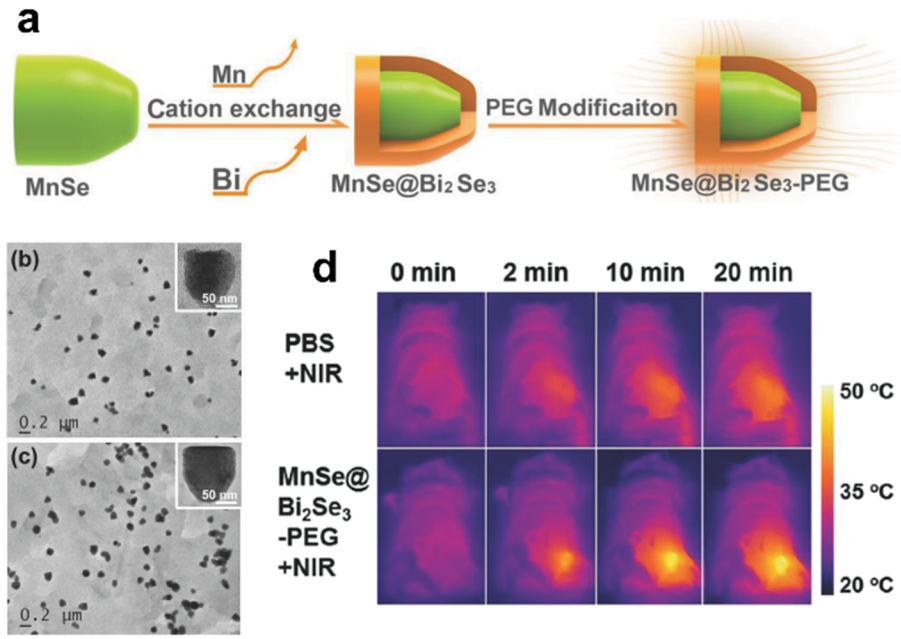

Figure 1.4 (a) A schematic illustration showing the synthesis of $MnSe@Bi_2Se_3$ core-shell nanostructure by cation exchange and PEG coating. TEM images of (b) MnSe NPs and (c) $MnSe@Bi_2Se_3$ NPs. (d) IR thermal images of 4T1 breast tumor-bearing mice after treatment of PBS or $MnSe@Bi_2Se_3$ NPs under the 808 nm laser irradiation. Reproduced from Ref. [50].

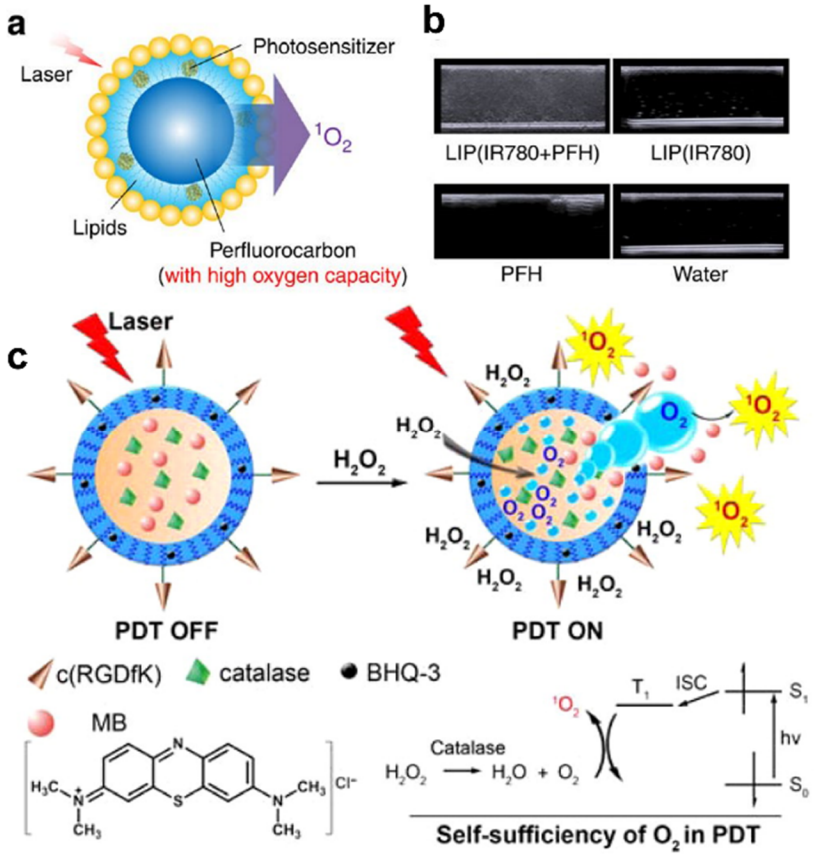

Figure 1.5 (a) Design of the Oxy-PDT agent. Perfluorocarbon (PFC) and photosensitizer are encapsulated by lipids. (b) Ultrasound images of the Oxy-PDT agent and other control groups. (c) Mechanism of H_2O_2-activatable release of photosensitizer and oxygen for improved PDT. (a~b) from Ref. [55] and (c) from Ref. [60].

1.3.3 Macrophage Phenotype Modulation in Inflammatory Microenvironments

Macrophages refer to phagocytic cells which engulf and digest foreign substances, cellular debris, and dead cells in a process called phagocytosis.[8] They could be found in most of tissues due to the potential pathogens, existing as various forms, including Kupffer cells, alveolar macrophages, microglia, and others. In the early stage of inflammation, neutrophils are recruited to the inflamed site, stimulating the appearance of the macrophages and make them digest the neutrophils after several hours.[64] The dying or dead cells are handled by fixed macrophages, which are located in the major organs, including lung, liver, bone, spleen, neuronal tissue, and connective tissue. The macrophages as various forms ingest foreign substances and recruit additional macrophages. Besides phagocytosis, macrophages play a crucial role in innate and adaptive immunity in the body by recruiting other immune cells. They can act as an antigen presenter to activate T cells, which plays a key role in initiating an immune response. After a pathogen was digested by macrophages, the macrophages present the antigen of the pathogen to the corresponding helper T cells. They integrate the antigen into the cell membrane and display it attached to MFC class II (MHC-II)

molecules. Consequently, the antigen presentation enables the production of antibodies, which facilitates the adhesion to macrophages with their cell membrane and phagocytose.

Macrophages exist in two different subtypes with pro-inflammatory M1 macrophages and anti-inflammatory M2 macrophages.[65] M1 macrophages can be activated by lipopolysaccharide (LPS) and IFN-γ and secrete pro-inflammatory cytokines such as IL-12 and IL-10, exhibiting pro-inflammatory, bactericidal, and phagocytic functions. On the other hand, M2 macrophages play a role in constructive processes such as tissue repair and wound healing, producing anti-inflammatory cytokines including IL-10. They are the phenotype of resident tissue macrophages and tumor-associated macrophages. While M1 macrophages are the dominating phenotype in the early stage of inflammation, the ratio of M2 macrophages increases and that of M1 macrophages decreases as the wound ages.[66] M2 macrophages are necessary for production of collagen, revascularization, and reepithelialization at the wound site. Therefore, a strategy has been proposed for the treatment of various inflammatory diseases and cancer using macrophage polarization from M1 to M2 phenotype or from M2

to M1 phenotype. In this part, recent researches using macrophage polarization for various diseases will be introduced.

Macrophage have been emerged as a potential target for the treatment of various inflammatory diseases. Using NPs to control macrophages has a great therapeutic potential in treatment of the diseases. For example, Harel-Adar et al. developed microparticles to target macrophages in cardiac tissue in patients with myocardial infarction.[67] They proposed a new strategy to stimulate M2 polarization by mimicking the natural process of efferocytosis that refers to a phagocytosis of apoptotic cells triggering M1 to M2 transition. Furthermore, Kwon et al. designed IL-4 loaded mesoporous silica NPs with extra-large pores (XL-MSNs) for macrophage polarization by *in vivo* cytokine delivery.[68] They synthesized mesoporous silica NPs with 30 nm-sized pores due to the large-sized proteins like IL-4. IL-4 loaded XL-MSNs were successfully degraded *in vivo* and polarized the macrophages to anti-inflammatory M2 phenotype. Recently, ceria NPs have been studied for M2 polarization by eradicating ROS in various inflammatory disease models. Zeng et al. reported that ceria NPs show a neuroprotective effect by modulating phenotypic polarization of the microglia (**Figure 1.6a−d**).[69] Since ROS is largely associated with the phenotype of

macrophages, ceria NPs can scavenge multiple ROS with high efficiency and polarize from a pro-inflammatory phenotype to an anti-inflammatory phenotype.

In tumor microenvironments, tumor-associated macrophages (TAMs) exist primarily as anti-inflammatory M2 phenotype, facilitating the tumor development with immune suppression, angiogenesis, and metastasis.[7] Therefore, the polarization of TAMs from M2 phenotype to M1 phenotype can alleviate anti-tumor immunity to promote tumor growth and progression. To date, several strategies have been proposed to alter the polarization of TAMs to inhibit tumor growth. Song et al. developed hyaluronic acid-modified manganese dioxide NPs for simultaneous producing O_2 and reprogramming pro-tumoral M2 TAMs to anti-tumoral M1 macrophages, allowing efficient cancer treatment (**Figure 1.6e**).[70] The hyaluronic acid-coated, mannan-conjugated MnO_2 NPs successfully increased tumor oxygenation and polarized the phenotype toward M1 macrophages. Parayath et al. designed CD44-targeting hyaluronic acid-poly(ethyleneimine) (HA-PEI)-based NPs encapsulating miR-125b for TAM-specific delivery and transfection.[71] They demonstrated that intraperitoneal administration of HA-PEI NPs

increases in the M1 to M2 macrophage ratio in lung tumor tissue, showing an excellent potential in anticancer immunotherapy.

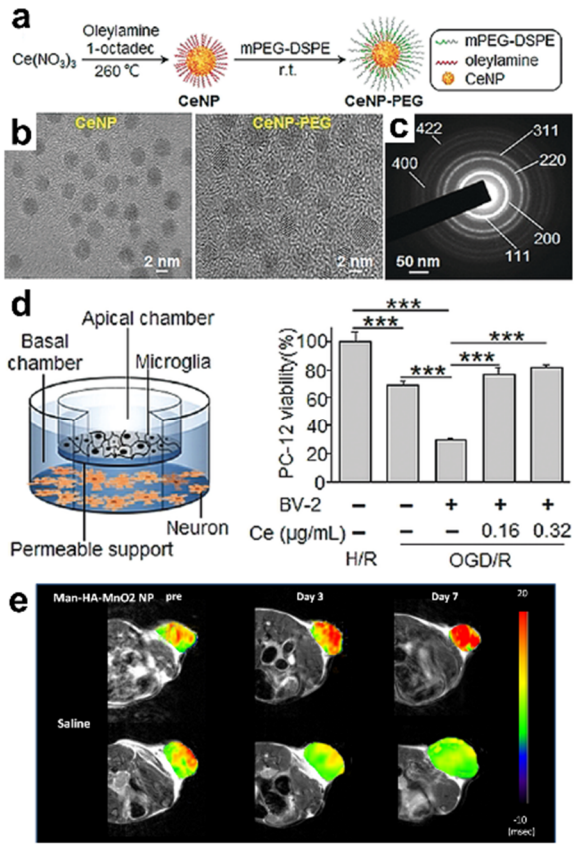

Figure 1.6 (a) Synthetic procedure of CeNP-PEG. (b) TEM images of CeNP and CeNP-PEG. (c) SAED images of the CeNPs showing the cubic fluorite crystal structure. (d) Diagram of microglia cells and neuron-like PC-12 cells co-cultured in a transwell dish, and cell viability test of PC-12 cells after CeNP-PEG treatment to microglia cells. (e) Increased T_2^* values of tumor after treatment of Man-HA-MnO_2 NPs, showing the effect of Man-HA-MnO_2 NPs on tumor oxygenation. (a~d) from Ref. [69] and (e) from Ref. [70].

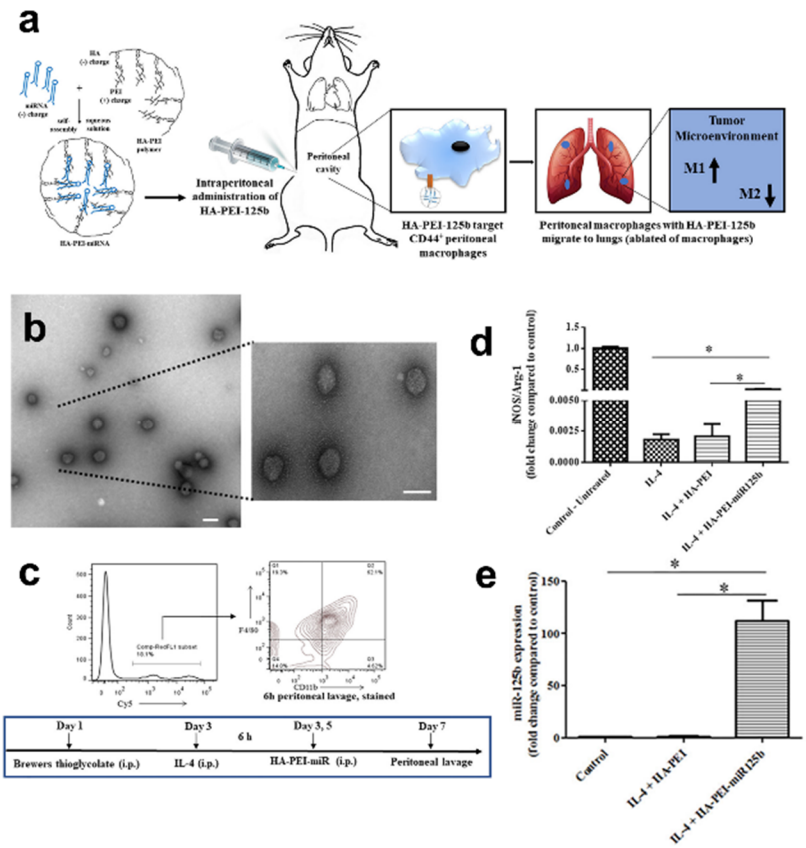

Figure 1.7 (a) Schematic illustration showing the uptake of HA-PEI/miR NPs by peritoneal macrophages inducing the repolarization of TAMs in the lung tumor tissue. (b) TEM image of HA-PEI/miR NPs. Scale bar, 100 nm. (c) FACS analysis of cells stained with F4/80 and CD11b antibodies. (d) In vivo polarization of peritoneal macrophages treated with HA-PEI NPs, as determined by qPCR analysis. (e) miR-125b expression level in peritoneal macrophages treated with HA-PEI NPs. Reproduced from Ref. [71].

1.3.4 Inflammatory Cell Recruitment in Inflammatory Tumor Microenvironments

Another major characteristic of the tumor microenvironment is inflammation.[7] In normal pathological processes such as wound healing and infection, various kinds of cytokines involved in the process initiate and maintain a host response to heal the inflamed tissue. It involves the recruitment and activation of leukocytes such as neutrophils, monocytes, and eosinophils, to the damaged sites. However, dysregulation of this process results in dysfunction of inflammatory system and tumorigenesis from the sites of inflammation, infection, and chronic irritation. Inflammation in cancer involves different factors that is observed in typical inflammatory responses, including an influx of pro-inflammatory cytokines, cytotoxic mediators, proteases, MMPs, and interleukins.[4] In addition, TAMs produce pro-angiogenic growth factors, such as VEGF, and tumor cells produce various cytokines recruiting inflammatory cells for tumorigenic growth and metastasis.[42]

Since tumors often occur at sites of chronic inflammation, various kinds of leukocytes, including macrophages, dendritic cells, myeloid-derived suppressor cells (MDSCs), and T cells, are infiltrated to the tumor microenvironment. Although these myeloid-monocytic cells have

similar morphology, their cellular effectors are functionally heterogeneous and play important roles in accelerating tumor growth and metastasis.[72] Anti-inflammatory M2 macrophages downregulate inflammatory responses, induce neoangiogenesis, and promote parasitic encapsulation, contributing to tumor growth and metastasis.[73] Dendritic cells are more effective than macrophages in activating a naïve T cells and thus are called professional antigen presenting cells (APCs). Since they have immunoregulatory properties and the potential for providing therapeutic activity, the suppression of dendiritic cells in tumor microenvironments leads to the limited response to immunotherapy in cancer patients. As well as dendritic cells, MDSCs can also inhibit T cell activation by anti-CD3 and superantigen. The mechanism of MDSC immunosuppression involves the ROS upregulation, NO generation, L-arginine metabolism, and immunosuppressive cytokines.[74] However, tumor infiltrating T cells are closely associated with a positive prognosis, a high frequency of infiltrating T cells is not always beneficial to tumor suppression. The type of T lymphocytes is also a critical factor for a positive outcome for antitumor property.

As described above, various kinds of immune cells are recruited to the tumor microenvironments at the early stage of tumorigenesis.

Therefore, targeting inflammatory cells has been a novel strategy to treat malignant cancers. To date, many strategies have been proposed that utilizing the leukocytes as an active vehicle to deliver NPs toward primary and metastatic tumors. Choi et al. proposed that monocytes containing therapeutic NPs could serve as "Trojan Horses" for NP delivery into the tumor regions.[75] They designed gold nanoshell-laden monocytes for photothermal cancer therapy, which can be applied to delivery of various therapies to the hypoxic regions in tumors. Huang et al. reported drug loaded- nanocapsule-functionalized T cells to target the lymphoid tissue sites and enhance the efficacy of chemotherapy (**Figure 1.8**).[76] In this study, T cells served as an active vector to deliver the chemotherapeutic into tumor-bearing lymphoid tissues. Xue et al. developed neutrophil-mediated anticancer drug delivery for suppression of postoperative glioma recurrence (**Figure 1.9a−e**).[77] They showed that neutrophils carrying liposomes that contain paclitaxel, an anticancer drug, can penetrate the brain and suppress the recurrence of glioma. He et al. designed inflammatory monocytes loading protease-sensitive NPs for lung metastasis targeting and drug release (**Figure 1.9f**).[78] They synthesized cytotoxic mertansine-loaded poly(styrene-*co*-maleic anhydride) with a legumain-sensitive peptide and self-assembled into

NPs (SMNs), and then loaded into inflammatory monocytes to prepare the SMNs-loaded monocytes delivery system. This system enabled considerable inhibition on the proliferation, migration, and invasion activities of metastatic breast cancer cells.

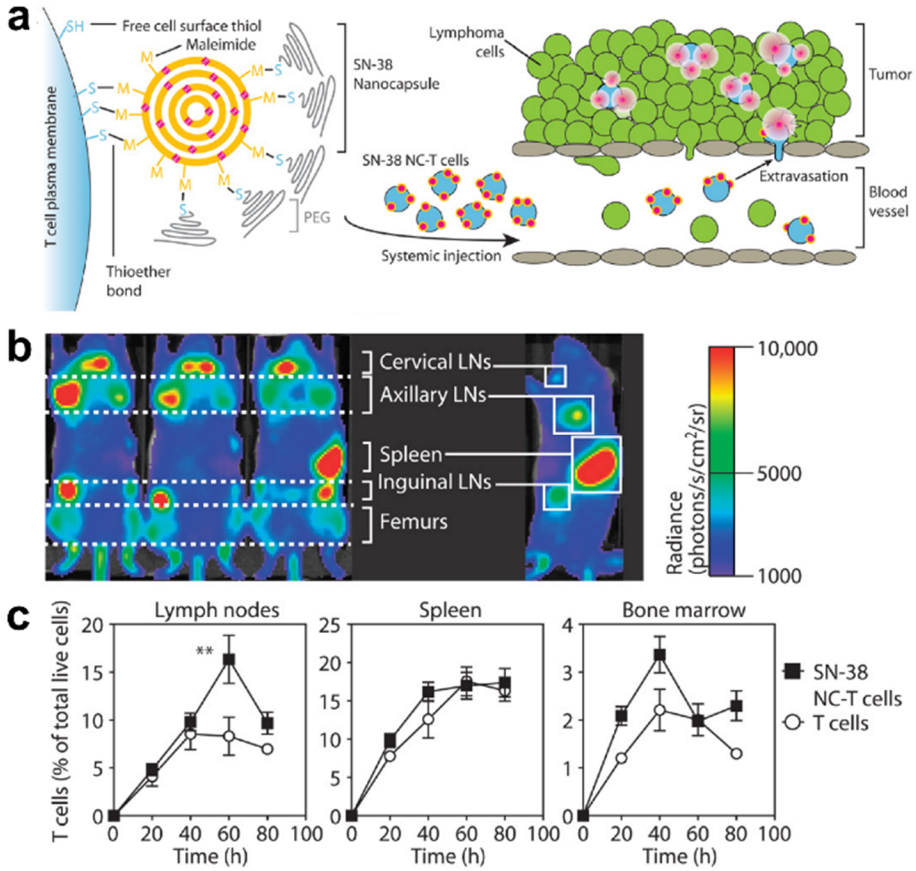

Figure 1.8 (a) Schematic illustration of T cell-mediated delivery of SN-38 NCs into tumors. (b) T cell biodistribution of SN-38 NC-conjugated T cells assessed by bioluminescence 38 h after administration. (c) Kinetics of T cell and SN-38 NC-T cell accumulation in lymph nodes, spleen, and bone marrow assessed by flow cytometry analysis. Reproduced from Ref. [76].

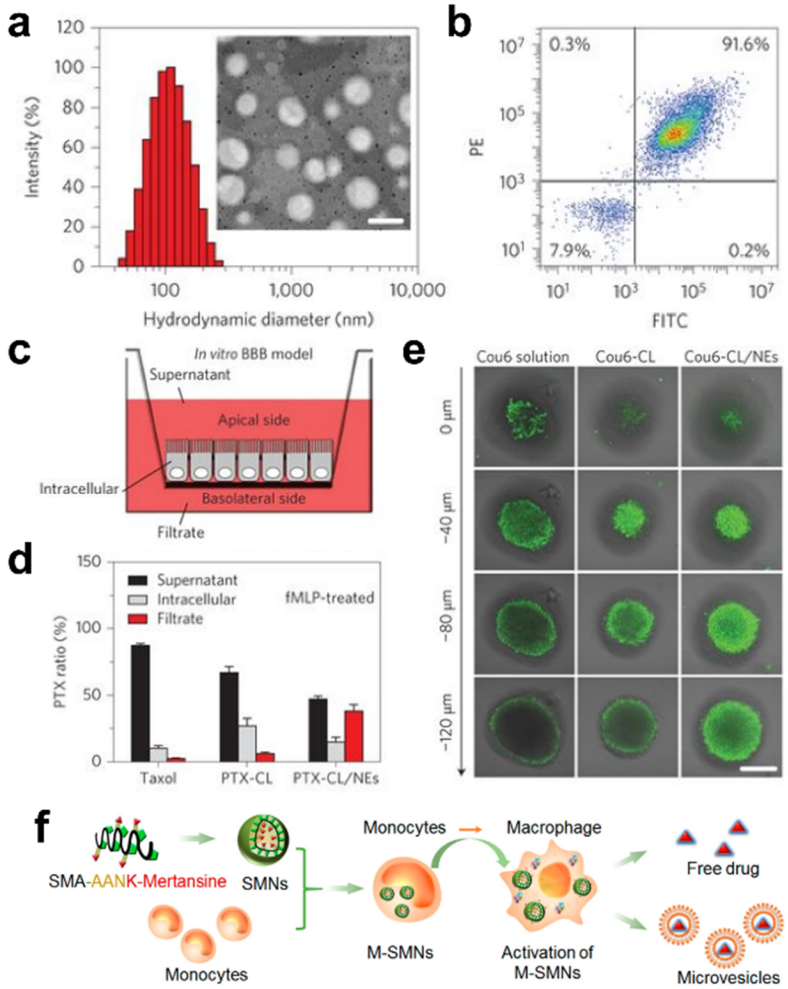

Figure 1.9 (a) Hydrodynamic size and TEM image of paclitaxel-encapsulated cationic liposomes (PTX-CL). (b) Flow cytometry analysis of the purity of neutrophils (NEs). (c) In vitro transwell BBB model to evaluate the penetration capability of PTX-CL/NEs. (d) Quantification of the PTX distribution in the transwell chamber in the presence of NE-chemotactic peptide. (e) Penetration of coumarin 6 (Cou6) into the G422

tumor spheroid. (f) Schematic illustration of the self-assembled into nanoparticles (SMNs)-loaded monocytes delivery system (S-SMNs). (a~e) from Ref. [77] and (f) from Ref. [78].

1.4 Dissertation Overview

As described above, multifunctional inorganic NPs have a great potential in various diseases that occur in hypoxic inflammatory microenvironments. Utilizing the combination of various functional NPs and organic moieties, hypoxia and inflammation can be easily relieved. Since tumor microenvironment is composed of a number of inflammatory cells and hypoxic conditions, multifunctional NPs enable much enhanced cancer therapy by attenuating hypoxic and inflammatory tumor microenvironments. As well as tumor, multifunctional NPs can modulate the subtypes of macrophages and endowing excellent therapeutic effect on various inflammatory diseases. Moreover, targeting the inflammatory cells using novel targeting strategies, multifunctional NPs can be delivered to inflammatory microenvironments that cannot be achieved by a traditional targeting strategy. This dissertation focuses on the designed synthesis of multifunctional inorganic NPs and their applications as a theranostic agent for treatment of hypoxic inflammatory microenvironments.

In Chapter 2, continuously O_2-evolving manganese ferrite-anchored

mesoporous silica NPs (MFMSNs) were developed for tumor hypoxia attenuation. Therapeutic effects of photodynamic therapy (PDT) are highly limited by cancer hypoxia because the PDT process is dependent on O_2 concentration. They can relieve hypoxic conditions and improve therapeutic outcomes of PDT for tumors by employing the continuously O_2-evolving property of MFMSNs through the Fenton reaction. These findings demonstrate great potential of MFMSNs for theranostic agents in cancer therapy.

In Chapter 3, manganese ferrite and ceria NP-anchored mesoporous silica NPs (MFC-MSNs) were synthesized to synergistically scavenge ROS and produce oxygen for M2 polarization of macrophages in rheumatoid arthritis (RA) model. Macrophage polarization from pro-inflammatory M1 phenotype to anti-inflammatory M2 phenotype has been considered as a promising therapeutic strategy to treat inflammatory diseases including RA. M2 polarization of macrophages in joints with RA can be induced by overcoming hypoxia and scavenging ROS. MFC-MSNs exhibit the synergistic effect on O2 generation due to hydroxyl radical scavenging ability of ceria NPs, leading to efficient M1 to M2 macrophage polarization in RA. The inflamed synovial joint of

RA-suffering rat model was successfully oxygenated by intra-articularly administered MFC-MSNs, showing the excellent therapeutic effect on RA.

Finally, in Chapter 4, a click reaction-assisted immune cell targeting (CRAIT) strategy to deliver drug-loaded NPs into deep tumor interiors was proposed. The therapeutic efficiency of drug-loaded NPs is hampered by heterogeneous distribution owing to limited penetration in tumor tissue. Inspired by the fact that cancer cells recruit inflammatory immune cells to support their survival, immune cell-targeting CD11b antibodies and mesoporous silica NPs were modified with *trans*-cyclooctene and tetrazine, respectively, for biorthogonal click chemistry. Since this strategy does not require *ex vivo* manipulation of cells and are applicable to various types of cells and nanovehicles, it shows great potential in enhanced therapeutic efficacy by deep tumor penetration of drug-loaded NPs.

Some contents of this chapter were published in the article, “Recent Development of Nanoparticles for Molecular Imaging.” (*Phil. Trans. R. Soc. A* **2017, *375,* 20170022.)

1.5 References

[1] De, M.; Ghosh, P. S.; Rotello, V. M., *Adv. Mater.* **2008,** *20*, 4225.

[2] Kim, J.; Piao, Y.; Hyeon, T., *Chem. Soc. Rev.* **2009,** *38*, 372.

[3] Kim, D.; Shin, K.; Kwon, S. G.; Hyeon, T., *Adv. Mater.* **2018**, e1802309.

[4] Lu, H.; Ouyang, W.; Huang, C., *Mol. Cancer Res.* **2006,** *4*, 221.

[5] Harris, A. L., *Nat. Rev. Cancer* **2002,** *2*, 38.

[6] Semenza, G. L., *Nat. Rev. Cancer* **2003,** *3*, 721.

[7] Hanahan, D.; Coussens, L. M., *Cancer Cell* **2012,** *21*, 309.

[8] Mosser, D. M.; Edwards, J. P., *Nat. Rev. Immunol.* **2008,** *8*, 958.

[9] Liu, J.; Chen, Q.; Feng, L.; Liu, Z., *Nano Today* **2018,** *21*, 55.

[10] Lee, J. E.; Lee, N.; Kim, T.; Kim, J.; Hyeon, T., *Acc. Chem. Res.* **2011,** *44*, 893.

[11] Ahmad, M. W.; Xu, W.; Kim, S. J.; Baeck, J. S.; Chang, Y.; Bae, J. E.; Chae, K. S.; Park, J. A.; Kim, T. J.; Lee, G. H., *Sci. Rep.* **2015,** *5*, 8549.

[12] Park, Y. I.; Kim, J. H.; Lee, K. T.; Jeon, K.-S.; Na, H. B.; Yu, J. H.; Kim, H. M.; Lee, N.; Choi, S. H.; Baik, S.-I.; Kim, H.; Park, S. P.; Park, B.-J.; Kim, Y. W.; Lee, S. H.; Yoon, S.-Y.; Song, I. C.; Moon, W. K.; Suh, Y. D.; Hyeon, T., *Adv. Mater.* **2009,** *21*, 4467.

[13] Cheng, L.; Liu, J.; Gu, X.; Gong, H.; Shi, X.; Liu, T.; Wang, C.; Wang, X.; Liu, G.; Xing, H.; Bu, W.; Sun, B.; Liu, Z., *Adv. Mater.* **2014,** *26*, 1886.

[14] Xie, J.; Chen, K.; Huang, J.; Lee, S.; Wang, J.; Gao, J.; Li, X.; Chen, X., *Biomaterials* **2010,** *31*, 3016.

[15] Choi, J.-s.; Park, J. C.; Nah, H.; Woo, S.; Oh, J.; Kim, K. M.; Cheon, G. J.; Chang, Y.; Yoo, J.; Cheon, J., *Angew. Chem. Int. Ed.* **2008,** *47*, 6259.

[16] Lee, J.-H.; Jun, Y.-W.; Yeon, S.-I.; Shin, J.-S.; Cheon, J., *Angew. Chem. Int. Ed.* **2006,** *45*, 8160.

[17] Shin, T.-H.; Choi, J.-s.; Yun, S.; Kim, I.-S.; Song, H.-T.; Kim, Y.; Park, K. I.; Cheon, J., *ACS Nano* **2014,** *8*, 3393.

[18] Regino, C. A. S.; Walbridge, S.; Bernardo, M.; Wong, K. J.; Johnson, D.; Lonser, R.; Oldfield, E. H.; Choyke, P. L.; Brechbiel, M. W., *Contrast Media Mol. Imaging* **2008,** *3*, 2.

[19] Lee, N.; Cho, H. R.; Oh, M. H.; Lee, S. H.; Kim, K.; Kim, B. H.; Shin, K.; Ahn, T.-Y.; Choi, J. W.; Kim, Y. W.; Choi, S. H.; Hyeon, T., *J. Am. Chem. Soc.* **2012,** *134*, 10309.

[20] Alric, C.; Taleb, J.; Le Duc, G.; Mandon, C.; Billotey, C.; Le Meur-Herland, A.; Brochard, T.; Vocanson, F.; Janier, M.; Perriat, P.; Roux, S.; Tillement, O., *J. Am. Chem. Soc.* **2008,** *130*, 5908.

[21] Lee, D.-E.; Koo, H.; Sun, I.-C.; Ryu, J. H.; Kim, K.; Kwon, I. C., *Chem.*

Soc. Rev. **2012,** *41*, 2656.

[22] Bae, K. H.; Park, M.; Do, M. J.; Lee, N.; Ryu, J. H.; Kim, G. W.; Kim, C.; Park, T. G.; Hyeon, T., *ACS Nano* **2012,** *6*, 5266.

[23] von Maltzahn, G.; Park, J.-H.; Agrawal, A.; Bandaru, N. K.; Das, S. K.; Sailor, M. J.; Bhatia, S. N., *Cancer Res.* **2009,** *69*, 3892.

[24] Hirsch, L. R.; Stafford, R. J.; Bankson, J. A.; Sershen, S. R.; Rivera, B.; Price, R. E.; Hazle, J. D.; Halas, N. J.; West, J. L., *Proc. Natl. Acad. Sci. U. S. A.* **2003,** *100*, 13549.

[25] Chen, J.; Glaus, C.; Laforest, R.; Zhang, Q.; Yang, M.; Gidding, M.; Welch, M. J.; Xia, Y., *Small* **2010,** *6*, 811.

[26] Gobin, A. M.; Lee, M. H.; Halas, N. J.; James, W. D.; Drezek, R. A.; West, J. L., *Nano Lett.* **2007,** *7*, 1929.

[27] Lee, J.-H.; Jang, J.-t.; Choi, J.-s.; Moon, S. H.; Noh, S.-H.; Kim, J.-W.; Kim, J.-G.; Kim, I.-S.; Park, K. I.; Cheon, J., *Nat. Nanotechnol.* **2011,** *6*, 418.

[28] Kam, N. W. S.; O'Connell, M.; Wisdom, J. A.; Dai, H., *Proc. Natl. Acad. Sci. U. S. A.* **2005,** *102*, 11600.

[29] Yang, K.; Hu, L.; Ma, X.; Ye, S.; Cheng, L.; Shi, X.; Li, C.; Li, Y.; Liu, Z., *Adv. Mater.* **2012,** *24*, 1868.

[30] Zhou, M.; Li, J.; Liang, S.; Sood, A. K.; Liang, D.; Li, C., *ACS Nano* **2015,** *9*, 7085.

[31] Huang, P.; Lin, J.; Wang, X.; Wang, Z.; Zhang, C.; He, M.; Wang, K.; Chen, F.; Li, Z.; Shen, G.; Cui, D.; Chen, X., *Adv. Mater.* **2012,** *24*, 5104.

[32] Rehman, F. U.; Zhao, C.; Jiang, H.; Wang, X., *Biomater. Sci.* **2016,** *4*, 40.

[33] Ge, J.; Lan, M.; Zhou, B.; Liu, W.; Guo, L.; Wang, H.; Jia, Q.; Niu, G.; Huang, X.; Zhou, H.; Meng, X.; Wang, P.; Lee, C.-S.; Zhang, W.; Han, X., *Nat. Commun.* **2014,** *5*, 4596.

[34] Bagalkot, V.; Zhang, L.; Levy-Nissenbaum, E.; Jon, S.; Kantoff, P. W.; Langer, R.; Farokhzad, O. C., *Nano Lett.* **2007,** *7*, 3065.

[35] Lee, J.-H.; Lee, K.; Moon, S. H.; Lee, Y.; Park, T. G.; Cheon, J., *Angew. Chem. Int. Ed.* **2009,** *48*, 4174.

[36] Li, Z.; Barnes, J. C.; Bosoy, A.; Stoddart, J. F.; Zink, J. I., *Chem. Soc. Rev.* **2012,** *41*, 2590.

[37] Kim, J.; Kim, H. S.; Lee, N.; Kim, T.; Kim, H.; Yu, T.; Song, I. C.; Moon, W. K.; Hyeon, T., *Angew. Chem. Int. Ed.* **2008,** *47*, 8438.

[38] Lee, J. E.; Lee, D. J.; Lee, N.; Kim, B. H.; Choi, S. H.; Hyeon, T., *J. Mater. Chem.* **2011,** *21*, 16869.

[39] Kim, J.; Lee, J. E.; Lee, S. H.; Yu, J. H.; Lee, J. H.; Park, T. G.; Hyeon, T., *Adv. Mater.* **2008,** *20*, 478.

[40] Park, Y. I.; Kim, H. M.; Kim, J. H.; Moon, K. C.; Yoo, B.; Lee, K. T.; Lee, N.; Choi, Y.; Park, W.; Ling, D.; Na, K.; Moon, W. K.; Choi, S. H.; Park,

H. S.; Yoon, S.-Y.; Suh, Y. D.; Lee, S. H.; Hyeon, T., *Adv. Mater.* **2012,** *24*, 5755.

[41] Kong, G.; Braun, R. D.; Dewhirst, M. W., *Cancer Res.* **2001,** *61*, 3027.

[42] Whiteside, T. L., *Oncogene* **2008,** *27*, 5904.

[43] Finger, E. C.; Giaccia, A. J., *Cancer Metastasis Rev.* **2010,** *29*, 285.

[44] Muz, B.; de la Puente, P.; Azab, F.; Azab, A. K., *Hypoxia (Auckl)* **2015,** *3*, 83.

[45] Thiery, J. P.; Sleeman, J. P., *Nat. Rev. Mol. Cell Biol.* **2006,** *7*, 131.

[46] Shin, H. J.; Rho, S. B.; Jung, D. C.; Han, I. O.; Oh, E. S.; Kim, J. Y., *J. Cell Sci.* **2011,** *124*, 1077.

[47] Huang, C. C.; Chia, W. T.; Chung, M. F.; Lin, K. J.; Hsiao, C. W.; Jin, C.; Lim, W. H.; Chen, C. C.; Sung, H. W., *J. Am. Chem. Soc.* **2016,** *138*, 5222.

[48] Shannon, A. M.; Bouchier-Hayes, D. J.; Condron, C. M.; Toomey, D., *Cancer Treat. Rev.* **2003,** *29*, 297.

[49] Li, X.; Lee, S.; Yoon, J., *Chem. Soc. Rev.* **2018,** *47*, 1174.

[50] Song, G.; Liang, C.; Gong, H.; Li, M.; Zheng, X.; Cheng, L.; Yang, K.; Jiang, X.; Liu, Z., *Adv. Mater.* **2015,** *27*, 6110.

[51] Jain, R. K., *Science* **2005,** *307*, 58.

[52] Tian, L.; Chen, Q.; Yi, X.; Wang, G.; Chen, J.; Ning, P.; Yang, K.; Liu, Z., *Theranostics* **2017,** *7*, 614.

[53] Wang, S.; Yuan, F.; Chen, K.; Chen, G.; Tu, K.; Wang, H.; Wang, L. Q.,

Biomacromolecules **2015,** *16*, 2693.

[54] Castro, C. I.; Briceno, J. C., *Artif. Organs* **2010,** *34*, 622.

[55] Cheng, Y.; Cheng, H.; Jiang, C.; Qiu, X.; Wang, K.; Huan, W.; Yuan, A.; Wu, J.; Hu, Y., *Nat Commun* **2015,** *6*, 8785.

[56] Ren, H.; Liu, J.; Su, F.; Ge, S.; Yuan, A.; Dai, W.; Wu, J.; Hu, Y., *ACS Appl Mater Interfaces* **2017,** *9*, 3463.

[57] Song, G.; Liang, C.; Yi, X.; Zhao, Q.; Cheng, L.; Yang, K.; Liu, Z., *Adv. Mater.* **2016,** *28*, 2716.

[58] Song, X.; Feng, L.; Liang, C.; Yang, K.; Liu, Z., *Nano Lett.* **2016,** *16*, 6145.

[59] Lopez-Lazaro, M., *Cancer Lett.* **2007,** *252*, 1.

[60] Chen, H.; Tian, J.; He, W.; Guo, Z., *J. Am. Chem. Soc.* **2015,** *137*, 1539.

[61] Song, G.; Chen, Y.; Liang, C.; Yi, X.; Liu, J.; Sun, X.; Shen, S.; Yang, K.; Liu, Z., *Adv. Mater.* **2016,** *28*, 7143.

[62] Prasad, P.; Gordijo, C. R.; Abbasi, A. Z.; Maeda, A.; Ip, A.; Rauth, A. M.; DaCosta, R. S.; Wu, X. Y., *ACS Nano* **2014,** *8*, 3202.

[63] Zhu, W.; Dong, Z.; Fu, T.; Liu, J.; Chen, Q.; Li, Y.; Zhu, R.; Xu, L.; Liu, Z., *Adv. Funct. Mater.* **2016,** *26*, 5490.

[64] Gordon, S., *Nat. Rev. Immunol.* **2003,** *3*, 23.

[65] Liu, Y. C.; Zou, X. B.; Chai, Y. F.; Yao, Y. M., *Int. J. Biol. Sci.* **2014,** *10*,

520.

[66] Parisi, L.; Gini, E.; Baci, D.; Tremolati, M.; Fanuli, M.; Bassani, B.; Farronato, G.; Bruno, A.; Mortara, L., *J Immunol Res* **2018,** *2018*, 8917804.

[67] Harel-Adar, T.; Ben Mordechai, T.; Amsalem, Y.; Feinberg, M. S.; Leor, J.; Cohen, S., *Proc. Natl. Acad. Sci. U. S. A.* **2011,** *108*, 1827.

[68] Kwon, D.; Cha, B. G.; Cho, Y.; Min, J.; Park, E. B.; Kang, S. J.; Kim, J., *Nano Lett.* **2017,** *17*, 2747.

[69] Zeng, F.; Wu, Y.; Li, X.; Ge, X.; Guo, Q.; Lou, X.; Cao, Z.; Hu, B.; Long, N. J.; Mao, Y.; Li, C., *Angew. Chem. Int. Ed.* **2018,** *57*, 5808.

[70] Song, M.; Liu, T.; Shi, C.; Zhang, X.; Chen, X., *ACS Nano* **2016,** *10*, 633.

[71] Parayath, N. N.; Parikh, A.; Amiji, M. M., *Nano Lett.* **2018,** *18*, 3571.

[72] Talmadge, J. E.; Donkor, M.; Scholar, E., *Cancer Metastasis Rev.* **2007,** *26*, 373.

[73] Mantovani, A., *Int. J. Cancer* **1978,** *22*, 741.

[74] Gabrilovich, D. I.; Nagaraj, S., *Nat. Rev. Immunol.* **2009,** *9*, 162.

[75] Choi, M. R.; Stanton-Maxey, K. J.; Stanley, J. K.; Levin, C. S.; Bardhan, R.; Akin, D.; Badve, S.; Sturgis, J.; Robinson, J. P.; Bashir, R.; Halas, N. J.; Clare, S. E., *Nano Lett.* **2007,** *7*, 3759.

[76] Huang, B.; Abraham, W. D.; Zheng, Y.; Bustamante Lopez, S. C.; Luo, S. S.; Irvine, D. J., *Sci. Transl. Med.* **2015,** *7*, 291ra94.

[77] Xue, J.; Zhao, Z.; Zhang, L.; Xue, L.; Shen, S.; Wen, Y.; Wei, Z.; Wang, L.; Kong, L.; Sun, H.; Ping, Q.; Mo, R.; Zhang, C., *Nat Nanotechnol* **2017,** *12*, 692.

[78] He, X.; Cao, H.; Wang, H.; Tan, T.; Yu, H.; Zhang, P.; Yin, Q.; Zhang, Z.; Li, Y., *Nano Lett.* **2017,** *17*, 5546.

Chapter 2. Continuously O_2-Evolving Manganese Ferrite Nanoparticles for Efficient Photodynamic Therapy in Hypoxic Cancer

2.1 Introduction

Photodynamic therapy (PDT), which involves a generation of cytotoxic reactive oxygen species (ROS) by light activation of photosensitizers, has emerged as a promising minimally invasive therapeutic strategy for various types of cancers.[1-7] Since it involves the systemic administration of photosensitizers followed by local activation using light of a specific wavelength, PDT has many advantages over conventional therapies, including minimal invasiveness, repeatability without inducing severe toxicity, and high selectivity and efficacy.[1-3] However, because it inherently employs O_2 to generate ROS, hypoxia

inevitably occurs during PDT.[3-4] Cancer hypoxia plays a critical role in preventing effective cancer treatments such as chemotherapy and radiotherapy, leading to cancer progression by promoting tumor metastasis, initiation of angiogenesis, and receptor upregulation.[8-11] In particular, PDT is highly vulnerable to cancer hypoxia, because O_2 is an essential component in PDT. Consequently, there is a vicious cycle that PDT promotes cancer hypoxia, which in turn inhibits the therapeutic effects of PDT.

Hyperbaric oxygen therapy, which involves breathing pure O_2 in a pressurized chamber, has been applied to overcome hypoxia. Unfortunately, its extensive use is limited by intrinsic side effects including hyperoxic seizures and barotrauma as a result of overproduced ROS in normal tissues.[12] Recently, various nanomaterials, including perfluorocarbon, CaO_2, MnO_2, and carbon nitride, have been used to selectively relieve cancer hypoxia.[13-20] These nanomaterials directly transport O_2 molecules as a delivery vehicle or catalytically generate O_2 under light activation. However, there are several limitations, including poor biocompatibility, difficulties in systemic delivery, transitory O_2 generation effects, and the necessity for continuous external activation. Therefore, the development of biocompatible nanomaterials that can

generate O_2 continuously without invasive treatment and external activation is essential.

Accordingly, we hypothesized that a sufficient amount of O_2 for PDT can be continuously produced via the Fenton reaction in an H_2O_2-rich cancer microenvironment.[21-22] Because H_2O_2 is an abundant tumor metabolite (present at concentrations ranging from 100 μM to 1 mM) compared with the amount in normal tissues as a result of excess ROS produced by hypoxia, it is a singularly appropriate source to produce O_2 within tumors.[23] In this regard, manganese ferrite nanoparticles (MFNs), which can work as a Fenton catalyst, are anchored to mesoporous silica nanoparticles (MFMSNs) that are loaded with the photosensitizer molecule, chlorin e6 (Ce6; **Figure 2.1**). MFNs have been exploited as an efficient catalyst for decomposition of H_2O_2.[24-25] They are not consumed during the reaction, and no external activation is required, which enables continuous O_2 generation with a relatively small amount of the nanoparticles. Moreover, they also exhibit excellent T_2 contrast effect in magnetic resonance imaging (MRI), allowing for *in vivo* tracking of MFMSNs.[26-28] On the other hand, mesoporous silica nanoparticles (MSNs), which exhibit great biocompatibility and high loading capacity, can be readily functionalized with various silane

agents,[29] enabling the conjugation of MFNs and loading of Ce6 for simultaneous hypoxia reoxygenation and enhanced PDT, respectively.

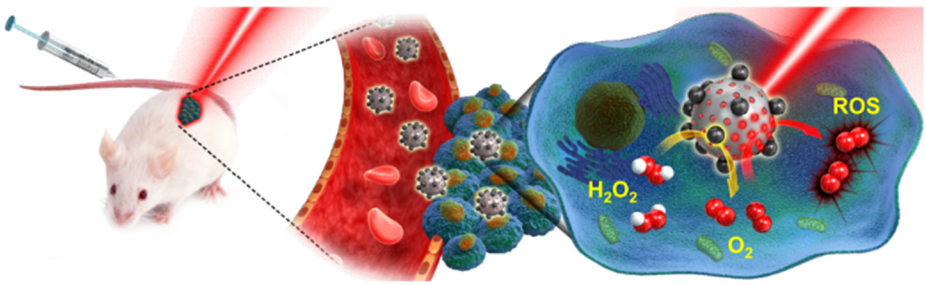

Figure 2.1 Schematic illustration of MFMSNs that act as a catalyst for generating intracellular O_2.

2.2 Experimental Section

2.2.1 Synthesis of MFMSNs

Synthesis of oleic acid-capped manganese ferrite nanoparticle (MFN): MFNs were synthesized via thermal decomposition of iron oleate complex and manganese oleate complex using previously reported method.[30] The iron complex was prepared by dissolving 40 mmol of iron chloride and 120 mmol of sodium oleate into 60 mL of distilled water, 80 mL ethanol and 140 mL n-hexane. Similarly, the manganese complex was prepared by dissolving manganese chloride instead of iron chloride and mixing 80 mmol of sodium oleate. The resulting solution was heated to 70 °C and stirred for 4 h. The upper organic layer was separated and washed several times with distilled water. After washing and evaporation of n-hexane, metal oleate complex was prepared for the synthesis of MFNs. For the synthesis of MFNs, 0.67 mmol of as-prepared precursors, including manganese oleate, 1.33 mmol of iron oleate, and 4 mmol of oleic acid, were dissolved in 10 g of 1-octadecene at room temperature. After degassing, the reaction mixture was heated to 320 °C with a constant heating rate of 3.3 °C min^{-1}, and kept at the

temperature for 1 h. The resulting solution containing oleic acid-capped MFNs were washed with ethanol several times and redispersed in chloroform.

Synthesis of BMPA-capped MFN: 0.5 g of BMPA and 0.05 g of citric acid were dissolved in a mixture of chloroform and DMF (50/50 v/v, 15 mL). 10 mg of oleic acid-capped MFNs were dispersed in this solution and stirred overnight at room temperature. BMPA-capped MFNs were retrieved by several washing with ethanol and finally dispersed in ethanol.

Synthesis of mesoporous silica nanoparticle (MSN): MSNs were synthesized by modifying a previously reported method.[31] The surface of MSNs was functionalized with amine groups by treatment with APTES. 150 μL of APTES was added to MSNs in ethanol, followed by reflux for 3 h. After washing with ethanol several times, amine-functionalized MSNs were redispersed in ethanol (20 mg/mL).

Synthesis of MFMSN: 20 mg of amine-functionalized MSNs were added to as-prepared BMPA-capped MFN dispersion, followed by stirred overnight at room temperature. After washing with ethanol, the nanocrystals were conjugated with PEG using methoxy poly(ethylene

glycol) succinimidyl glutarate (mPEG-SG) and methoxy poly(ethylene glycol) amine (mPEG-AM) in order. After washed with ethanol several times, the resulting MFMSNs were dispersed in 5 mL of distilled water.

2.2.2 Characterization of MFMSNs

TEM was performed on a JEOL EM-2010 microscope operated at 200 kV to observe the morphology of nanoparticles. The crystal structure of MFMSNs was analyzed through X-ray diffraction (Rigaku, D/MAX-2500H). Metal ion concentration was measured by inductively coupled plasma atomic emission spectroscopy (ICP-AES) using an ICPS-7500 spectrometer (Shimadzu). Hydrodynamic sizes and zeta potentials were measured by dynamic light scattering (Malvern). Brunauer-Emmett-Teller (BET) surface area and pore volume were measured by nitrogen adsorption at 77 K using a 3Flex Surface Characterization Analyzer (Micromeritics). Ultraviolet-visible light spectrophotometry (Agilent Technologies) was used to acquire the amount of loaded and released photosensitizer by measuring the absorbance of Ce6 at 400 nm. Photoluminescence spectrophotometry (Agilent Technologies) was used to demonstrate the loading of Ce6 into MFMSNs. Transverse (T_2) relaxation time of protons from the dispersion containing MFMSNs was

measured using a 3 T MRI scanner (Siemens).

To demonstrate the Fenton catalytic effect of MFMSNs, 2.5 mM of H_2O_2 and 5 mM of MFMSNs were mixed in PBS at 37 °C. Then, 50 μL of the solution was added to 100 μL of $Ti(SO_4)_2$ solution (1.33 mL of 24% $Ti(SO_4)_2$ + 8.33 mL of H_2SO_4 in 50 mL of distilled water) every 30 min. The concentration of H_2O_2 was acquired by measuring the absorbance at 405 nm. The continuous catalytic effect was verified by repetitive addition of 2.5 mM of H_2O_2 to the solution, followed by measuring the concentration of H_2O_2 after incubation with MFMSNs. To investigate the capability of evolving oxygen with intracellular concentration of H_2O_2, 125 μM of H_2O_2 was incubated with 250 μM of MFMSNs in PBS, followed by measuring the O_2 concentration with dissolved oxygen meter (HI9136, HANNA instruments, Korea). To measure ROS concentration after PDT, singlet oxygen sensor green (SOSG) assay was used after 0.5 W 670 nm laser irradiation for 5 min in normoxic or hypoxic condition. Hypoxic condition was achieved by adding 125 μM of H_2O_2 into PBS at pH 5.4, followed by Ar blowing into the solution for 30 min.

2.2.3 *In vitro* and *in vivo* study of MFMSNs

Cellular uptake and cell viability test: To examine the cellular uptake of free Ce6 and Ce6-loaded MFMSNs, U-87 MG cells were incubated with 2.5 μM of free Ce6 and Ce6-loaded MFMSNs for 24 h, followed by the analysis using flow cytometry and confocal laser scanning microscope. Cell viability was assessed using MTS cell proliferation assay (G3582, Promega). After U-87 MG cells were incubated with various concentrations of MFMSNs for 24 h, MTS solution was added to media and the absorbance intensity was measured at 490 nm using a microplate reader.

HIF-1α immunostaining: HIF-1α immunostaining was performed in U-87 MG cells incubated in normoxic and hypoxic conditions after the MFMSN treatment. Hypoxic condition was achieved by incubation in hypoxia chamber with 1 % O_2, 5 % CO_2, and 94 % N_2 gas for 4 h. MFMSN-pre-treated U-87 MG cells were incubated in hypoxic condition for 4h, followed by staining with antibodies against HIF-1α (ab190197, Abcam, Cambridge, MA, USA). Rhodamine phalloidin (R415, Molecular Probes) was used to counterstain F-actin in the cells. The stained cells were investigated by confocal laser scanning microscope (CLSM).

Western blot: Preparation of samples for western blot is similar with those for immunostaining. MFMSN-pre-treated U-87 MG cells incubated in normoxic or hypoxic condition were lysed and collected, followed by mixing with sample buffer and heated at 95 °C for 5 min. After electrophoresis with 10 % SDS-PAGE, proteins were transferred to a PVDF membrane. The PVDF membrane was stained with primary antibodies against HIF-1α (ab51608, Abcam, Cambridge, MA, USA) for evaluating the degree of hypoxia and against actin for loading control, then with the HRP-labeled secondary antibody. The HIF-1α level was monitored by enhanced chemiluminescence using Gel Doc system (Bio-Rad).

Measurement of oxygen saturation by photoacoustic imaging: To measure the vascular oxygen saturation (sO_2) inside the U-87 MG solid tumor, Vevo LAZR Photoacoustic Imaging System (VisualSonics Inc., Canada) with LZ550 transducer was used. Before and after intravenous administration of 200 μL of MFMSNs, sO_2 around the tumor was measured by the differential optical absorption of oxygenated and deoxygenated hemoglobin at different wavelength of 850 nm and 750 nm, respectively.

Immunohistochemistry (IHC) of HIF-1α: HIF-1α protein levels before and after MFMSNs treatment were assessed by IHC. 200 μL of 8 mM MFMSNs were injected intravenously into tumor-bearing mice. After 24 h, the mice were sacrificed and tumors were extracted and stained with antibody against HIF-1α. The stained tissues were observed by optical microscope.

CA9 level test: 100 μL or 200 μL of 8 mM MFMSNs were intravenously injected into mouse tail veins. After 24 h, the mice were intravenously administered 100 μL of HypoxiSense 680 (NEV11070, PerkinElmer) to evaluate the degree of hypoxia. After another 24 h, the mice were sacrificed and the tumors were retrieved and imaged using an *in vitro* imaging system (IVIS).

In vitro PDT: For *in vitro* PDT, mice were divided into 7 groups: (1) control, (2) MFMSNs, (3) Ce6-loaded MFMSNs (MFMSN-Ce6), (4) control + laser, (5) Ce6 + laser, (6) MSN-Ce6 + laser, and (7) MFMSN-Ce6 + laser. 200 μL of each samples were intravenously injected into the tumor-bearing mouse models, followed by 0.88 W of 670 nm laser irradiation to the tumor region of mice in laser groups for 5 min after 24 h. The sizes of tumors and body weights were measured twice a week

until 3 weeks after treatment (tumor volume = $W^2 \times L/2$, W=width, L=length). Mice were sacrificed and tumors were retrieved for immunohistochemistry 3 weeks after laser treatment.

Biodistribution and cytotoxicity test of MFMSNs: 200 μL of Cy5-conjugated MFMSNs were intravenously administered to tumor-bearing mice. Then, all the organs were extracted and imaged using the IVIS to observe biodistribution after 24 h. To evaluate cytotoxicity of MFMSNs, 200 μL of MFMSNs were intravenously injected to tumor-bearing mice and organs, including lung, liver, kidney, spleen, heart, and tumor, were histologically identified by H&E staining.

2.3 Result and Discussion

2.3.1 Synthesis and Characterization of MFMSNs

MFMSNs were synthesized according to the previous report with slight modifications.[31] 6 nm-sized MFNs were conjugated to 50 nm-sized MSNs by the nucleophilic substitution reaction. **Figure 2.2a** shows a transmission electron microscope (TEM) image of MFMSNs, demonstrating the uniform size distribution. The presence of manganese and iron ions on the surface of MSNs was confirmed by energy-dispersive X-ray spectroscopy (EDX) analysis (**Figure 2.2b**). The X-ray diffraction (XRD) pattern of MFMSNs reveals the cubic spinel crystal structure of manganese ferrite along with the broad peak of amorphous silica (**Figure 2.3a**). In addition, the MFMSNs were functionalized with polyethylene glycol (PEG) to avoid nonspecific protein binding and facilitate efficient passive targeting by the enhanced permeability and retention (EPR) effect.[32] The successful conjugation of MFNs and PEG onto the surface of MSNs was confirmed by hydrodynamic size (**Figure 2.3b**) and zeta potential measurements (**Figure 2.3c**). The hydrodynamic size increased gradually, and zeta potential was alternatively changed by

conjugating MFNs and PEG. The r_2 relaxivity of MFMSNs was measured to be 60.9 $mM^{-1}s^{-1}$ at 3 T, showing increasingly darker MR contrast as the concentration increases (**Figure 2.4a**). Nitrogen adsorption/desorption experiments yielded a Brunauer-Emmett-Teller (BET) surface area of 429.4 m^2/g and a pore size of 2.8 nm, which enable the high loading of the photosensitizer Ce6 (**Figure 2.4b**). Successful Ce6 loading was validated by UV-Vis (**Figure 2.5a**) and photoluminescence (PL, **Figure 2.5b**) spectra, and the loading capacity and loading efficiency were as high as 1.03 mg/mL and 50.3 %, respectively. Only 5.7 % of Ce6 was released after 7 days (**Figure 2.5c**), demonstrating that most Ce6 molecules can be delivered to the tumors along with MFMSNs.

To evaluate the catalytic effect of MFMSNs, we carried out time-dependent H_2O_2 assays after the addition of MFMSNs. Most of H_2O_2 was decomposed by MFMSNs within 3 h, as shown in **Figure 2.6a**. We then further investigated whether MFMSNs can generate a sufficient amount of oxygen at a low H_2O_2 concentration under hypoxia. As expected, a significant amount of oxygen was produced by MFMSNs in the presence of 100 μM H_2O_2, which is typical intracellular H_2O_2

concentration in tumor cells (**Figure 2.6b**).[23] One of the critical advantages of MFMSNs is continuous catalytic generation of O_2. The catalytic activity of the nanoparticles was nearly unchanged, even after repetitive addition of H_2O_2 (**Figure 2.6c**). Next, the amounts of generated singlet oxygen were compared between the Ce6 and the MFMSNs loaded with the same amount of Ce6 (MFMSN-Ce6) after irradiation with a 680 nm laser for 5 min (**Figure 2.6d**). Under normoxic condition, there was no significant difference between Ce6 and MFMSN-Ce6 after laser irradiation. However, under hypoxic condition, MFMSN-Ce6 produced approximately 2.2 times more singlet oxygen. As hypoxic condition was achieved by purging argon gas into 100 μM H_2O_2 solution at pH 5.4, the greater ROS generation can be attributed to the sufficient amount of oxygen produced by MFMSN-Ce6 via the Fenton reaction.

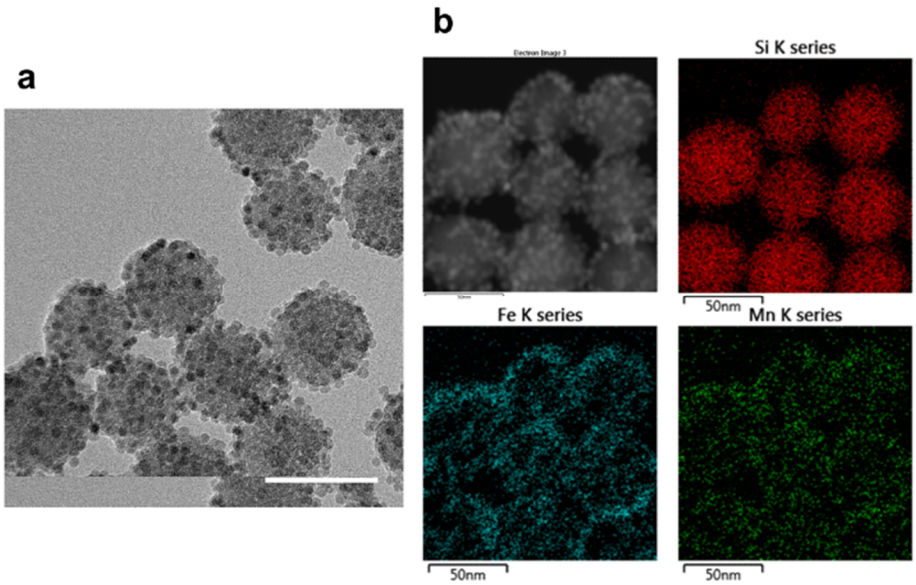

Figure 2.2 (a) TEM image of MFMSNs. Scale bar, 60 nm. (b) EDX analysis of MFMSNs.

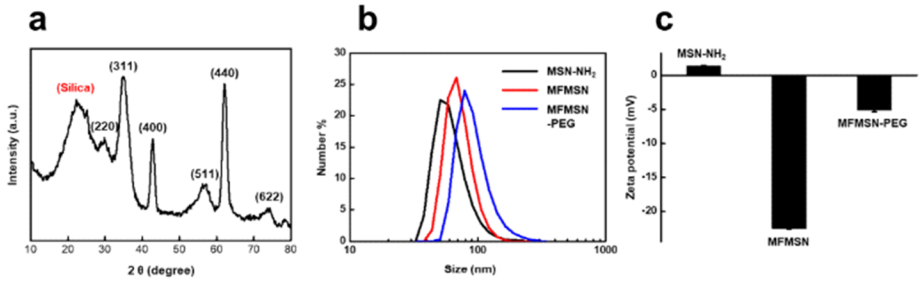

Figure 2.3 (a) XRD pattern of MFMSNs. (b) Size distribution by number and (c) zeta potentials of MFMSNs in each synthetic step.

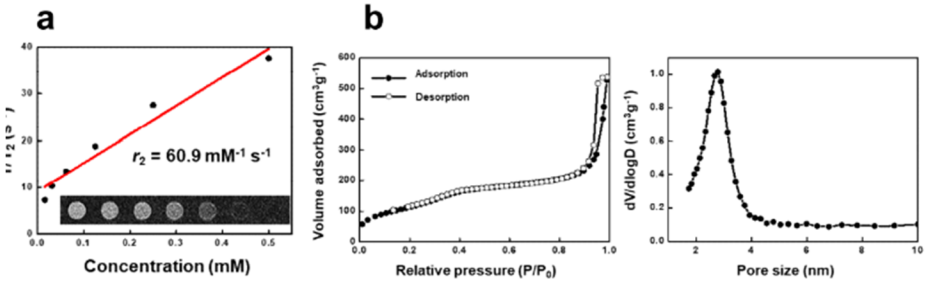

Figure 2.4 (a) Plots of R_2 values of MFMSNs and T_2-weighted MR images of MFMSNs at various concentration of metals at 3 T. (b) N_2 adsorption/desorption isotherms of MFMSNs. (c) Pore size distribution from absorption branch.

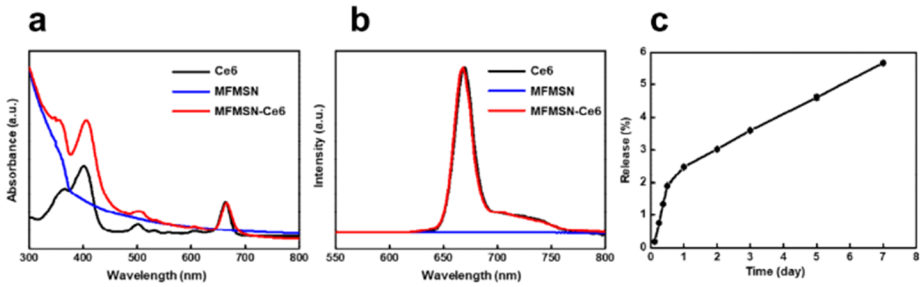

Figure 2.5 (a) UV/Vis absorption spectra and (b) PL spectra of free Ce6, MFMSNs, and Ce6-loaded MFMSNs. (c) Release curve of Ce6 from Ce6-loaded MFMSNs.

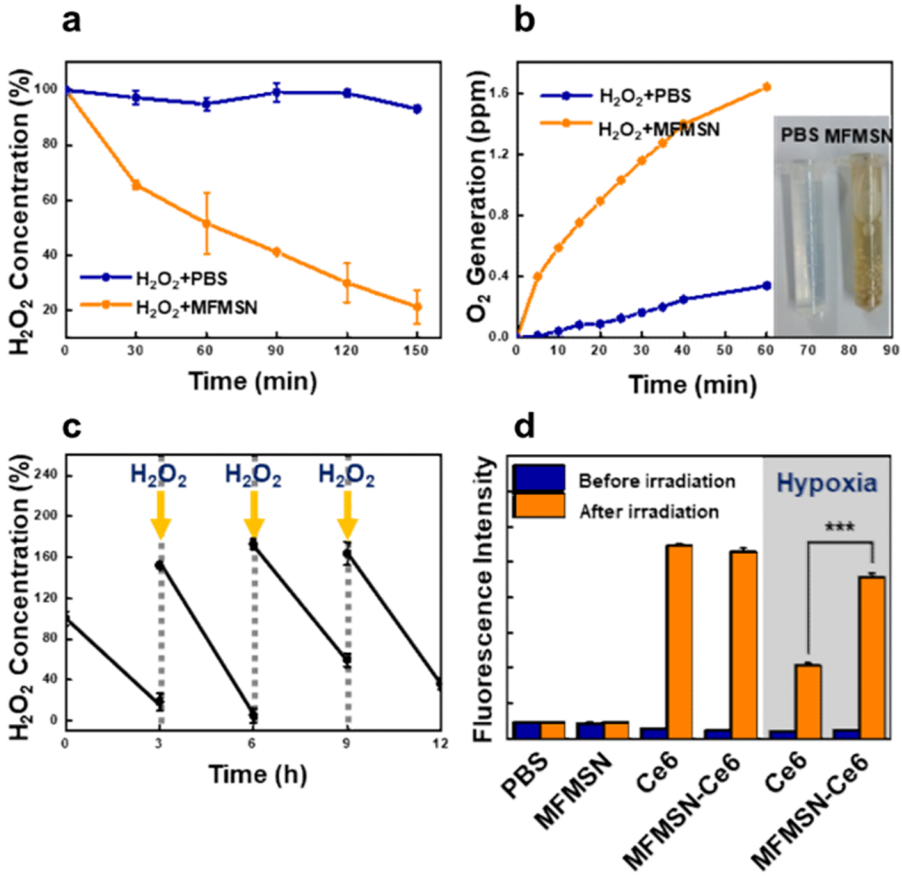

Figure 2.6 (a) Degradation curve of H_2O_2 after treating with PBS or MFMSNs at pH 7.4 (n=3). (b) O_2 generation in H_2O_2 solution after treating with PBS or MFMSNs under physiological condition. (c) Repetitive catalytic ability of MFMSNs with repetitive addition of H_2O_2. (d) The generation of singlet oxygen measured by the fluorescence intensity of SOSG (n=3). ***$P < 0.001$.

2.3.2 *In vitro* study of MFMSNs

To confirm the catalytic effect after endocytosis, we first examined the cellular uptake of MFMSNs by incubating human glioblastoma cancer (U-87 MG) cells with the nanoparticles for 24 h. Confocal laser scanning microscope (CLSM) images show successful Ce6 uptake by U-87 MG cancer cells (**Figure 2.7a**). In addition, flow cytometry analysis show that the fluorescence intensity of the cells treated with MSN-Ce6 or MFMSN-Ce6 is approximately 2 times stronger than that of the cells incubated with free Ce6, suggesting that the MSNs facilitate efficient cellular uptake (**Figures 2.7b**). Moreover, MFMSNs do not show severe toxicity during 24 h at concentrations of up to 200 μM of metal (**Figure 2.7c**). Consequently, all subsequent *in vitro* experiments were performed at a concentration of 200 μM or less.

To further demonstrate the catalytic effect of MFMSNs at the cellular level, the intracellular H_2O_2 concentration was assessed using a fluorescent peroxide assay kit. After treatment with 100 μM H_2O_2, strong green fluorescence indicating high H_2O_2 level was observed in U-87 MG cells. However, the fluorescence intensity of the cells pretreated with MFMSNs for 24 h decreased dramatically, confirming that MFMSNs

decompose intracellular H_2O_2 (**Figure 2.8a, 2.8b**). We then investigated whether MFMSNs can reduce hypoxia. Hypoxic condition was achieved by incubating cancer cells under a hypoxic atmosphere (1% O_2, 5% CO_2, and 94% N_2) for several hours. Because hypoxia-inducible factor (HIF-1α) protein is typically upregulated under hypoxic condition, the degree of hypoxia can be assessed based on HIF-1α levels.[33] To evaluate the HIF-1α levels, HIF-1α and F-actin were co-stained using Alexa Fluor 488-conjugated primary antibody and rhodamine phalloidin, respectively. As presented in **Figure 2.8c**, incubation of cells under low oxygen condition caused the accumulation of HIF-1α. When the cancer cells were treated with MFMSNs, a concentration-dependent reduction in the fluorescence intensity representing HIF-1α was observed (**Figure 2.8d**). Furthermore, western blot analysis shows that the signal intensity of HIF-1α decreased dramatically as the concentration of nanoparticles increased under hypoxic condition (**Figure 2.8e**). These results suggest that MFMSNs can alleviate hypoxia via O_2 generation after cellular uptake.

The ROS-generation capacity of Ce6 was also enhanced by overcoming hypoxia in cancer cells with MFMSNs. Since non-

fluorescent dihydrorhodamine 123 (DHR123) can be rapidly oxidized by ROS into green fluorescent rhodamine 123, DHR123 was used as an intracellular ROS indicator.[34] Under normoxic condition, a similar amount of ROS was generated 30 s after laser irradiation in cells treated with free Ce6 and MFMSN-Ce6. However, in the hypoxic environment, the ROS level of MFMSN-Ce6-treated cells was almost unaltered in comparison with that under normoxic condition, whereas cells treated with free Ce6 showed much lower ROS levels (**Figure 2.9a**). Quantitative analysis using singlet oxygen sensor green (SOSG) assays showed that ROS generation increased by about 2-fold by MFMSNs under hypoxic condition (**Figure 2.9b**). After confirming enhanced ROS production by MFMSN-Ce6 under hypoxic condition, the PDT efficacy of U-87 MG cells incubated with Ce6 or MFMSN-Ce6 under hypoxic and normoxic conditions was investigated using MTS assay. As shown in **Figure 2.10a**, both Ce6 and MFMSN-Ce6 exhibit excellent PDT efficacy under normoxic condition, resulting in noticeable cell death after laser irradiation. Under hypoxic condition, however, only MFMSN-Ce6 maintained good PDT efficacy (**Figure 2.10b**). Moreover, to reconfirm the differences in PDT efficacy, calcein AM and propidium iodide were used to stain live and dead cells, respectively. In contrast

with the Ce6 group, MFMSN-Ce6 displayed similar cytotoxicity toward U-87 MG cells in both normoxic and hypoxic environment, suggesting that MFMSNs successfully alleviate hypoxia and play a pivotal role in maintaining good PDT efficacy even under hypoxic condition (**Figure 2.10c**).

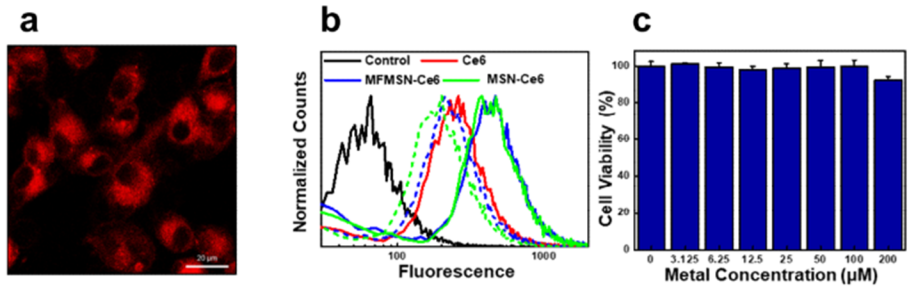

Figure 2.7 (a) CLSM image of U-87 MG cells incubated with MFMSN-Ce6. Scale bar, 20 μm. (b) Flow cytometry data of U-87 MG cells treated with 25 μM of MSN-Ce6, MFMSN-Ce6, or free Ce6 (solid lines). Dashed lines indicate 12.5 μM treatment with MSN-Ce6 or MFMSN-Ce6. (c) *In vitro* U-87 MG cell viability test of MFMSN, determined by MTS assay after incubation with various concentrations of MFMSNs for 24 h (n=3).

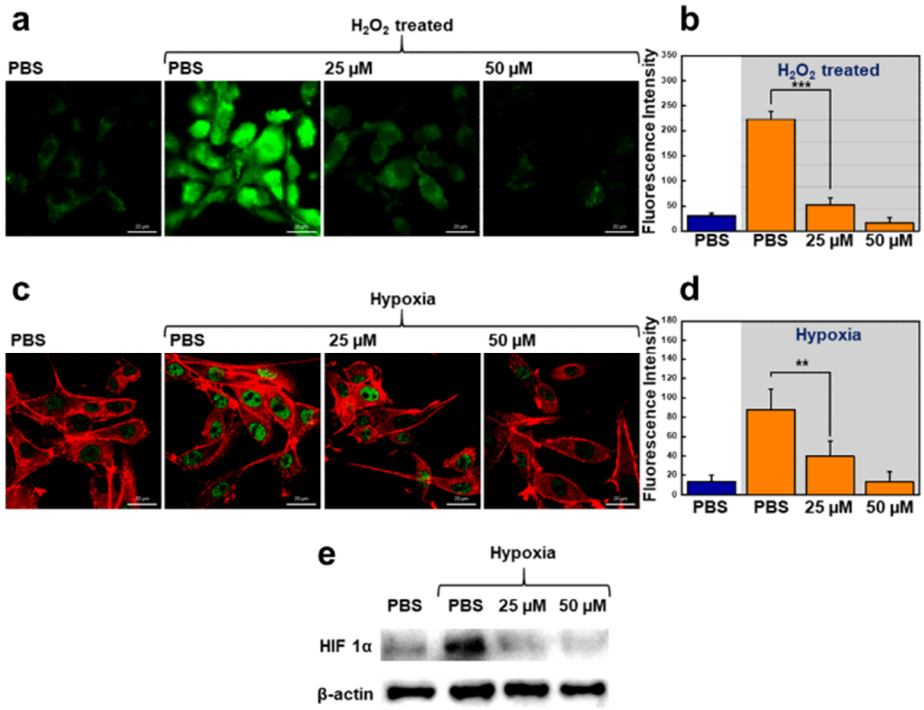

Figure 2.8 (a) CLSM images of green fluorescent intracellular H_2O_2 in cells incubated with PBS or MFMSNs under H_2O_2 treatment, and (b) corresponding fluorescence intensity (n=3). (c) CLSM images of HIF-1α (green) and F-actin (red) in cells incubated with PBS or MFMSN under normoxic or hypoxic condition, and (d) corresponding fluorescence intensity (n=3). (e) Western blots of HIF-1α expression in U-87 MG cells treated with MFMSNs. β-actin was used as a loading control. Scale bar, 20 μm. $^{**}P < 0.01$, $^{***}P < 0.001$.

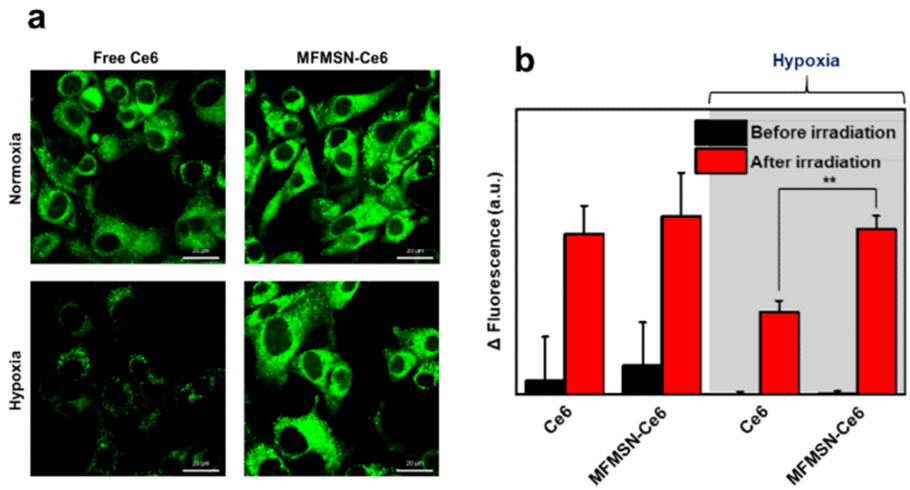

Figure 2.9 (a) Singlet oxygen generation evaluated by DHR123 in U-87 MG cells treated with free Ce6 or MFMSN-Ce6 under normoxic or hypoxic condition. (b) Singlet oxygen generation measured by increased fluorescence intensity of SOSG in cells treated with free Ce6 or MFMSN-Ce6 under normoxic or hypoxic condition (n=3). $^{**}P < 0.01$.

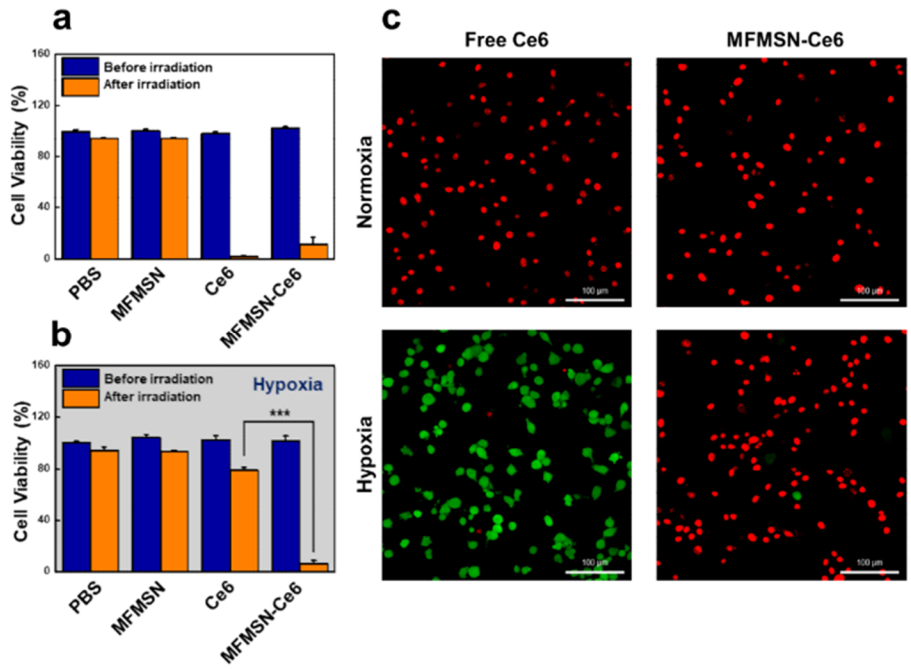

Figure 2.10 Cell viability assay of MFMSN-treated U-87 MG cells in (a) normoxic and (b) hypoxic environments. ***$P < 0.001$. (c) Live/dead cell assay for cells treated with free Ce6 and MFMSN-Ce6 under normoxic and hypoxic conditions. (Green: live cells, red: dead cells)

2.3.3 *In vivo* study of MFMSNs

Based on the *in vitro* results, we next investigated the effectiveness of MFMSNs for treatment of solid tumors *in vivo*. First, a xenograft model was established by injecting U-87 MG tumor cells subcutaneously in BALB/c nude mice. To validate the delivery of the nanoparticles to the tumor, MFMSNs were administered by tail vein injection. MFMSNs successfully accumulated in the tumor via the EPR effect, resulting in signal attenuation in T_2^*-weighted MR images obtained by a 9.4 T MR scanner (**Figure 2.11**). Moreover, Cy5 dye-incorporated MFMSNs were administered by intravenous injection to investigate the biodistribution in tumor tissues and major organs, including the heart, lung, liver, spleen, and kidney (**Figure 2.12**). Although most MFMSNs were located in the liver, a representative organ of the reticuloendothelial system (RES),[35] a significant portion of the fluorescence was observed in tumor tissue. Based on these results, we conclude that intravenously injected MFMSNs were effectively delivered to the tumor tissue through the EPR effect.

To demonstrate the ability of MFMSNs to relieve hypoxia within tumors, we first evaluated oxygen saturation (sO_2) in the blood inside tumors by photoacoustic imaging based on the differential absorption of

oxygenated and deoxygenated hemoglobin at different wavelengths of 850 and 750 nm, respectively.[14] The sO_2 inside tumors increased dramatically after intravenous administration of MFMSNs. In a time-course analysis, we found that sO_2 reached a maximum of 13.5% ± 2.6% 4 h after injection and slowly decreased until 24 h (**Figure 2.13**). Next, HIF-1α levels were assessed using immunohistochemistry to further demonstrate the re-oxygenating ability of MFMSNs. HIF-1α expression was significantly downregulated after the MFMSN treatment (**Figure 2.14a**). Similar to HIF-1α, carbonic anhydrase (CA9) protein is also an endogenous marker of hypoxia representing the degree of hypoxia within tumors.[36] The expression of CA9 was investigated using HypoxiSense, an optical fluorescent dye permitting the quantitative analysis of CA9 levels.[13] After intravenous injection of 100 or 200 μL MFMSNs, the fluorescence intensity of the MFMSN-treated group decreased in a dose-dependent manner compared with that of the untreated control group (**Figure 2.14b, 2.14c**).

After studying the tumor-oxygenating ability of MFMSNs, the *in vivo* therapeutic effects of PDT using Ce6-loaded MFMSNs were evaluated by monitoring the volume of tumors after local laser irradiation (**Figure 2.15a, 2.15b**). Mice were divided into seven groups (three laser-

unirradiated groups and four laser-irradiated groups) to examine various parameters. Compared with the control group, no significant therapeutic effect was observed for the MFMSN- or MFMSN-Ce6-treated groups without laser irradiation. Among the laser-irradiated groups, the tumor volumes of the MSN-Ce6- and MFMSN-Ce6-treated groups decreased dramatically compared with those of the laser-unirradiated groups, whereas no marked reduction of tumor size was observed in other laser-irradiated groups without any treatment or treated with free Ce6 only. Notably, the tumor size of the laser-irradiated MFMSN-Ce6 group was dramatically reduced compared with that of the laser-irradiated MSN-Ce6 group, showing that sufficient oxygen inside tumors generated by MFMSNs resulted in the enhancement of the therapeutic effects. To further investigate the cytotoxic effects of each group, tumor tissues were retrieved and processed for TUNEL analysis after 3 weeks (**Figure 2.15c**). The tendency of the staining was almost identical to previous findings, indicating that the efficacy of PDT was improved in the MFMSN-Ce6-treated laser irradiation group. During the PDT experiments, body weight was also monitored to evaluate whether the nanoparticles negatively affect the health of mice (**Figure 2.16a**). No significant change was observed compared with their initial body weight.

In addition, H&E staining of excised major organs, including the heart, lung, liver, spleen, and kidney, was performed 3 weeks after intravenous administration of MFMSNs (**Figure 2.16b**). Similarly, no major abnormality was observed in the images of stained organ slices. These results demonstrate the negligible toxicity of MFMSN-based PDT treatment.

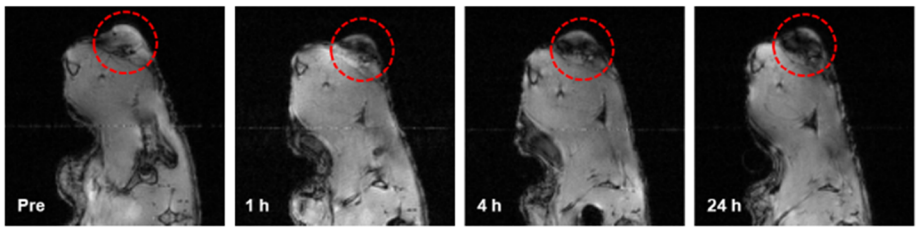

Figure 2.11 *In vivo* T_2^*-weighted MR images of a tumor-bearing mouse at various time periods. Tumors are circled with red dashed lines.

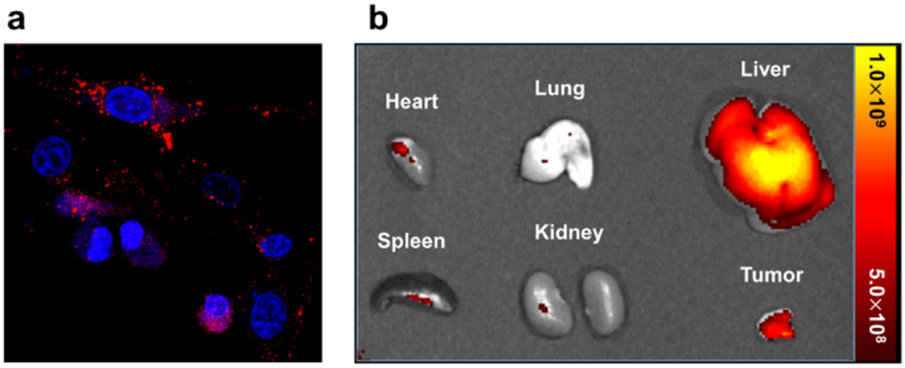

Figure 2.12 (a) CLSM images of U-87 MG cells treated with Cy5-incorporated MFMSNs. Blue, DAPI (nuclei); red, Cy5. (b) IVIS *ex vivo* organ images obtained 24 h after intravenous injection of Cy5-incorporated MFMSNs.

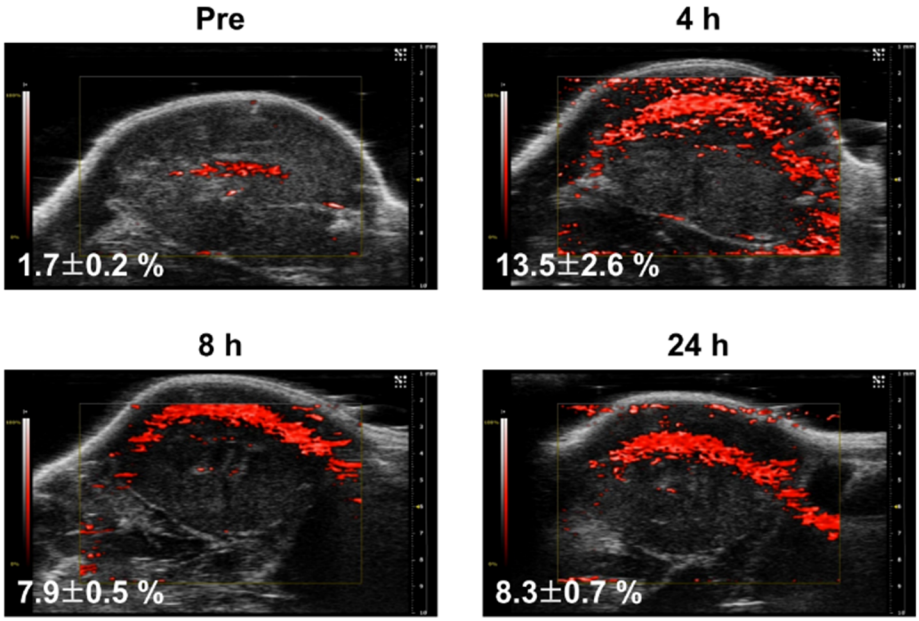

Figure 2.13 Time-dependent photoacoustic images after intravenous administration of MFMSNs into a tumor-bearing mouse.

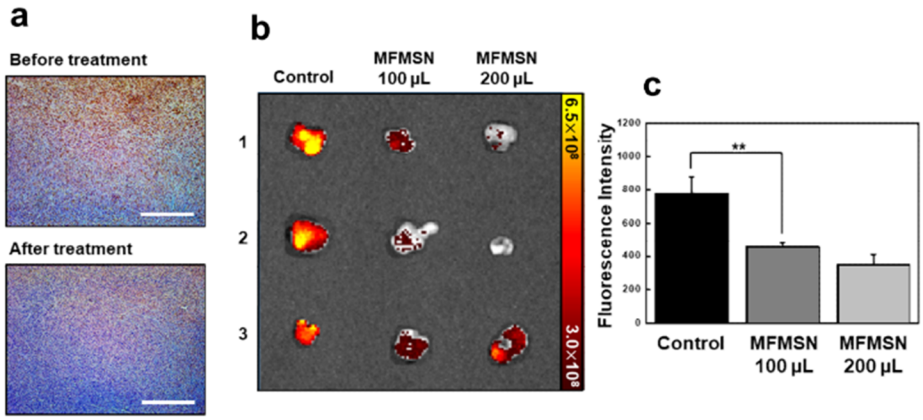

Figure 2.14 (a) Immunohistochemistry (IHC) of HIF-1α in excised tumor tissues. The brown color indicates HIF-1α-positive cell nuclei and the blue color indicates DAPI-stained cell nuclei. Scale bar, 400 μm. (b) Fluorescence images of hypoxic marker CA9 and (c) corresponding fluorescence intensity with or without intravenous administration of MFMSN (n=3). $^{**}P < 0.01$.

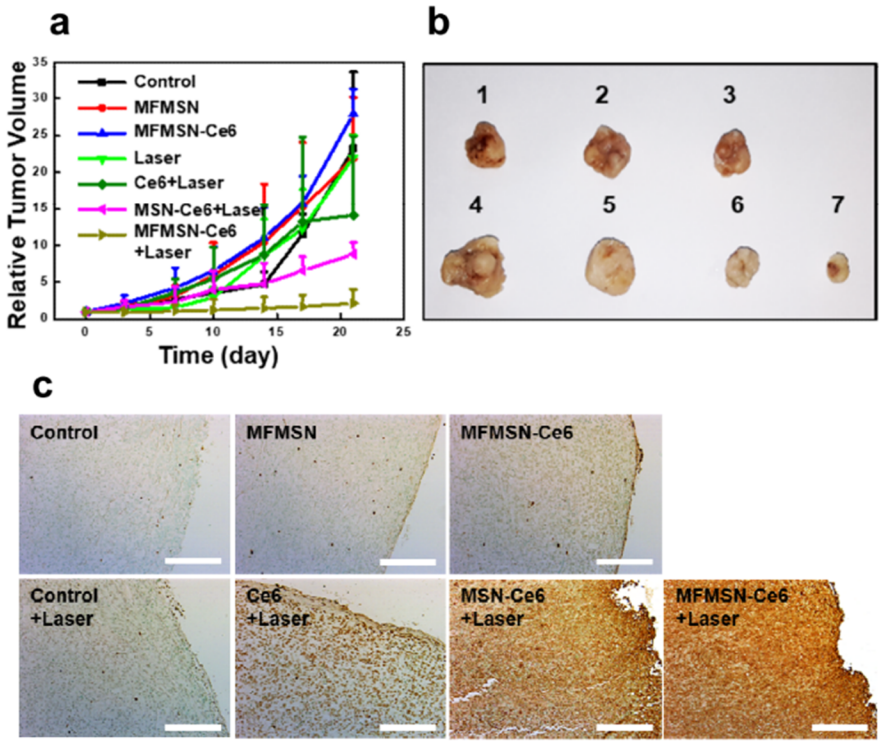

Figure 2.15 (a) Tumor volume changes and (b) corresponding tumor images of various control and experimental groups after 3 weeks (n=3). (c) TUNEL assay of various control groups and experimental groups after PDT. Scale bar, 200 μm.

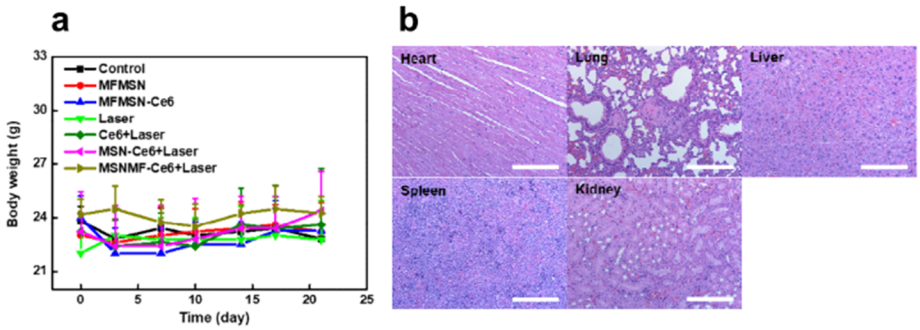

Figure 2.16 (a) Body weight changes of mice after treatment in various groups (n=3). (b) H&E stained tissue images obtained from major organs of a MFMSN-treated mouse for *in vivo* toxicity evaluation. Scale bar, 200 μm.

2.4 Conclusion

In summary, we successfully developed a Ce6-loaded MFMSN system for enhancement of the therapeutic effects of PDT against hypoxic tumors. Our findings demonstrate the continuous generation of oxygen by a Fenton catalyst under physiological condition, improving ROS generation of photosensitizers under hypoxic condition. Markers of hypoxia were significantly reduced after MFMSN treatment in both *in vitro* and *in vivo* models. Minimally-invasive intravenous injection is available with this system due to the excellent bioavailability of MFMSNs. Systemically administered Ce6-loaded MFMSNs were selectively retained at tumor sites owing to the EPR effect and continuously supplied oxygen, enabling simultaneous attenuation of hypoxia and improvement of PDT. These findings demonstrate a great potential of MFMSNs for effective theranostic agents in cancer therapy. **Most of the contents in this chapter were published in the article, "Continuous O_2-Evolving $MnFe_2O_4$ Nanoparticle-Anchored Mesoporous Silica Nanoparticles for Efficient Photodynamic Therapy in Hypoxic Cancer." (*J. Am. Chem. Soc.* **2017**, *139*, 10992.)

2.5 References

[1] Huang, P.; Lin, J.; Wang, X.; Wang, Z.; Zhang, C.; He, M.; Wang, K.; Chen, F.; Li, Z.; Shen, G.; Cui, D.; Chen, X., *Adv. Mater.* **2012,** *24*, 5104.

[2] Liang, G.; Wang, L.; Yang, Z.; Koon, H.; Mak, N.; Chang, C. K.; Xu, B., *Chem. Commun.* **2006**, 5021.

[3] Brown, S. B.; Brown, E. A.; Walker, I., *The Lancet Oncol.* **2004,** *5*, 497.

[4] Liu, Y.; Liu, Y.; Bu, W.; Cheng, C.; Zuo, C.; Xiao, Q.; Sun, Y.; Ni, D.; Zhang, C.; Liu, J.; Shi, J., *Angew. Chem. Int. Ed.* **2015,** *54*, 8105.

[5] Lu, K.; He, C.; Lin, W., *J. Am. Chem. Soc.* **2015,** *137*, 7600.

[6] Lucky, S. S.; Soo, K. C.; Zhang, Y., *Chem. Rev.* **2015,** *115*, 1990.

[7] He, C.; Duan, X.; Guo, N.; Chan, C.; Poon, C.; Weichselbaum, R. R.; Lin, W., *Nat. Commun.* **2016,** *7*, 12499.

[8] Fan, W.; Bu, W.; Zhang, Z.; Shen, B.; Zhang, H.; He, Q.; Ni, D.; Cui, Z.; Zhao, K.; Bu, J.; Du, J.; Liu, J.; Shi, J., *Angew. Chem. Int. Ed.* **2015,** *54*, 14026.

[9] Liu, J.; Liu, Y.; Bu, W.; Bu, J.; Sun, Y.; Du, J.; Shi, J., *J. Am. Chem. Soc.* **2014,** *136*, 9701.

[10] Sun, X.; Niu, G.; Chan, N.; Shen, B.; Chen, X., *Mol. Imaging Biol.* **2011,** *13*, 399.

[11] Xu, R.; Wang, Y.; Duan, X.; Lu, K.; Micheroni, D.; Hu, A.; Lin, W., *J. Am. Chem. Soc.* **2016,** *138*, 2158.

[12] Chen, Q.; Huang, Z.; Chen, H.; Shapiro, H.; Beckers, J.; Hetzel, F. W., *Photochem. and Photobiol.* **2007,** *76*, 197.

[13] Huang, C. C.; Chia, W. T.; Chung, M. F.; Lin, K. J.; Hsiao, C. W.; Jin, C.; Lim, W. H.; Chen, C. C.; Sung, H. W., *J. Am. Chem. Soc.* **2016,** *138*, 5222.

[14] Gordijo, C. R.; Abbasi, A. Z.; Amini, M. A.; Lip, H. Y.; Maeda, A.; Cai, P.; O'Brien, P. J.; DaCosta, R. S.; Rauth, A. M.; Wu, X. Y., *Adv. Funct. Mater.* **2015,** *25*, 1858.

[15] Song, M.; Liu, T.; Shi, C.; Zhang, X.; Chen, X., *ACS Nano* **2016,** *10*, 633.

[16] Cheng, Y.; Cheng, H.; Jiang, C.; Qiu, X.; Wang, K.; Huan, W.; Yuan, A.; Wu, J.; Hu, Y., *Nat. Commun.* **2015,** *6*, 8785.

[17] Chen, H.; Tian, J.; He, W.; Guo, Z., *J. Am. Chem. Soc.* **2015,** *137*, 1539.

[18] Chen, Q.; Feng, L.; Liu, J.; Zhu, W.; Dong, Z.; Wu, Y.; Liu, Z., *Adv. Mater.* **2016,** *28*, 7129.

[19] Fan, W.; Bu, W.; Shen, B.; He, Q.; Cui, Z.; Liu, Y.; Zheng, X.; Zhao, K.; Shi, J., *Adv. Mater.* **2015,** *27*, 4155.

[20] Zheng, D. W.; Li, B.; Li, C. X.; Fan, J. X.; Lei, Q.; Li, C.; Xu, Z.; Zhang, X. Z., *ACS Nano* **2016,** *10*, 8715.

[21] Kremer, M. L., *J. Phys. Chem. A* **2003,** *107*, 1734.

[22] Buda, F.; Ensing, B.; Gribnau, M. C.; Baerends, E. J., *Chem. Eur. J.* **2003,** *9*, 3436.

[23] Halliwell, B.; Clement, M. V.; Long, L. H., *FEBS Letters* **2000,** *486*, 10.

[24] Valdés-Solís, T.; Valle-Vigón, P.; Álvarez, S.; Marbán, G.; Fuertes, A. B., *Catal. Commun.* **2007,** *8*, 2037.

[25] Sahoo, B.; Sahu, S. K.; Nayak, S.; Dhara, D.; Pramanik, P., *Catal. Sci. Technol.* **2012,** *2*, 1367.

[26] Peng, E.; Choo, E. S.; Chandrasekharan, P.; Yang, C. T.; Ding, J.; Chuang, K. H.; Xue, J. M., *Small* **2012,** *8*, 3620.

[27] Shin, T. H.; Choi, Y.; Kim, S.; Cheon, J., *Chem. Soc. Rev.* **2015,** *44*, 4501.

[28] Sahoo, B.; Devi, K. S.; Dutta, S.; Maiti, T. K.; Pramanik, P.; Dhara, D., *J. Colloid. Interface Sci.* **2014,** *431*, 31.

[29] Lee, J. E.; Lee, N.; Kim, T.; Kim, J.; Hyeon, T., *Acc. Chem. Res.* **2011,** *44*, 893.

[30] Park, J.; An, K.; Hwang, Y.; Park, J. G.; Noh, H. J.; Kim, J. Y.; Park, J. H.; Hwang, N. M.; Hyeon, T., *Nat. Mater.* **2004,** *3*, 891.

[31] Lee, J. E.; Lee, N.; Kim, H.; Kim, J.; Choi, S. H.; Kim, J. H.; Kim, T.; Song, I. C.; Park, S. P.; Moon, W. K.; Hyeon, T., *J. Am. Chem. Soc.* **2010,** *132*, 552.

[32] Harbers, G. M.; Emoto, K.; Greef, C.; Metzger, S. W.; Woodward, H. N.;

Mascali, J. J.; Grainger, D. W.; Lochhead, M. J., *Chem. Mater.* **2007,** *19*, 4405.

[33] Li, Q. F.; Wang, X. R.; Yang, Y. W.; Lin, H., *Cell Res.* **2006,** *16*, 548.

[34] Lee, H.; Lee, Y.; Song, C.; Cho, H. R.; Ghaffari, R.; Choi, T. K.; Kim, K. H.; Lee, Y. B.; Ling, D.; Lee, H.; Yu, S. J.; Choi, S. H.; Hyeon, T.; Kim, D. H., *Nat. Commun.* **2015,** *6*, 10059.

[35] Fischer, H. C.; Liu, L.; Pang, K. S.; Chan, W. C. W., *Adv. Funct. Mater.* **2006,** *16*, 1299.

[36] Olive, P. L.; Aquino-Parsons, C.; MacPhail, S. H.; Liao, S. Y.; Raleigh, J. A.; Lerman, M. I.; Stanbridge, E. J., *Cancer Res.* **2001,** *61*, 8924.

Chapter 3. Synergistically O_2-Generating Nanoparticles Inducing M2 Polarization of Macrophages for Rheumatoid Arthritis Treatment

3.1. Introduction

Rheumatoid arthritis (RA) is an inflammatory autoimmune disease that results in long-term synovitis and joint disability.[1-2] Disease modifying anti-rheumatic drugs (DMARDs) are the primary RA treatment, but long-term disease remission is not achieved due to adverse side effects. Biologic DMARDs such as Infliximab, the first Food and Drug Administration-approved TNF-α inhibitor for RA treatment, have shown effectiveness, but with accompanying side effects and high treatment costs.[3-5] Although the pathogenesis of RA has not been clearly elucidated, the mechanism involves u

nwanted immune responses that attack the joints. Inflammatory cel ls including macrophages, dendritic cells, T and B lymphocytes, n eutrophils, and natural killer cells, infiltrate the RA joint synovium and contribute to the severe destruction of joint bone and cartila ge.[3] In particular, macrophages play a crucial role in the pathoph ysiological responses in RA. Macrophages exist in two different p henotypes of a pro-inflammatory classical (M1) phenotype and an anti-inflammatory (M2) phenotype.[6-7] M1 macrophages are predo minant during the early stages of inflammation, inducing inflamm ation by secreting pro-inflammatory cytokines such as IL-1β and TNF-α.[8-9] In contrast, M2 macrophages secrete anti-inflammatory c ytokines and are associated with inflammation resolution.[10] Macrop hages in RA joints are primarily of the M1 phenotype, promoting RA progression by releasing various inflammatory cytokines.[11] T herefore, macrophages have emerged as a potential target for the treatment of inflammatory diseases.[10, 12-16]

Hypoxia-inducible factor (HIF-1α) expression and reactive oxyg en species (ROS) in RA joints induce synovial inflammation and affect the balance of macrophage subtypes. Hypoxia is induced in RA synovium mainly through the increased oxygen d

emand of fibroblast-like synoviocyte hyperplasia and infiltrated inf lammatory cells.[17-18] Hypoxia upregulates HIF-1α in RA, which is r eported to induce polarization of macrophages to the M1 subtype[19-22] through ROS production or another pathway.[23] Thus, inhibition o f HIF-1α can attenuate the M1 phenotype, enhance M2 polarizatio n of macrophages,[24] and effectively ameliorate RA.[3-5] In addition, strategies regulating ROS for M1 to M2 phenotypic tra nsition have been extensively studied for the treatment of inflam matory diseases. For example, abrogation of the NADPH oxidase associated with ROS production inhibits pro-inflammatory M1 macrophage responses.[25] Additionally, ceria nanoparticles (NPs) drive M2 polarization of macrophages by eradicating ROS in a bra in inflammatory disorder model.[26] Taken together, simultaneous in hibition of HIF-1α and ROS could be a promising strategy for shi fting phenotypic transition of pro-inflammatory M1 macrophages to the anti-inflammatory M2 subtype for RA treatment.

Catalytic NPs, such as manganese ferrite NPs, have been rec ently developed as biocompatible therapeutic agents for continuous oxygen generation under H_2O_2-rich hypoxic environments.[27-41] Ma nganese ferrite NPs relieve hypoxic conditions through the Fenton

reaction, downregulating hypoxic markers such as HIF-1α.[27] Mea nwhile, ceria NPs have been investigated as efficient ROS scavengers for various inflammatory diseases.[42-45] The catalytic pr operty of ceria NPs is attributed to the presence of two reversible oxidation states (Ce^{3+} or Ce^{4+}) at the surface of NPs.[46-49] Howev er, a high concentration of the NPs can cause cell cytotoxicity. E xcessive concentrations of manganese ferrite NPs results in cytoto xicity and reduction in oxygen production efficacy, because hydro xyl radicals are generated as intermediates of the Fenton reaction. [50] Ceria NPs also exhibit severe safety concerns associated with their cytotoxicity potential, which can hinder clinical translations.[5 1-52] Therefore, reducing the NP dose by increasing efficiency is e ssential for biomedical applications. We hypothesized that hydroxy l radicals, which is an intermediate of the Fenton reaction, can b e converted to O_2 molecules by ceria NPs, increasing the O_2 gen eration efficiency of the Fenton reaction in a hypoxic environmen t. In other words, we expected that manganese ferrite and ceria NPs exhibit a synergistic effect on O_2 generation through the effic ient scavenging of intermediate ROS, leading to M2 polarization of macrophages with a relatively low NP concentration.

Herein, we designed manganese ferrite and ceria NP-anchored mesoporous silica NPs (MFC-MSNs) for use as a therapeutic ag ent to efficiently generate O_2 and scavenge ROS for M2 polarizat ion of macrophages in RA models (**Figure 3.1**). We further invest igated how manganese ferrite and ceria NPs play a role in the in tracellular pathways of H_2O_2 metabolism and how they synergistic ally affect O_2 generation. In *in vitro* experiments using bone marr ow-derived macrophages (BMDMs), inhibition of HIF-1α expressio n and M2 polarization were observed after treating with MFC-MS Ns. In addition, methotrexate (MTX), which is the most widely u sed small-molecule DMARD, was loaded into the MSNs for susta ined release and efficient RA treatment. We finally demonstrated t hat the MTX-loaded MFC-MSNs exhibit a great therapeutic poten tial in an *in vivo* RA rat model.

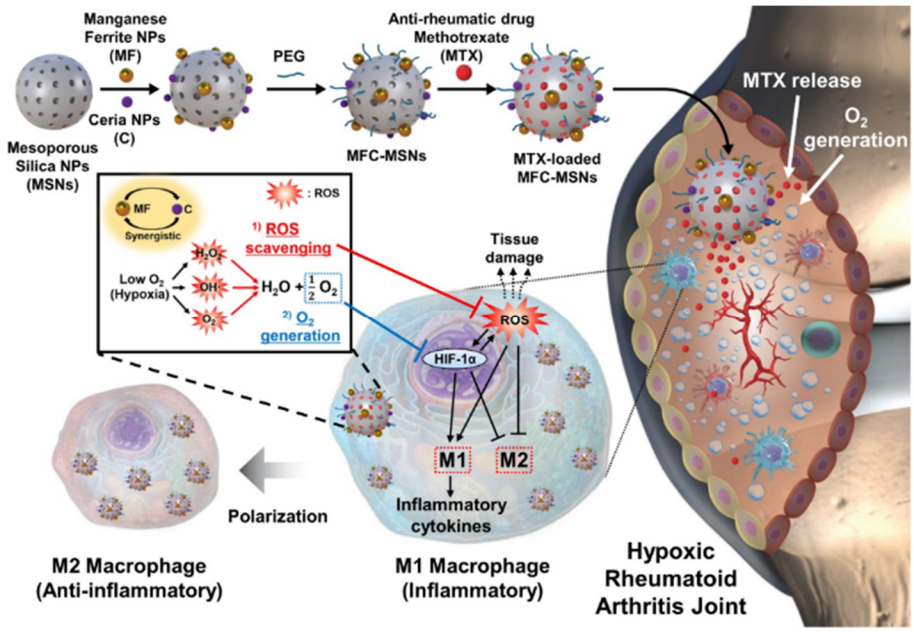

Figure 3.1 Therapeutic mechanism of MFC-MSNs for RA. MFC-MSNs synergistically scavenge ROS and produce O_2, which leads to the polarization of pro-inflammatory M1 macrophages to anti-inflammatory M2 phenotype in hypoxic and inflamed synovial joint. Additionally, methotrexate, an anti-rheumatic drug, can be loaded into MFC-MSNs to augment the therapeutic effect.

3.2 Experimental Section

3.2.1 Synthesis of MFC-MSNs

Synthesis of 6 nm-sized manganese ferrite NPs: Manganese ferrite NPs with a size of 6 nm were synthesized via thermal decomposition of manganese oleate and iron oleate complex according to our previously reported method.[53] Iron oleate complex was prepared by dissolving 40 mmol of iron chloride and 120 mmol of sodium oleate into 60 mL of deionized water, 80 mL of ethanol, and 140 mL of n-haxane. Manganese oleate complex was prepared by substituting manganese chloride instead of iron chloride in the synthetic procedure of iron oleate complex. As-prepared solution was heated to 70 °C and stirred for 4 h. The upper organic layer was separated, and the solvent was evaporated using rotary evaporator to obtain the metal oleate complex. For the synthesis of manganese ferrite NPs, 0.67 mmol of manganese oleate, 1.33 mmol of iron oleate, and 4 mmol of oleic acid were dissolved in 10 g of 1-octadecene. After degassing under vacuum, the mixture was heated to 320 °C with a constant heating rate of 3.3 °C min^{-1} and aged for 1 h. The resulting NPs were washed with ethanol several times and dispersed in chloroform.

Synthesis of 3 nm-sized ceria NPs: 1 mmol of cerium(III) acetate and 12 mmol of oleylamine were dissolved in 15 mL of xylene. The mixture was stirred for 2 h at room temperature and heated to 90 °C. After 1 mL of deionized water was added to the solution, the resulting solution was aged at 90 °C for 3 h and cooled down to room temperature. The ceria NPs were washed with ethanol several times and re-dispersed in chloroform.

Synthesis of BMPA-capped manganese ferrite NPs and ceria NPs: For the synthesis of BMPA-capped manganese ferrite NPs, 0.5 g of BMPA, 0.05 g of citric acid and 15 mg of oleic-acid capped manganese ferrite NPs were dissolved in a mixture of chloroform and DMF (50/50 v/v, 15 mL). Similarly, BMPA-capped ceria NPs were synthesized by mixing 0.25 g of BMPA, 0.025 g of citric acid, 15 mg of ceria NPs in a mixture of chloroform and DMF. The mixtures were stirred overnight, followed by centrifugation to remove the excess ligand. BMPA-capped NPs were dispersed in ethanol for the conjugation to mesoporous silica NPs.

Synthesis of large pore-sized mesoporous silica NPs (MSNs) incorporating RITC and amine functional group: MSNs were synthesized by modifying the previously reported method.[54] 2 g of

CTAC, 0.08 g of triethanolamine was dissolved in 20 mL of deionized water, followed by heating at 95 °C under vigorous stirring. After 1 h, 1.5 mL of mesitylene, 1.5 mL of TEOS, and as-prepared 0.15 mL of APTES-RITC were added to the mixture and aged for another 1 h. The product was collected by centrifugation and washed with ethanol several times. CTAC was removed by ammonium nitrate (60 mg/mL in methanol) treatment for three times. To synthesize amine-functionalized MSNs, 0.15 mL of APTES was added to MSNs, and heated to 70 °C and aged for 3 h. The final product was obtained by washing several times with ethanol.

Synthesis of MFC-MSNs, MF-MSNs, and C-MSNs: 20 mg of amine-functionalized MSNs were added to 15 mg of BMPA-capped manganese ferrite NPs and 15 mg of BMPA-capped ceria NPs, followed by stirred overnight at room temperature. MF-MSNs and C-MSNs were synthesized using 15 mg of manganese ferrite NPs and 60 mg of ceria NPs instead, respectively. Then, the product was washed with ethanol and water several times and subsequently coated with PEG using methoxy poly(ethylene glycol) succinimidyl glutarate (mPEG-SG) and methoxy poly(ethylene glycol) amine (mPEG-AM). The resulting MFC-MSNs, MF-MSNs, and C-MSNs were re-dispersed in 5 mL of deionized

water.

MTX loading and release test: MTX was loaded by mixing 1 mL of MFMSNs and 1 mL of 0.2 mg/mL MTX in deionized water and stirring overnight at room temperature. The excess MTX was removed by washing with deionized water several times. The release profile of MTX was obtained until 7 days by measuring absorbance at 305 nm of the supernatant after centrifugation.

3.2.2 Characterization of MFC-MSNs

TEM analysis was performed using a JEOL EM-2010 microscope operated at 200 kV. Metal ion concentration including manganese, iron, and ceria was analyzed by inductively coupled plasma atomic emission spectroscopy (ICP-AES) using an ICPS-7500 spectrometer (Shimadzu). Hydrodynamic sizes of the NPs were measured using a dynamic light scattering instrument (Malvern). Brunauer-Emmett-Teller (BET) surface area and pore size of MFC-MSNs were measured by nitrogen adsorption at 77 K using a 3Flex Surface Characterization Analyzer (Micrometritics). RITC labeling of MSNs were confirmed using an UV-Vis spectrophotometry (Agilent Technologies). MTX loading was also demonstrated by UV-Vis spectrophotometry by measuring the intrinsic

absorbance of MTX at 305 nm. PL spectrophotometry (Agilent Technologies) was employed to examine the successful labeling of RITC on MSNs.

3.2.3 Catalytic activity of MFC-MSNs

H_2O_2 decomposition: 2.5 mM of H_2O_2 and MF-MSNs, C-MSNs, and MFC-MSNs incorporating 60 μg/mL of manganese ferrite and ceria were mixed in PBS at room temperature. Then, 50 μL of the solution was added to 100 μL of $Ti(SO_4)_2$ solution, including 1.33 mL of 24% $Ti(SO_4)_2$ 8.33 mL of H_2SO_4 in 50 mL of deionized water, every 30 min until 3 h. After the reaction was completed, the absorbance of the solution at 405 nm was measured to evaluate the H_2O_2 concentration.

O_2 generation: 1 M of H_2O_2 and MF-MSNs, C-MSNs, and MFC-MSNs incorporating 150 μg/mL of manganese ferrite and ceria were mixed in 20 mL of PBS at room temperature, followed by measuring the O_2 concentration using a dissolved oxygen meter (HI9136, HANNA instruments, Korea) every 5 min. To observe O_2 bubbles in Eppendorf Tube, 1 M of H_2O_2 and MF-MSNs, C-MSNs, MFC-MSNs incorporating 75 μg/mL of manganese ferrite and ceria were mixed and monitored until 1 h. O_2 generating capability of MFC-MSNs were also evaluated under

hypoxic and inflammatory condition which was achieved by Ar blowing and 100 μM of H_2O_2 addition in PBS.

SOD-mimetic catalytic activity: SOD-mimetic catalytic activity of MF-MSNs, C-MSNs, and MFC-MSNs was investigated using a SOD assay kit (Sigma Aldrich) following the provided protocol. WST working solution, enzyme working solution were added to MF-MSNs, C-MSNs, and MFC-MSNs with a final concentration of 300 μg/mL, followed by thoroughly mixing and incubation at room temperature for 20 min. Then, the absorbance at 450 nm was measured using a microplate reader, and the SOD activity (%) was calculated using the provided equation.

Hydroxyl radical generation: The generation of hydroxyl radical by MF-MSNs, C-MSNs, and MFC-MSNs was assessed using a Hydroxyl Radical Antioxidant Capacity (HORAC) assay (Cell Biolabs, Inc.) with a slightly modified protocol. 40 μL of MF-MSNs, C-MSNs, and MFC-MSNs incorporating 20 μg/mL of manganese ferrite and ceria were mixed with 140 μL of 1X Fluorescein Solution, followed by incubation for 30 min. Then, 20 μL of 1X Hydroxyl Radical Initiator was added to the solution for the Fenton reaction with the NPs. The fluorescence intensity of the solution was measured every 30 min until 2 h using a microplate reader (ex/em = 480/530).

3.2.4 *In vitro* study

Preparation of BMDMs: To obtain rat bone marrow-derived macrophages (BMDMs), bone marrow was collected from the femurs of five-week-old male Sprague Dawley (SD) rat (Koatech., Gyunggi-do, Korea), as described previously.[55] In brief, hind limbs were excised from rat, and muscle tissue was discarded. Tibia and femur bones were then flushed with PBS using 10 mL syringes and 25-gauge needles. Collected bone marrow cells were differentiated into macrophages using conditioned medium of L929 cells. Bone marrow cells were incubated in a 100 mm^2 petri dish for 4 days in 10 mL of macrophage differentiation medium composed of high-glucose DMEM supplemented with 15% (v/v) FBS, 5% (v/v) horse serum, 1% (v/v) penicillin/streptomycin, and 30% (v/v) L929 cell-conditioned medium. L929 cell-conditioned medium was prepared by growing L929 cells in high-glucose DMEM containing 10% (v/v) FBS, and 1% (v/v) penicillin/streptomycin. After 4 days, macrophage differentiation medium was discarded and adherent BMDMs were harvested using cell scrapers.

Cellular uptake and cell viability test: To verify the cellular uptake of RITC-labeled MFC-MSNs, BMDMs were incubated with MFC-

MSNs for 24 h, followed by flow cytometry using FACS AriaII at the National Center for Inter-University Research Facilities (NCIRF) and CLSM analysis. For CLSM analysis, cell nucleus was co-stained using Hoechst 33342 (Thermo Fisher Scientific). Cell viability was evaluated using MTS cell proliferation assay (Promega). After BMDMs were incubated with MF-MSNs, C-MSNs, and MFC-MSNs for 24 h, MTS solution was added to the media and the absorbance was measured at 490 nm suing a microplate reader.

Intracellular H_2O_2 assay: To assess the intracellular H_2O_2 concentration, intracellular H_2O_2 assay (Sigma Aldrich) was used. 100 μM of H_2O_2 was treated to BMDMs which were pre-incubated with 40 μg/mL of MF-MSNs, C-MSNs, and MFC-MSNs for 24 h. After 1 h, the cell media was replaced by assay buffer and intracellular H_2O_2 concentration was measured using a CLSM (ex/em = 490/520).

Intracellular OH radical generation: Intracellular hydroxyl radical generating capability was investigated using 3′-(p-hydroxyphenyl) fluorescein (HPF, Thermo Fisher Scientific) which is an ROS indicator sensitive to hydroxyl radical. BMDMs were incubated with 40 μg/mL of MF-MSNs, C-MSNs, and MFC-MSNs for 24 h, followed by incubation with 100 μM of H_2O_2 for another 1 h. Then, the H_2O_2-containing media

was removed and replaced by 5 μM HPF working solution. The green fluorescence intensity of the well was examined using CLSM analysis after 30 min.

HIF-1α immunostaining: HIF-1α immunostaining was carried out in BMDMs incubated in lipopolysaccharide (LPS)-containing media under hypoxic condition after MF-MSN, C-MSN, and MFC-MSN treatment. Hypoxic condition was achieved by incubation in hypoxia chamber containing 1% O_2, 5% CO_2, and 94% N_2 gas for 4 h. BMDM cells pre-incubated with 40 μg/mL of MF-MSNs, C-MSNs, MFC-MSNs for 4 h were incubated in 0.2 μg/mL of LPS-containing media under hypoxic condition for another 4 h, followed by staining with primary antibody against HIF-1α (Abcam) and Alexa Fluor 488-labeled secondary antibody (Abcam). F-actin was co-stained using rhodamine phalloidin (Thermo Fisher Scientific).

qRT-PCR and western blot analysis: Rat BMDMs were pre-treated with MSNs, C-MSNs, MF-MSNs, and MFC-MSNs for 4 h, followed by extensive PBS washing. Fresh DMEM supplemented with LPS (200 ng/mL) was added and cells were incubated in hypoxic condition (1% O_2, 5% CO_2, and 94% N_2). After 4 h, total RNA and proteins from BMDMs were extracted with TRIzol® (Life Technologies, CA) and Cell

Lysis Buffer® (Cell Signaling Technology, MA), respectively, according to the manufacturer's instructions. The total RNA concentration was determined using a NanoDrop spectrometer (ND-2000, NanoDrop Technologies, Wilmington, DE). Six hundred nanograms of total RNA from each sample were reverse-transcribed into cDNAs. For qRT-PCR, gene expression was assessed using FAST SYBR Green PCR master mix (Applied Biosystems) in StepOnePlus real-time PCR system (Applied Biosystems, CA) with amplification with 40 cycles at 94°C for 3 s and at 60°C for 30 s. For western blot analysis, total protein concentration of cells or NV lysates were determined by Bradford assay. Lysates were mixed with NuPAGE® LDS sample buffer (Life Technologies, CA) and loaded on 10% (w/v) SDS-polyacrylamide gel. After 100 min of electrophoresis at 80V, proteins were transferred to Immobilon-P membrane (Millipore Corp., Bedford, MA) using Trans-Blot® SD Semi-Dry Electrophoretic Transfer Cell (Bio-Rad, CA) for 50 min at 20 V. Subsequently, the membrane was blocked with 5% skim milk for 2 h, and probed with primary antibodies; HIF-1α (Novus Biologicals, CO), iNOS, IL-1β, Cox-2, Arg-1 (Abcam, Cambride, UK) for 16 h at 4°C. Next, captured proteins were conjugated with horseradish peroxidase-conjugated secondary antibodies (Abcam) for 1 h in room temperature.

Blots were developed using chemiluminescence detection system (GE healthcare, Buckinghamshire, UK).

3.2.5 *In vivo* study

Adjuvant-induced arthritis (AIA) model and intra-articular injection of NPs: All animal studies were performed according to an approved protocol by Institutional Animal Care and Use Committee (IACUC) at Seoul National University. For establishment of AIA model, ten-week-old SD rat was purchased from Koatech and allowed to acclimatize for 1 week. Next, arthritis was induced by tail-based intra-dermal injection of 10 mg/mL heat-killed *Mycobacterium butyricum* suspended in incomplete Freund's adjuvant (Chondrex, WA) as described previously.[56-57] The animals were randomly assigned after first signs of inflammation observed at day 8. The AIA-induced animals were randomly assigned into eight groups (n=6). At day 10 of post-adjuvant administration, PBS, MTX, MSN, MSN + MTX, C-MSN, MF-MSN, MFC-MSN, MFC-MSN + MTX were administered *via* intra-articular injection at the knee joint.

Thermographic imaging and assessment of physical functions of

arthritic joint: After intra-articular injection of MTX and various NPs, the temperature variations and photothermal images of hind paws were recorded using an infrared thermal imaging system (FLIR i2, FLIR Systems Inc.) until day 30 of post-adjuvant administration. Changes in paw width were measured by caliper and used as an assessment of inflammation in AIA model. The data has been reported as the cumulative measurement of two hind paws of the animal. Physical functions of AIA animals were assessed by recording average time to cross 70 cm beam. Animals in all the groups were acclimated to the beam set-up at day 3 and 6 before the first sign of inflammation. The average values to cross the beam for rats within each treatment groups were recorded from day 10 onwards.

Photoacoustic imaging of oxygen levels in knee joints: Vascular O_2 saturation (sO_2) around synovial joint was measured by the differential optical absorption of oxygenated and deoxygenated hemoglobin at different wavelength of 850 nm and 750 nm, respectively, using a Vevo LAZR Photoacoustic Imaging System (VisualSonics Inc., Canada) with LZ550 transducer. sO_2 around synovial joint in rat AIA model was measured before and after 50 µL of 300 µg/mL MFC-MSNs were

administered into synovial joints via intra-articular injection.

Immunohistochemical analysis: Tissue histopathology was evaluated to determine the features of RA including hypoxia, M1/M2 balance, angiogenesis, synovial inflammation (synovitis), and cartilage destruction. At day 30, animals were sacrificed, and knee joints were retrieved. The knee joints were fixed for 3 days in 4% neutral buffered formalin in 4°C, and then transferred to decalcifying solution (Sigma, MO) placed above orbital shaker. Tissues were decaled for 14 days in room temperature. Processed samples were embedded in paraffin and sectioned on a microtome at 10μm. For immunohistochemistry, tissue sections were dewaxed, and stained with primary antibodies against HIF-1α, Cox-2, CD206, F4/80 and vWF. Secondary antibodies used were goat anti-mouse Alexa Fluor® 568 for HIF-1α, goat anti-rabbit Alexa Fluor® 488 for F4/80 and CD206, and goat anti-rabbit Alexa Fluor® 568 for Cox-2 and vWF. Sections were counterstained with DAPI, fixed, and examined using confocal fluorescence microscopy (LSM780, Carl Zeiss, Germany). For quantification of vWF-positive vascular density, vWF-positive area relative to DAPI-positive area was measured using ImageJ software.

qRT-PCR analysis of M1/M2 expressions from collected synovial joints: At day 30 post-adjuvant administration, knee joints of all animals were retrieved, and placed in RNAse/DNAse free conical tubes**.** Next, synovial tissues from knee joints were collected using sterile surgical blades. Obtained tissues were minced with surgical blades and homogenized (D1000, Benchmark Scientific, NJ) in the presence of TRIzol®. Next, total RNA was isolated by following manufacturer's instructions. Synthesis of cDNA and qRT-PCR was performed as previously described for *in vitro* analysis.

Safranin-O and H&E staining: For evaluation of cartilage destruction and synovial inflammation, safranin-O and H&E staining was performed, respectively. Safranin-O staining, which stains proteoglycan in cartilage, was carried out by following previously described methods.[58] In brief, dewaxed tissue sections were stained with Weigert's hematoxylin working solution composed of 1% hematoxylin and 30% ferric chloride (anhydrous) for 10 min. After extensive washing, sections were counter-stained with fast green (FCF) solution for 5 min. Rinsed with 1% acetic acid, slides were stained with 0.1% safranin O solution for 5 min. For H&E staining, dewaxed tissue

sections were initially stained with hematoxylin working solution for 10 min. After extensive washing with running tap water and 95% alcohol, slides were stained with 1% Eosin Y solution for 3 min. After dehydration, safranin-O and H&E stained tissue sections were mounted with Canada Balsam (Sigma). Knee joints and synovial tissues were visualized by optical microscopy for assessment of cartilage destruction and synovial inflammation, respectively. Cartilage destruction was scored using Mankin's method as previously described,[59] with seven investigators who were blinded to the experimental animal groups.

3.3 Result and Discussion

3.3.1 Synthesis and Characterization of MFC-MSNs

MFC-MSNs were synthesized according to our recently reported method with slight modifications.[27, 42] Large pore-sized MSNs were decorated with 3 nm-sized ceria NPs and 6 nm-sized manganese ferrite NPs by a nucleophilic substitution reaction. Inductively coupled plasma atomic emission spectrometer (ICP-AES) analysis revealed that the weight ratio of manganese and iron ions to cerium ions was approximately 1.0. The conjugation of manganese ferrite and ceria NPs to MSNs was confirmed by a transmission electron microscopy (TEM) of MFC-MSNs (**Figure 3.2a**). Through energy-dispersive X-ray spectroscopy (EDX) analysis, manganese, iron, and cerium ions were observed on the surface of MSNs (**Figure 3.2b**). Nitrogen adsorption-desorption experiments showed that MFC-MSNs have a Brunauer-Emmett-Teller (BET) surface area of 320.19 m^2/g and a median pore size of 3.80 nm (**Figure 3.3**). We added the swelling agent, mesitylene, to the reaction mixture to synthesize large pore-sized MSNs for efficient drug uptake. Rhodamine B isothiocyanate (RITC) was incorporated into the

MSNs for fluorescence labeling, which was validated by ultraviolet-visible (UV-Vis) and photoluminescence (PL) spectroscopy (**Figure 3.4**). For biomedical applications, the surface of the NPs was coated with polyethylene glycol (PEG) to avoid nonspecific protein adsorption under *in vivo* conditions. The hydrodynamic size was increased from 67.3 ± 1.3 nm of MSNs to 80.8 ± 2.2 nm of PEGylated MFC-MSNs after the conjugation with manganese ferrite and ceria NPs (**Figure 3.5**).

Next, we compared the catalytic properties of MFC-MSNs with those of manganese ferrite NP-anchored MSNs (MF-MSNs) and ceria NP-anchored MSNs (C-MSNs) to investigate the synergistic effect of manganese ferrite and ceria NPs. In a time-dependent H_2O_2 assay under physiological condition (pH 7.4), 31.6% and 20.5% of H_2O_2 was decomposed after 3 h by MF-MSNs and C-MSNs, respectively (**Figure 3.6a**). Interestingly, however, the majority of H_2O_2 was decomposed by the same concentration of MFC-MSNs after only 1.5 h, demonstrating the dramatically enhanced catalytic effect of MFC-MSNs. The O_2 generation capability of MFC-MSNs was also dramatically enhanced compared with that of MF-MSNs and C-MSNs, as demonstrated by increased dissolved oxygen value and the number of O_2 bubbles (**Figure 3.6b, 3.6c**). These results indicate that manganese ferrite and ceria NPs

exhibit synergistic effects on H_2O_2 decomposition and O_2 generation. To understand this synergistic effect, we further investigated the concentration changes in hydroxyl radicals and superoxide anions, which are intermediates in the intracellular H_2O_2 metabolism pathway. First, the superoxide anion-decomposing ability of the NPs was evaluated using a superoxide dismutase (SOD) assay. The SOD activity of MF-MSNs, C-MSNs, and MFC-MSNs was 64.9 ± 1.0%, 19.4 ± 13.4%, and 79.2 ± 2.2%, respectively. All NPs possessed SOD activity, but no synergistic effect on SOD activity was observed for the manganese ferrite and ceria NPs (**Figure 3.7a**). Next, hydroxyl radical generation in the presence of NPs was evaluated after adding H_2O_2. We observed that MF-MSNs generated hydroxyl radicals as an intermediate of the Fenton reaction (**Figure 3.7b**). Notably, MFC-MSNs did not produce hydroxyl radicals, indicating that ceria NPs scavenged these radicals produced by manganese ferrite NPs. Therefore, we concluded that the synergistic effect on efficient H_2O_2 decomposition and O_2 generation is attributed to the conversion of hydroxyl radicals to O_2 molecules by ceria NPs during the Fenton reaction of manganese ferrite NPs (**Figure 3.7c**). Moreover, we confirmed that the synergistic O_2 generation by MFC-MSNs also occurs under low H_2O_2 concentration such as 100μM, which is the

intracellular concentration of H_2O_2 under inflammatory conditions (**Figure 3.8**).[60-61]

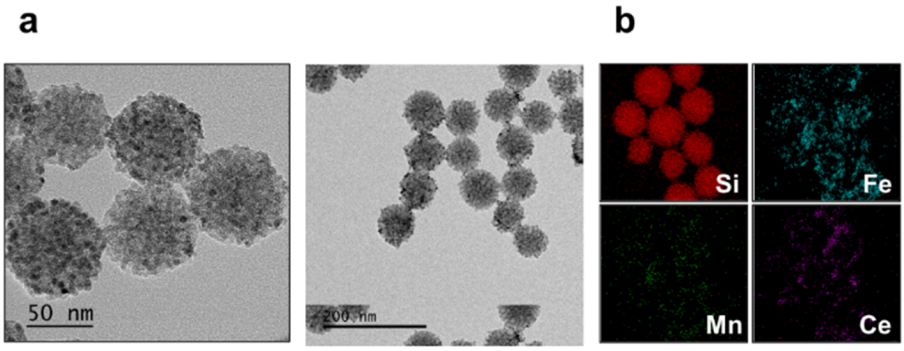

Figure 3.2 (a) TEM image of MFC-MSNs. (b) EDX mapping images of MFC-MSNs, showing the successful conjugation of manganese ferrite and ceria NPs on MSNs. Scale bar, 100 nm.

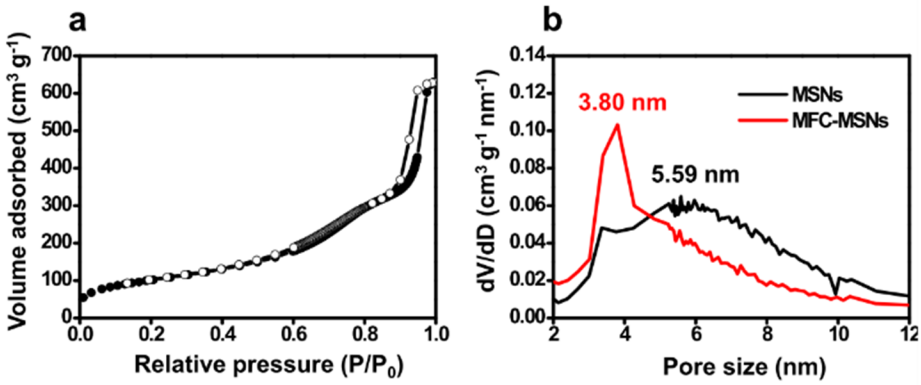

Figure 3.3 (a) N_2 adsorption/desorption isotherms of large pore MSNs. (b) Pore size distribution of large pore MSNs and MFC-MSNs.

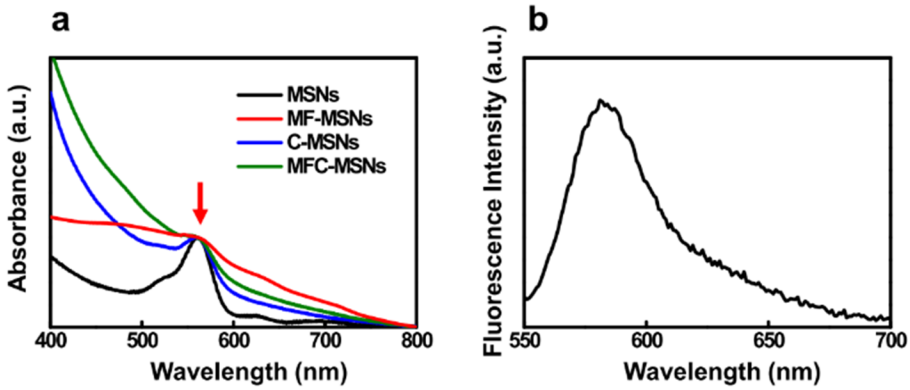

Figure 3.4 (a) UV/Vis absorption spectra of RITC-labeled NPs and (b) PL spectrum of RITC-labeled MFC-MSNs. Red arrow indicates the specific absorption of RITC at 570 nm.

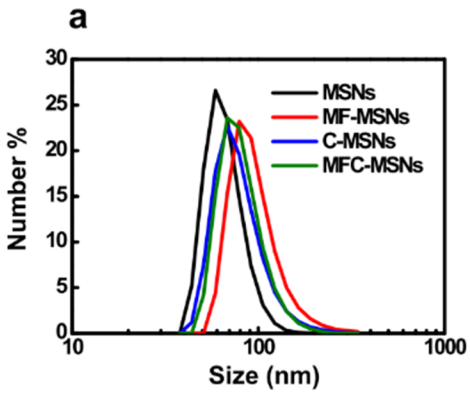

b

	HD (nm)
MSNs	67.27 ± 1.27
MF-MSNs	100.42 ± 2.57
C-MSNs	70.12 ± 6.37
MFC-MSNs	80. 75 ± 2.23

Figure 3.5 (a) Size distribution by number of various NPs and (b) the corresponding hydrodynamic sizes.

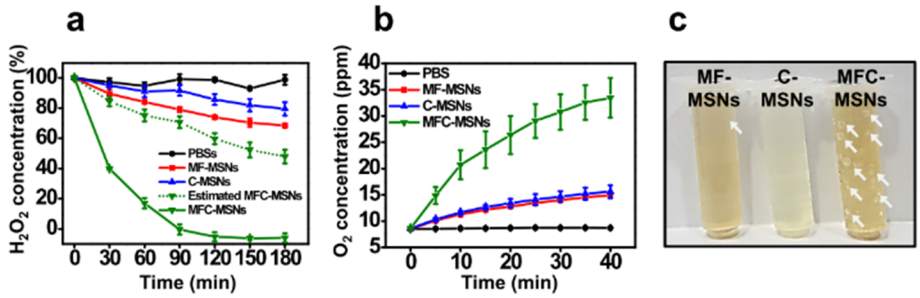

Figure 3.6 (a) H_2O_2 degradation curves in the presence of MF-MSNs, C-MSNs, and MFC-MSNs at pH 7.4 (n=3). Estimated H_2O_2 degradation of MFC-MSNs was obtained by simply adding the degraded H_2O_2 concentration of MF-MSNs and C-MSNs. (b) O_2 generation curves in 1 M of H_2O_2 solution in the presence of the NPs under physiological conditions (n=3). (c) MFC-MSNs generate much more O_2 bubbles compared with MF-MSNs and C-MSNs after 1 h incubation with 1 M of H_2O_2. White arrows indicate generated O_2 bubbles.

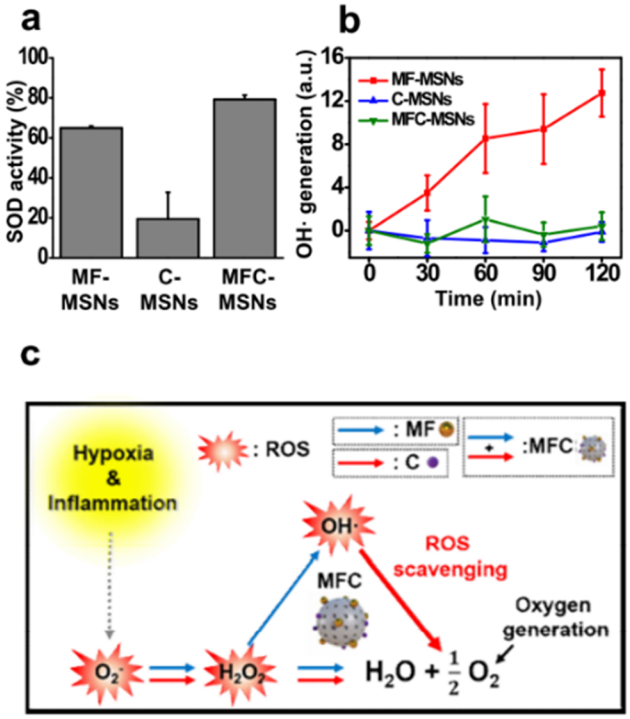

Figure 3.7 (a) SOD activity of MF-MSNs, C-MSNs, and MFC-MSNs (n=3). (b) Time-dependent hydroxyl radical generation of MF-MSNs, C-MSNs, and MFC-MSNs in the presence of H_2O_2 (n=3). (c) Proposed mechanism of the synergistic O_2 generation and ROS scavenge of MFC-MSNs. Compared to either ceria (C) or manganese ferrite (MF) alone, MFC can generate additional O_2 by scavenging intermediate hydroxyl radical generated by manganese ferrite NPs during the Fenton reaction. In addition, MFC can eliminate more H_2O_2 ROS than either C or MF alone.

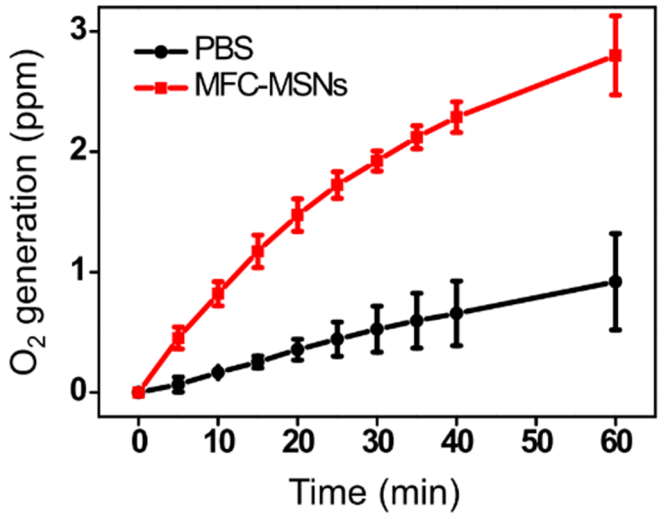

Figure 3.8 O_2 generation of MFC-MSNs at the presence of as low as 100 μM of H_2O_2, which is intracellular concentration of H_2O_2 under inflammatory condition (n=3).

3.3.2 *In vitro* study of MFC-MSNs

We further performed *in vitro* experiments using BMDMs isolated from rats. After 24 h incubation with RITC-labeled MFC-MSNs, confocal laser scanning microscopy (CLSM) showed efficient cellular uptake of MFC-MSNs by BMDMs (**Figure 3.9a**). Flow cytometry analysis also showed that the fluorescence intensity of cells increased after incubation with MFC-MSNs in a concentration-dependent manner (**Figure 3.9b**). In addition, MFC-MSNs did not exhibit cytotoxicity for 24 h at concentrations up to 55 μg/mL, as determined by MTS assay (**Figure 3.9c**). Thus, we carried out subsequent *in vitro* experiments at a MFC-MSN concentration below 55 μg/mL.

To evaluate the ROS scavenging effect of MFC-MSNs under *in vitro* conditions, we first assessed intracellular H_2O_2 levels using an intracellular H_2O_2 assay kit (**Figure 3.10a**). After MF-MSN, C-MSN, and MFC-MSN-pretreated BMDMs were incubated with 100 μM H_2O_2 for 1 h, we determined intracellular H_2O_2 levels through fluorescence intensity. MFC-MSNs decomposed intracellular H_2O_2 more efficiently than the control groups, which is consistent with previous results, demonstrating the synergistic H_2O_2-degrading capability of MFC-MSNs (Figure 2a). We then evaluated the intracellular concentrations of

hydroxyl radicals using 3′-(p-hydroxyphenyl) fluorescein (HPF), which is a ROS indicator sensitive to hydroxyl radicals (**Figure 3.10b**). After MF-MSN, C-MSN, and MFC-MSN-pretreated BMDMs were treated with 100 μM H_2O_2, the fluorescence intensity of HPF was evaluated. BMDMs pretreated with C-MSNs or MFC-MSNs showed significantly decreased fluorescence intensities compared with that of the H_2O_2-treated control group, confirming that ceria NPs can efficiently eradicate intracellular hydroxyl radicals.

To verify the hypoxia-attenuating ability of MFC-MSNs, we evaluated HIF-1α expression levels. After pretreatment with MF-MSNs, C-MSNs, and MFC-MSNs, BMDMs were incubated under hypoxic and inflammatory conditions for 4 h, which was achieved by a hypoxic atmosphere (1% O_2, 5% CO_2, and 94% N_2) and the addition of 0.2 μg/mL lipopolysaccharide (LPS). Hypoxia and LPS upregulated HIF-1α expression, which was attenuated by treatment with MF-MSNs, C-MSNs, and MFC-MSNs (**Figure 3.11a**). The reduction in HIF-1α expression levels was most prominent with MFC-MSNs, implicating the synergistic generation of O_2 by MFC-MSNs.

We next evaluated *in vitro* M1 to M2 phenotypic transition of BMDMs after incubation with MFC-MSNs. Western blot analysis

showed that protein expression of HIF-1α and the pro-inflammatory M1 markers, including iNOS, IL-1β, and Cox-2, were significantly increased after hypoxia and LPS treatment (**Figure 3.11b**). Expression levels of HIF-1α and M1 markers exhibited a similar tendency, suggesting that HIF-1α plays a crucial role in the inflammatory behavior of activated macrophages.[42-45] Notably, treatment with MFC-MSNs markedly reduced expression levels of HIF-1α and pro-inflammatory M1 markers. Expression levels of arginase-1 (Arg-1), a representative M2 marker, was significantly increased in BMDMs treated with MFC-MSNs compared with that of the other groups. qRT-PCR analysis of BMDMs revealed that hypoxia and LPS treatment increased mRNA expression levels of the M1 markers including iNOS, IL-6, and TNF-α (**Figure 3.11c**). Similarly, MFC-MSN treatment reduced mRNA expression levels of the M1 markers significantly. In contrast, the anti-inflammatory M2 markers including Arg-1, CD206, and IL-10 were markedly increased after MFC-MSN treatment. Manganese ferrite and ceria NPs also showed a macrophage polarization effect but to a lesser extent than that of MFC-MSNs. Taken together, we verified the successful M1 to M2 phenotypic transition of macrophages by MFC-MSNs that synergistically scavenge ROS and produce O_2.

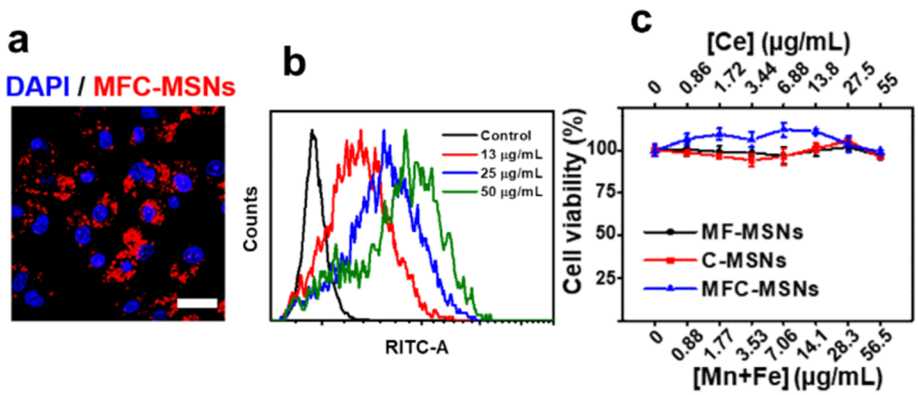

Figure 3.9 (a) CLSM images showing the cellular internalization of RITC-labeled MFC-MSNs to rat BMDMs. Scale bar, 20 μm. (b) Flow cytometry data of rat BMDMs treated with various concentration of RITC-labeled MFC-MSNs. (c) BMDM viability as determined by MTS assay after incubation with C-MSNs, MF-MSNs, and MFC-MSNs at various concentrations for 24 h (n=3).

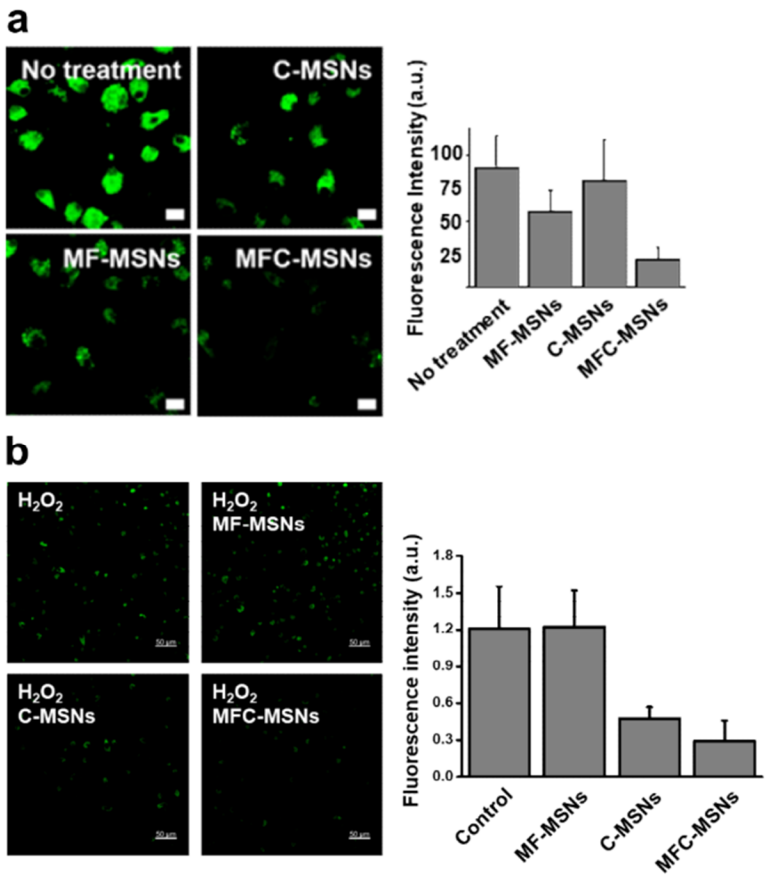

Figure 3.10 (a) CLSM images of intracellular H_2O_2 (green) in BMDMs incubated with MF-MSNs, C-MSNs, and MFC-MSNs in the presence of H_2O_2 in the medium, and the corresponding fluorescence intensity (n=5). Scale bars, 20 μm. (b) Intracellular hydroxyl radical concentration of BMDMs pretreated with MF-MSNs, C-MSNs, and MFC-MSNs after 100 μM of H_2O_2 treatment using HPF, which is an ROS indicator especially sensitive to hydroxyl radical (n=5).

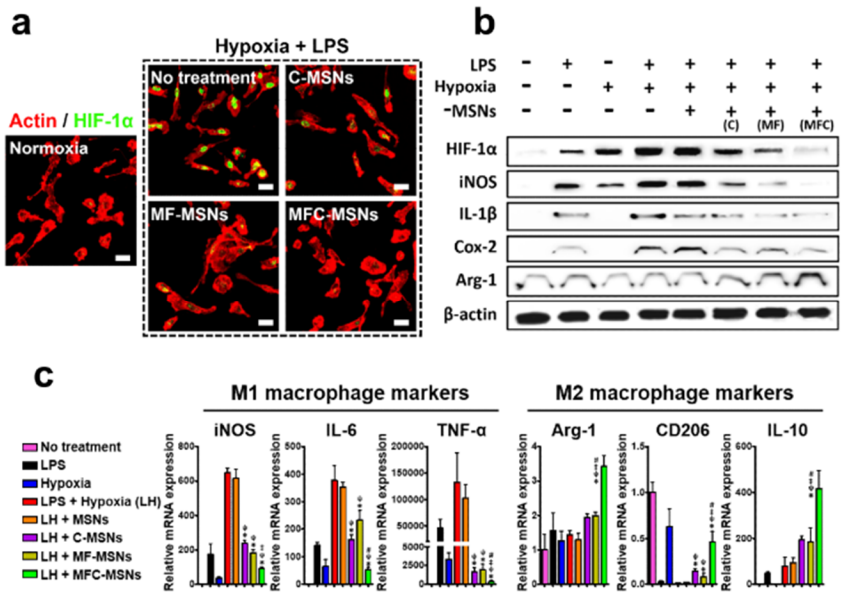

Figure 3.11 (a) HIF-1α (green) staining of BMDMs pretreated with MF-MSNs, C-MSNs, and MFC-MSNs for 4 h and subsequently incubated for 4 h under hypoxic (1% O_2) and inflammatory (+ LPS) conditions. F-actin (red) was stained for visualization of cell structure. Scale bars, 20 μm. (b) Protein expression of HIF1-α, M1 (iNOS, IL-1β, and Cox-2) and M2 (Arg-1) macrophage markers in BMDMs under various conditions, as evaluated by Western blot analysis. (c) mRNA expression of M1 and M2 macrophage markers in BMDMs under various conditions, as evaluated by qRT-PCR analysis (n=3). *, ψ, ‡, and # indicate significant difference as compared to the LH, LH + MSNs, LH + C-MSNs, and LH + MF-MSNs group, respectively ($P < 0.05$).

3.3.3 *In vivo* study of MFC-MSNs

To investigate the *in vivo* effectiveness of MFC-MSNs for RA treatment, we established a rat adjuvant-induced arthritis (AIA) model *via* intradermal injection of complete Freund's adjuvant.[62] It was reported that important pathologic features of human RA, including chronic inflammation and cartilage and bone destruction, are shared in the AIA model.[62] Using the rat AIA model, we first visualized hemoglobin oxygen saturation (sO_2) in the blood of hypoxic knee joints using photoacoustic imaging (**Figure 3.12a**).[63] Intra-articular injection of MFC-MSNs immediately increased sO_2 levels from 17.0 ± 0.7 % to 22.9 ± 1.2 %. This result demonstrates that MFC-MSNs can immediately and efficiently generate O_2 in hypoxic environments. One day after injection, we excised the synovial tissues to track the intracellular fate of MFC-MSNs (**Figure 3.12b**). CLSM images of synovial tissues stained with macrophage-specific F4/80 antibody showed intracellular accumulation of MFC-MSNs in macrophages, likely due to their potent phagocytic ability against foreign materials compared to other immune cells.[64]

We then determined whether O_2 generated by MFC-MSNs alleviates the hypoxia in RA knee joints. Immunohistochemical staining

for HIF-1α in synovial tissues and femurs demonstrated that injection of MFC-MSNs successfully attenuated HIF-1α expression in both synovial and bone tissues (**Figure 3.13**). Furthermore, MFC-MSNs, acting as ROS scavengers and O_2 generators, induced phenotypic alteration of synovial macrophages from the M1 to M2 phenotype in RA knee joints (**Figure 3.14, 3.15**). M1 macrophage-specific biomarkers such as Cox-2, TNF-α, and iNOS were increased after inducing RA, whereas MFC-MSN injection markedly reduced their levels. As expected, RA also stimulated the expression of M2 markers due to macrophage infiltration, but injection of MFC-MSNs additionally upregulated anti-inflammatory M2 markers. Consequently, MFC-MSNs immediately increased hemoglobin sO_2 levels, relieving the hypoxia around RA synovial joints, followed by alteration of macrophage phenotype from pro-inflammatory M1 to the anti-inflammatory M2 subtype.

Based on the unique characteristics of MSNs that make them capable of sustained incorporated drug release,[65-67] we determined whether MFC-MSNs can deliver the anti-rheumatic drug MTX to augment the therapeutic effect. To prevent rapid clearance and severe cytotoxicity caused by repetitive injection of highly concentrated MTX,[64] sustained release of low-dosed MTX would be highly

beneficial for RA treatment. The loading capacity and loading efficiency of MTX were 10.4 μg/mg and 20.8%, respectively. As shown in the release profile of MTX, ~60% of MTX was slowly released over 7 days, demonstrating sustained release (**Figure 3.16**). As inflammation and hypoxia in RA lead to hyperthermia and swelling of paws, thermography was used to assess paw temperature and swelling after administration of MFC-MSNs or MTX-loaded MFC-MSNs. After 30 days, paw temperature and width increased by ~37% and ~120%, respectively, in the PBS-treated group (**Figure 3.17**). In contrast, hyperthermia and paw swelling were dramatically reduced in rats treated with MFC-MSNs and further reduced after MTX-loaded MFC-MSN treatment (**Figure 3.18a, 3.18b**). However, injection of free MTX at a dose equal to that loaded on the MFC-MSNs did not exhibit therapeutic effects against RA, possibly due to the rapid clearance of MTX. Additionally, we performed behavioral tests on RA rats with different treatments by determining the time needed to cross a 70 cm beam. Rats injected with MFC-MSNs or MTX-loaded MFC-MSNs showed markedly reduced times compared with that of the PBS or MTX-injected groups (**Figure 3.18c**).

The therapeutic effect of MFC-MSNs and MTX-loaded MFC-MSNs was further evaluated by histological and immunohistochemical

analyses (**Figure 3.19**). As severe RA results in cartilage destruction, synovial inflammation (synovitis), and stimulated angiogenesis as a response against hypoxia,[62] we evaluated these RA-induced pathological features. Safranin-O staining of the knee joint showed complete destruction of cartilage in the PBS injection group. In contrast, the injection of MFC-MSNs or MTX-loaded MFC-MSNs showed efficient preservation of cartilage structure. Mankin's score was applied for the quantification of cartilage structure. In addition, synovitis was significantly reduced in the MFC-MSN and or MTX-loaded MFC-MSN injection groups as evaluated by H&E staining. Moreover, the number of inflammatory cells was remarkably reduced after treatment with MFC-MSNs or MTX-loaded MFC-MSNs. Finally, angiogenesis, which is a typical response triggered by hypoxia for increasing oxygen supply, was analyzed by immunohistochemical staining of blood vessels with von Willebrand factor (vWF). CLSM and quantification of vWF-positive blood vessels demonstrated that injection of MFC-MSNs or MTX-loaded MFC-MSNs markedly reduced angiogenesis in the knee joint. Overall, our results demonstrate that manganese ferrite, ceria, and MTX in the MTX-loaded MFC-MSNs are synergistic and exhibit an optimal therapeutic effect against RA.

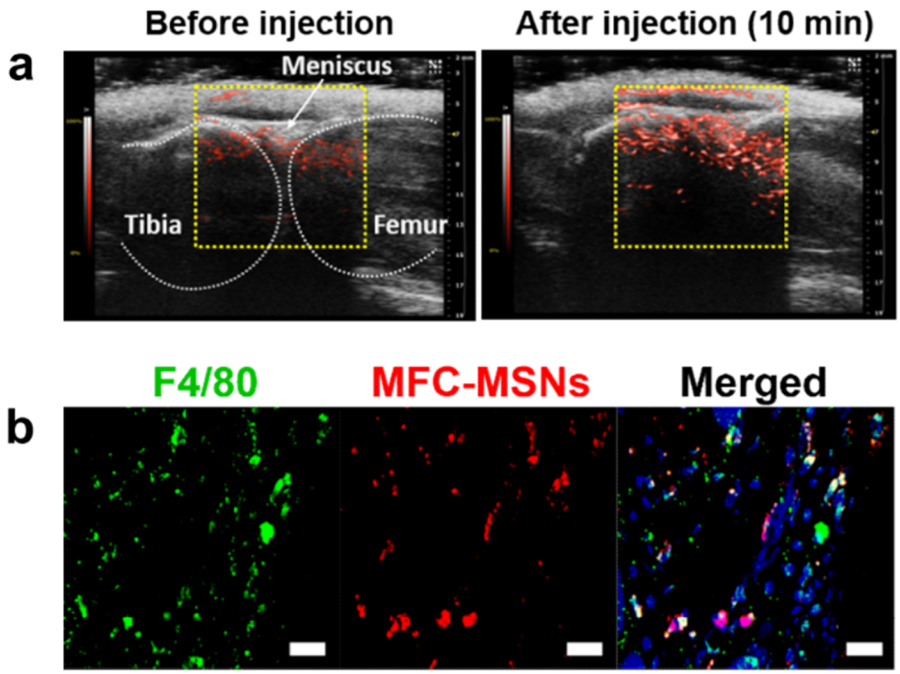

Figure 3.12 (a) Photoacoustic images showing sO_2 (red) in the knee joints before and after intra-articular injection of MFC-MSNs. (b) CLSM images showing the uptake of MFC-MSNs by synovial macrophages stained by macrophage-specific F4/80 antibodies in the knee joint at 3 days after injection. Blue indicates DAPI (nuclei). Scale bars, 20 μm.

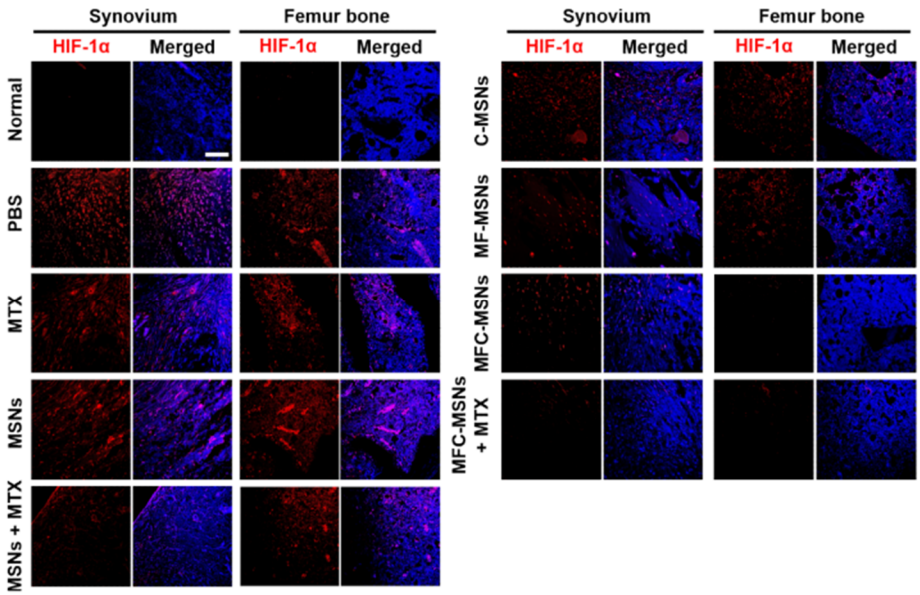

Figure 3.13 IHC staining of HIF-1α in the synovium and femur bone of knee joint after treatment in 8 different experimental groups.

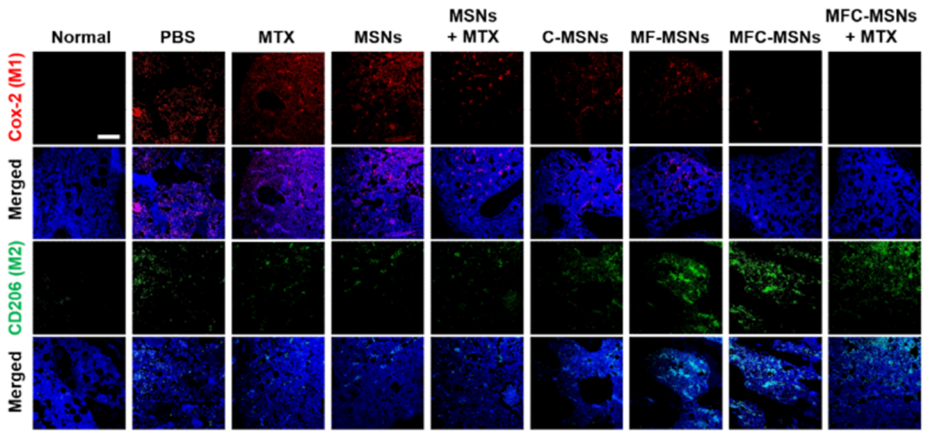

Figure 3.14 IHC staining of M1 (Cox-2) and M2 (CD206) markers in the synovium after treatment in 8 different groups.

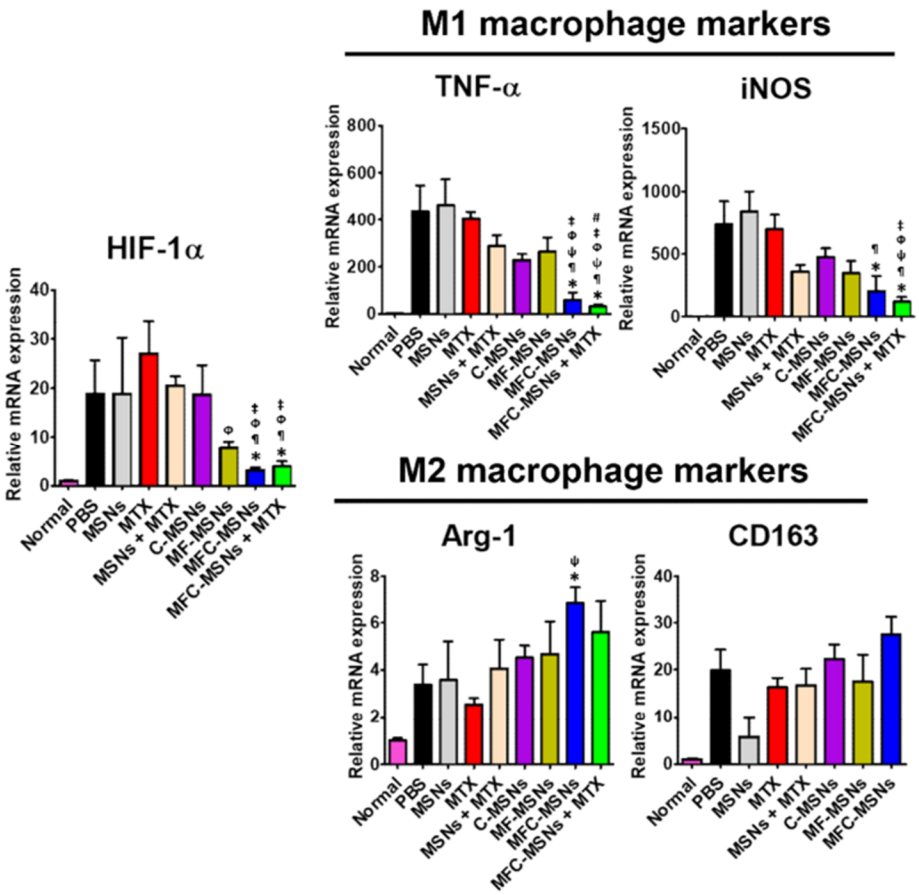

Figure 3.15 qRT-PCR analysis of M1 and M2 markers in isolated knee joint after treatment in 8 different groups (n=3). *, ψ, ¶, Φ, ‡, and # indicate significant difference from PBS, MSNs, MTX, MSNs+MTX, C-MSNs, and MF-MSNs, respectively ($P < 0.05$).

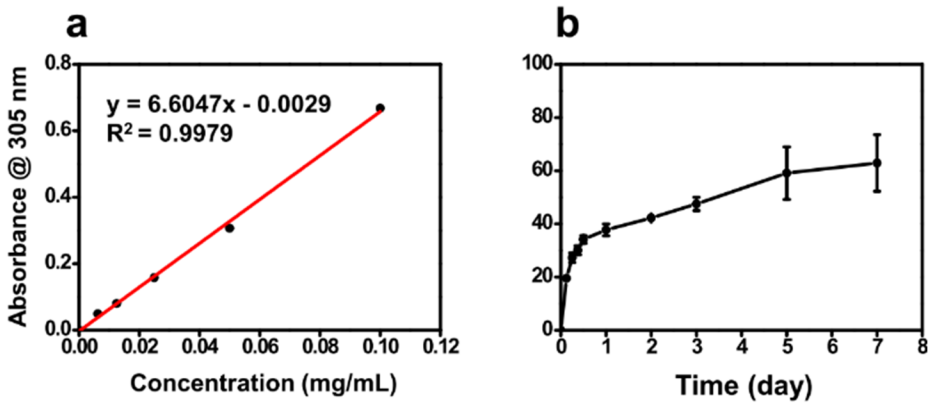

Figure 3.16 (a) Absorbance of MTX at 305 nm in a concentration-dependent manner. (b) Release curve of MTX from MTX-loaded MFC-MSNs (n=3).

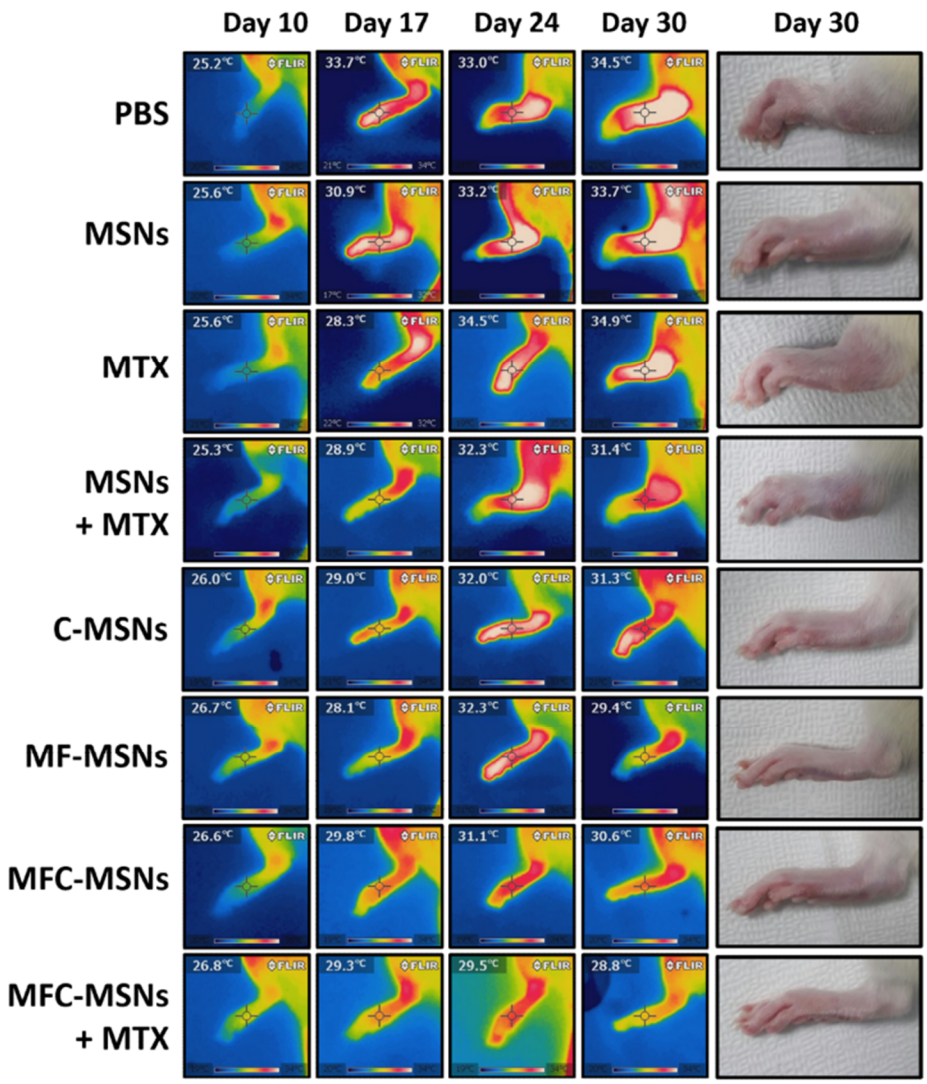

Figure 3.17 Thermographic images of hind paw of rat AIA model in 8 different groups.

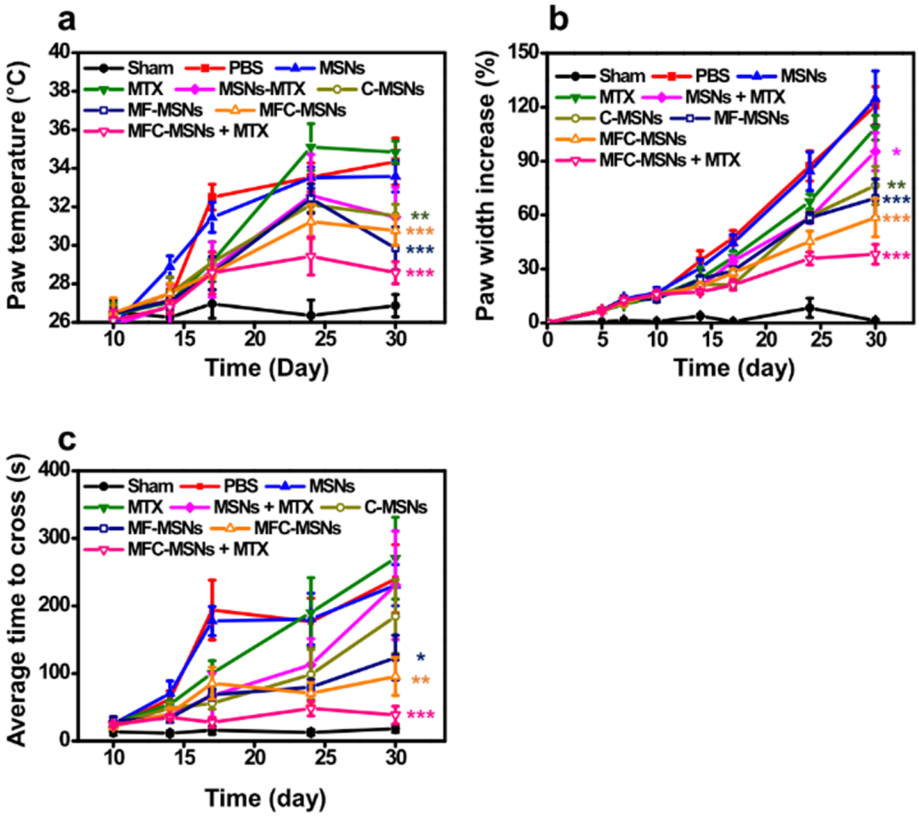

Figure 3.18 Quantification of (a) paw temperature, (b) paw width increase, and (c) average time to cross a beam in 8 different groups (n=6). *$P < 0.05$, **$P < 0.01$, ***$P < 0.001$ versus PBS group.

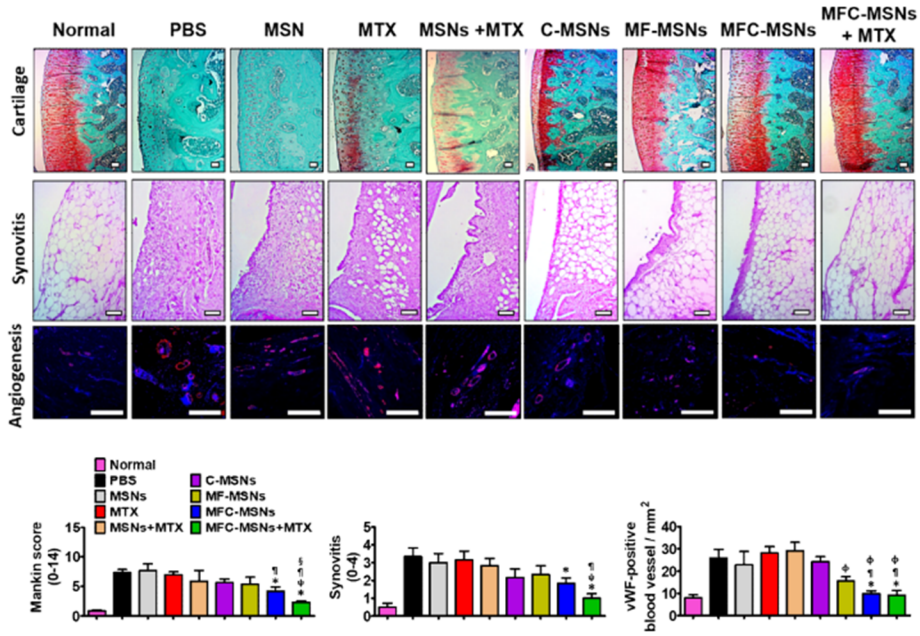

Figure 3.19 (a) Safranin-O staining, H&E staining, and vWF staining of RA knee joint after treatment in 8 different experimental groups, and (b) their corresponding quantifications (n=6). *, ψ, ¶, Φ, ‡, and § indicate significant difference from PBS, MSNs, MTX, MSNs+MTX, C-MSNs, and MFC-MSNs, respectively ($P < 0.05$)

3.4 Conclusion

In summary, we developed MFC-MSNs that can synergistically scavenge ROS and generate O_2 for alleviating inflammation through M1 to M2 polarization of macrophages in RA knee joints. The synergistic effect of manganese ferrite and ceria NPs was attributed to the hydroxyl radical scavenging effect of ceria NPs, whereby intermediate radicals generated by manganese ferrite NPs to O_2. MFC-MSNs successfully induced polarization of M1 to M2 macrophages under hypoxic and inflammatory conditions both *in vitro* and *in vivo*. Intra-articular injection of MFC-MSNs to RA rats successfully oxygenated the inflamed synovial joint, subsequently downregulating HIF-1α and attenuating inflammation through polarization of M1 to M2 macrophages. Anti-rheumatic drug delivery using MFC-MSNs further alleviated RA. This study suggests the potential of MFC-MSNs as an inflammation reliever and M2 macrophage stimulator for treatment of RA and other hypoxia-associated inflammatory disorders such as myocardial infarction.

Most of the contents of this chapter were published in the article, "Synergistic Oxygen Generation of Manganese Ferrite and Ceria Nanoparticles Potentiates M2 Polarization of Macrophages for Rheumatoid Arthritis Treatment." (*ACS Nano* **2018, *submitted.*)

3.5 References

[1] Firestein, G. S., *Nature* **2003,** *423*, 356.

[2] McInnes, I. B.; Schett, G., *Nat. Rev. Immunol.* **2007,** *7*, 429.

[3] Manabe, H.; Nasu, Y.; Komiyama, T.; Furumatsu, T.; Kitamura, A.; Miyazawa, S.; Ninomiya, Y.; Ozaki, T.; Asahara, H.; Nishida, K., *Inflamm. Res.* **2008,** *57*, 4.

[4] Shankar, J.; Thippegowda, P. B.; Kanum, S. A., *Biochem. Biophys. Res. Commun.* **2009,** *387*, 223.

[5] Cramer, T.; Yamanishi, Y.; Clausen, B. E.; Forster, I.; Pawlinski, R.; Mackman, N.; Haase, V. H.; Jaenisch, R.; Corr, M.; Nizet, V.; Firestein, G. S.; Gerber, H. P.; Ferrara, N.; Johnson, R. S., *Cell* **2003,** *112*, 645.

[6] Laria, A.; Lurati, A.; Marrazza, M.; Mazzocchi, D.; Re, K. A.; Scarpellini, M., *J. Inflamm. Res.* **2016,** *9*, 1.

[7] Kim, B.; Pang, H. B.; Kang, J.; Park, J. H.; Ruoslahti, E.; Sailor, M. J., *Nat Commun* **2018,** *9*, 1969.

[8] Davies, L. C.; Jenkins, S. J.; Allen, J. E.; Taylor, P. R., *Nat. Immunol.* **2013,** *14*, 986.

[9] Song, M.; Liu, T.; Shi, C.; Zhang, X.; Chen, X., *ACS Nano* **2016,** *10*, 633.

[10] Marchetti, V.; Yanes, O.; Aguilar, E.; Wang, M.; Friedlander, D.; Moreno,

S.; Storm, K.; Zhan, M.; Naccache, S.; Nemerow, G.; Siuzdak, G.; Friedlander, M., *Sci. Rep.* **2011,** *1*, 76.

[11] Bhattacharya, S.; Aggarwal, A., *Rheumatol. Int.* **2018**.

[12] Hu, X.; Li, P.; Guo, Y.; Wang, H.; Leak, R. K.; Chen, S.; Gao, Y.; Chen, J., *Stroke* **2012,** *43*, 3063.

[13] Brown, B. N.; Ratner, B. D.; Goodman, S. B.; Amar, S.; Badylak, S. F., *Biomaterials* **2012,** *33*, 3792.

[14] Mosser, D. M.; Edwards, J. P., *Nat. Rev. Immunol.* **2008,** *8*, 958.

[15] Wynn, T. A.; Chawla, A.; Pollard, J. W., *Nature* **2013,** *496*, 445.

[16] Arranz, A.; Doxaki, C.; Vergadi, E.; Martinez de la Torre, Y.; Vaporidi, K.; Lagoudaki, E. D.; Ieronymaki, E.; Androulidaki, A.; Venihaki, M.; Margioris, A. N.; Stathopoulos, E. N.; Tsichlis, P. N.; Tsatsanis, C., *Proc. Natl. Acad. Sci. U. S. A.* **2012,** *109*, 9517.

[17] Jeon, C. H.; Ahn, J. K.; Chai, J. Y.; Kim, H. J.; Bae, E. K.; Park, S. H.; Cho, E. Y.; Cha, H. S.; Ahn, K. S.; Koh, E. M., *Clin. Exp. Rheumatol.* **2008,** *26*, 646.

[18] Peters, C. L.; Morris, C. J.; Mapp, P. I.; Blake, D. R.; Lewis, C. E.; Winrow, V. R., *Arthritis Rheum.* **2004,** *50*, 291.

[19] Wang, T.; Liu, H.; Lian, G.; Zhang, S. Y.; Wang, X.; Jiang, C., *Mediators Inflamm.* **2017,** *2017*, 9029327.

[20] Lan, G.; Ni, K.; Xu, Z.; Veroneau, S. S.; Song, Y.; Lin, W., *J. Am. Chem. Soc.* **2018,** *140*, 5670.

[21] Xu, R.; Wang, Y.; Duan, X.; Lu, K.; Micheroni, D.; Hu, A.; Lin, W., *J. Am. Chem. Soc.* **2016,** *138*, 2158.

[22] Sun, X.; Niu, G.; Chan, N.; Shen, B.; Chen, X., *Mol. Imaging Biol.* **2011,** *13*, 399.

[23] Fearon, U.; Canavan, M.; Biniecka, M.; Veale, D. J., *Nat. Rev. Rheumatol.* **2016,** *12*, 385.

[24] Werno, C.; Menrad, H.; Weigert, A.; Dehne, N.; Goerdt, S.; Schledzewski, K.; Kzhyshkowska, J.; Brune, B., *Carcinogenesis* **2010,** *31*, 1863.

[25] Choi, S. H.; Aid, S.; Kim, H. W.; Jackson, S. H.; Bosetti, F., *J. Neurochem.* **2012,** *120*, 292.

[26] Zeng, F.; Wu, Y.; Li, X.; Ge, X.; Guo, Q.; Lou, X.; Cao, Z.; Hu, B.; Long, N. J.; Mao, Y.; Li, C., *Angew. Chem. Int. Ed.* **2018,** *57*, 5808.

[27] Kim, J.; Cho, H. R.; Jeon, H.; Kim, D.; Song, C.; Lee, N.; Choi, S. H.; Hyeon, T., *J. Am. Chem. Soc.* **2017,** *139*, 10992.

[28] Yao, C.; Wang, W.; Wang, P.; Zhao, M.; Li, X.; Zhang, F., *Adv. Mater.* **2018,** *30*.

[29] Huang, C. C.; Chia, W. T.; Chung, M. F.; Lin, K. J.; Hsiao, C. W.; Jin,

C.; Lim, W. H.; Chen, C. C.; Sung, H. W., *J. Am. Chem. Soc.* **2016,** *138*, 5222.

[30] Chen, H.; Tian, J.; He, W.; Guo, Z., *J. Am. Chem. Soc.* **2015,** *137*, 1539.

[31] Li, X.; Kwon, N.; Guo, T.; Liu, Z.; Yoon, J., *Angew. Chem. Int. Ed.* **2018,** *57*, 11522.

[32] Fan, H.; Yan, G.; Zhao, Z.; Hu, X.; Zhang, W.; Liu, H.; Fu, X.; Fu, T.; Zhang, X. B.; Tan, W., *Angew. Chem. Int. Ed.* **2016,** *55*, 5477.

[33] Zhao, Z.; Fan, H.; Zhou, G.; Bai, H.; Liang, H.; Wang, R.; Zhang, X.; Tan, W., *J. Am. Chem. Soc.* **2014,** *136*, 11220.

[34] Qian, C.; Yu, J.; Chen, Y.; Hu, Q.; Xiao, X.; Sun, W.; Wang, C.; Feng, P.; Shen, Q. D.; Gu, Z., *Adv. Mater.* **2016,** *28*, 3313.

[35] Song, G.; Liang, C.; Yi, X.; Zhao, Q.; Cheng, L.; Yang, K.; Liu, Z., *Adv. Mater.* **2016,** *28*, 2716.

[36] Deng, R.; Xie, X.; Vendrell, M.; Chang, Y. T.; Liu, X., *J. Am. Chem. Soc.* **2011,** *133*, 20168.

[37] Chen, Q.; Feng, L.; Liu, J.; Zhu, W.; Dong, Z.; Wu, Y.; Liu, Z., *Adv. Mater.* **2016,** *28*, 7129.

[38] Song, G.; Chen, Y.; Liang, C.; Yi, X.; Liu, J.; Sun, X.; Shen, S.; Yang, K.; Liu, Z., *Adv. Mater.* **2016,** *28*, 7143.

[39] Zhang, Y.; Wang, Z.; Li, X.; Wang, L.; Yin, M.; Wang, L.; Chen, N.; Fan, C.; Song, H., *Adv. Mater.* **2016,** *28*, 1387.

[40] Fan, W.; Bu, W.; Shen, B.; He, Q.; Cui, Z.; Liu, Y.; Zheng, X.; Zhao, K.; Shi, J., *Adv. Mater.* **2015,** *27*, 4155.

[41] Gu, T.; Cheng, L.; Gong, F.; Xu, J.; Li, X.; Han, G.; Liu, Z., *ACS Appl. Mater. Interfaces* **2018,** *10*, 15494.

[42] Kim, C. K.; Kim, T.; Choi, I. Y.; Soh, M.; Kim, D.; Kim, Y. J.; Jang, H.; Yang, H. S.; Kim, J. Y.; Park, H. K.; Park, S. P.; Park, S.; Yu, T.; Yoon, B. W.; Lee, S. H.; Hyeon, T., *Angew. Chem. Int. Ed.* **2012,** *51*, 11039.

[43] Soh, M.; Kang, D. W.; Jeong, H. G.; Kim, D.; Kim, D. Y.; Yang, W.; Song, C.; Baik, S.; Choi, I. Y.; Ki, S. K.; Kwon, H. J.; Kim, T.; Kim, C. K.; Lee, S. H.; Hyeon, T., *Angew. Chem. Int. Ed.* **2017,** *56*, 11399.

[44] Heckert, E. G.; Karakoti, A. S.; Seal, S.; Self, W. T., *Biomaterials* **2008,** *29*, 2705.

[45] Das, S.; Neal, C. J.; Ortiz, J.; Seal, S., *Nanoscale* **2018**.

[46] Celardo, I.; Pedersen, J. Z.; Traversa, E.; Ghibelli, L., *Nanoscale* **2011,** *3*, 1411.

[47] Chen, J.; Patil, S.; Seal, S.; McGinnis, J. F., *Nat. Nanotechnol.* **2006,** *1*, 142.

[48] Kwon, H. J.; Cha, M. Y.; Kim, D.; Kim, D. K.; Soh, M.; Shin, K.; Hyeon, T.; Mook-Jung, I., *ACS Nano* **2016,** *10*, 2860.

[49] Kwon, H. J.; Kim, D.; Seo, K.; Kim, Y. G.; Han, S. I.; Kang, T.; Soh, M.;

Hyeon, T., *Angew. Chem. Int. Ed.* **2018,** *57*, 9408.

[50] Zhang, C.; Bu, W.; Ni, D.; Zhang, S.; Li, Q.; Yao, Z.; Zhang, J.; Yao, H.; Wang, Z.; Shi, J., *Angew. Chem. Int. Ed.* **2016,** *55*, 2101.

[51] Lin, W.; Huang, Y. W.; Zhou, X. D.; Ma, Y., *Int. J. Toxicol.* **2006,** *25*, 451.

[52] Dowding, J. M.; Das, S.; Kumar, A.; Dosani, T.; McCormack, R.; Gupta, A.; Sayle, T. X.; Sayle, D. C.; von Kalm, L.; Seal, S.; Self, W. T., *ACS Nano* **2013,** *7*, 4855.

[53] Park, J.; An, K.; Hwang, Y.; Park, J. G.; Noh, H. J.; Kim, J. Y.; Park, J. H.; Hwang, N. M.; Hyeon, T., *Nat. Mater.* **2004,** *3*, 891.

[54] Pan, L.; He, Q.; Liu, J.; Chen, Y.; Ma, M.; Zhang, L.; Shi, J., *J. Am. Chem. Soc.* **2012,** *134*, 5722.

[55] Boltznitulescu, G.; Wiltschke, C.; Holzinger, C.; Fellinger, A.; Scheiner, O.; Gessl, A.; Forster, O., *J. Leukoc. Biol.* **1987,** *41*, 83.

[56] Bendele, A., *J. Musculoskelet. Neuronal Interact.* **2001,** *1*, 377.

[57] Joe, B.; Griffiths, M. M.; Remmers, E. F.; Wilder, R. L., *Curr. Rheumatol. Rep.* **1999,** *1*, 139.

[58] Schmitz, N.; Laverty, S.; Kraus, V. B.; Aigner, T., *Osteoarthritis Cartilage* **2010,** *18*, S113.

[59] Pritzker, K. P. H.; Gay, S.; Jimenez, S. A.; Ostergaard, K.; Pelletier, J. P.; Revell, P. A.; Salter, D.; van den Berg, W. B., *Osteoarthritis Cartilage* **2006,** *14*,

13.

[60] Yang, J.; Yang, J.; Liang, S. H.; Xu, Y.; Moore, A.; Ran, C., *Sci. Rep.* **2016,** *6*, 35613.

[61] Wittmann, C.; Chockley, P.; Singh, S. K.; Pase, L.; Lieschke, G. J.; Grabher, C., *Adv. Hematol.* **2012,** *2012*, 541471.

[62] Roubenoff, R.; Freeman, L. M.; Smith, D. E.; Abad, L. W.; Dinarello, C. A.; Kehayias, J. J., *Arthritis Rheum.* **1997,** *40*, 534.

[63] Zhang, H. F.; Maslov, K.; Sivaramakrishnan, M.; Stoica, G.; Wang, L. H. V., *Appl. Phys. Lett.* **2007,** *90*.

[64] Wigginton, S. M.; Chu, B. C. F.; Weisman, M. H.; Howell, S. B., *Arthritis Rheum.* **1980,** *23*, 119.

[65] Lee, J. E.; Lee, N.; Kim, T.; Kim, J.; Hyeon, T., *Acc. Chem. Res.* **2011,** *44*, 893.

[66] Wang, W.; Wang, P.; Tang, X.; Elzatahry, A. A.; Wang, S.; Al-Dahyan, D.; Zhao, M.; Yao, C.; Hung, C. T.; Zhu, X.; Zhao, T.; Li, X.; Zhang, F.; Zhao, D., *ACS Cent. Sci.* **2017,** *3*, 839.

[67] Fang, Y.; Zheng, G.; Yang, J.; Tang, H.; Zhang, Y.; Kong, B.; Lv, Y.; Xu, C.; Asiri, A. M.; Zi, J.; Zhang, F.; Zhao, D., *Angew. Chem. Int. Ed.* **2014,** *53*, 5366.

Chapter 4. Enhanced Tumor Penetration of Drug-Loaded Nanoparticles by Click Reaction-Assisted Immune Cell Targeting Strategy

4.1. Introduction

Targeted delivery of engineered nanoparticles (NPs) to tumors has been extensively studied to improve the accuracy of cancer diagnosis and the effectiveness of therapy.[1-2] It is well-known that when systemically administered NPs larger than the renal clearance cut-off of < 4 nm readily accumulate in solid tumors via the enhanced permeability and retention (EPR) effect, which originates from leaky vasculature and defective lymphatic drainage in tumor tissues.[3] However, delivery via the EPR effect (also known as passive targeting) results in a heterogeneous distribution of NPs with accumulation mainly at perivascular sites owing

to limited tumor penetration.[4] Decorating the surface of NPs with tumor-specific ligands can increase their affinity to tumors and retention time. However, ligands increase the overall size of the NPs and limit diffusion.[5] The penetration depth of NPs delivered by these methods remains limited at around 100−300 μm from tumor blood vessels.[6-7] This is because the tumor microenvironment has several barriers preventing effective penetration of NPs, including high interstitial fluid pressure, dense extracellular matrix formation, and heterogeneous permeability of blood vessels.[8] Therefore, there is a need for new strategies that can deliver NPs deep into tumors for more effective treatments.

Circulating cell-mediated drug delivery (also called the Trojan horse strategy) using host cells with specific tumor tropism has been explored to improve the spatial distribution and penetration depth of NPs.[9] Because tumors often occur at sites of chronic inflammation, several types of leukocytes are preferentially recruited to the tumor microenvironment. These cells support tumor survival by inducing tissue remodeling and angiogenesis.[10] Autologous leukocytes, including neutrophils,[11] monocytes,[12] macrophages,[13] and T cells,[14] have been

utilized as active vehicles to deliver NPs to primary and metastatic tumors. Among them, immature myeloid cells, also called myeloid-derived suppressor cells (MDSCs), have emerged as promising cell carriers because MDSCs are typically recruited rapidly at the early stage in various tumor types to protect tumor cells from immune destruction by suppressing T cell function.[15-16] Moreover, MDSCs can infiltrate deep inside tumors far from blood vessels where hypoxia is frequently developed, and are subsequently differentiated into tumor-associated macrophages (TAMs) that show pro-tumoral activities.[17] In breast cancer, TAMs may comprise up to 70% of the tumor mass, and the large number of TAMs in tumor is associated with poor prognosis.[18] Thus, we hypothesized that the therapeutic efficacy of the anti-cancer drug, doxorubicin (DOX), can be augmented if autologous MDSCs are utilized as vehicles to deliver DOX-loaded NPs to tumor interiors where NPs have failed to access by the EPR effect. These MDSCs decorated with NPs can act as local drug depots that release the DOX payload to neighboring tumor cells.[19]

Although the Trojan horse strategy is promising for drug delivery applications, current methods rely on adoptive cell transfer. During this

treatment, target cells extracted from internal organs are expanded and labeled with NPs *ex vivo* in specialized media, and then reinfused into the cancer patients or mouse models as therapeutics.[20] However, cell extraction, expansion and labeling *ex vivo* are time-consuming, and poorly reproducible, preventing practical clinical translation.[21] For innate immune cells, such as neutrophils and monocytes, the survival rate of isolated cells is always less than expected *in vivo*, because these cells have short life spans up to a few hours after isolation.[22] Poor survival rates and targeting efficiency of transferred cells in recipients have been reported because 90% of transplanted cells typically die within a week.[23] To resolve these issues, drug-loaded NPs that can be injected directly into the blood circulation to bind specifically with cell carriers *in vivo* are much needed. However, to achieve *in vivo* conjugation of NPs to MDSCs in circulation and in the tumor microenvironment, a high binding selectivity and specificity is required.

Click chemistry has been used for surface functionalization to enhance selectivity and specificity of NPs because it is a rapid, selective and high-yielding reaction in living systems.[24] Various chemical combinations, including azide-alkyne, thiol-ene, and Diels-Alder, have

been developed for biocompatible copper-free click chemistry.[25] In particular, the [4+2] inverse Diels-Alder cycloaddition reaction between 1,2,4,5-tetrazine (Tz) and *trans*-cyclooctene (TCO) is highly desirable for biomedical applications because this reaction can proceed orders of magnitude faster than other click reactions.[26] When applied to *in vivo* cancer-targeting delivery of NPs, unnatural glycans with click chemistry moieties are firstly introduced onto the surface of tumor cells.[27-28] Subsequent administration of NPs carrying the coupling partner leads to selective conjugation between click chemistry moieties, enhancing tumor-targeting efficiency of NPs. A key challenge with the glycoengineering is the very low delivery efficiency of glycans to tumor tissues.[29] To overcome this, pre-targeting with tumor-specific antibodies containing TCO molecules have been exploited for *in vivo* imaging applications.[30-31] However, no drug-loaded NPs have been conjugated *in vivo* to circulating inflammatory cells using bioorthogonal click chemistry.

Here, we report a click reaction-assisted immune cell targeting (CRAIT) strategy that uses MDSCs as active carriers to deliver DOX-loaded NPs into tumor interiors (**Figure 4.1**). For fast and catalyst-free

reaction *in vivo*, we used Tz/TCO cycloaddition to selectively target drug-loaded NPs to MDSCs in circulation and the tumor microenvironment. Primary administration of CD11b antibodies modified with TCO allows Tz-functionalized mesoporous silica NPs (MSNs-Tz) to be subsequently conjugated onto $CD11b^+$ myeloid cells. Labeled $CD11b^+$ cells are not affected by DOX molecules that are loaded in MSNs, and maintain their mobility toward 4T1 cancer cells *in vitro*. Real-time intravital imaging of 4T1 tumor-bearing mice showed that $CD11b^+$ cells tagged with MSNs-Tz are highly motile, crawling and rolling in tumor vasculatures. $CD11b^+$ cell-mediated delivery showed more uniform distribution and deeper tumor penetration of MSNs-Tz than conventional passive targeting. At the tumor interior, MSNs-Tz delivered by the CRAIT strategy showed much deeper penetration up to 2.5 mm compared to NPs delivered by the EPR effect. Furthermore, DOX delivery rapidly reduced tumor burden in an aggressive 4T1 breast cancer model without any systemic toxicities. Overall, this "immune cell hitchhiking" strategy enabled by *in vivo* click chemistry offers promising opportunities for targeted drug delivery deep inside tumors.

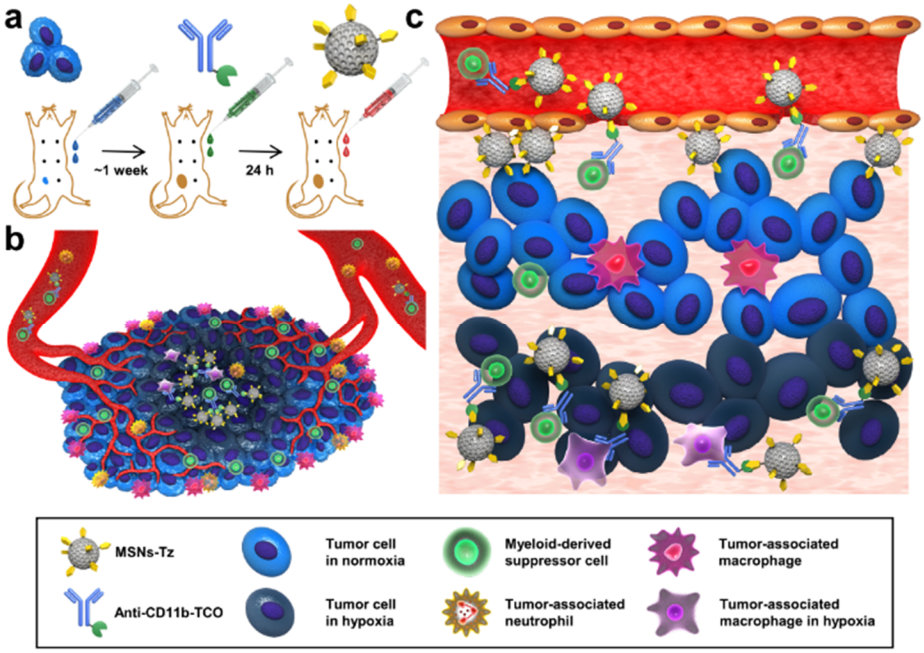

Figure 4.1 (a) Schematic illustrating the CRAIT method applied to an orthotopic 4T1 tumor mouse model. (b) Schematic illustration of the tumor microenvironment which is comprised of heterogeneous $CD11b^+$ inflammatory cells. (c) Schematic illustration of how the CRAIT strategy probes are delivered into tumor interiors. $CD11b^+$ cells in the tumor environment and blood vessels are labeled with anti-CD11b-TCO and subsequently tagged with MSNs-Tz by bioorthogonal click chemistry. The labeled $CD11b^+$ cells transmigrate from blood vessels to the tumor microenvironment and penetrate tumor interiors.

4.2 Experimental Section

4.2.1 Preparation of Tz-functionalized MSNs

fluorenylmethyloxycarbonyl-poly(ethylene oxide) 5K-succinimidyl NHS acid ester (Fmoc-PEG5K-SCM) and methoxy-poly(ethylene oxide) 2K-succinimidyl NHS acid ester (mPEG2K-SCM) were purchased from Creative PEGworks. PEG derivatives were pre-dissolved in dimethylformamide (DMF) at 100 mg ml^{-1}. For PEGlyation, Fmoc-PEG5K-SCM (5 mg) was added to the suspension of amine-functionalized MSNs (20 mg) at 25 ^{o}C, and stirred for 6 h. Then mPEG2K-SCM was added to the reaction mixture without purification, and additionally stirred for 6 h. The products were purified by centrifugation (15000 rpm, 20 min) and re-dispersed in DMF (5 ml). In order to remove Fmoc protecting group, 1 ml of piperidine (Sigma-Aldrich) was added to the products and stirred at 25 ^{o}C for 1 h. After several purification processes by centrifugation, methyltetrazine-PEG4-NHS ester (2.2 mg, Click Chemistry Tools) was added to the reaction mixture at 25^{o}C for 3 h. The mixture was washed with D.I. water and re-dispersed in 5% glucose solution. To determine number of Tz moiety per one MSN, 1ml of MSNs-Tz (4 mg ml^{-1}) was reacted with 200 ul of Cy5-

TCO (1 mg ml^{-1}, Click Chemistry Tools) for 1 h at 25 °C. After several purification processes by centrifugation, the absorption of nanoparticles was characterized by Uv-Vis absorption spectroscopy.

4.2.2 Preparation of TCO-functionalized anti-CD11b

Labeling antibodies with Trans-cyclooctene were adapted from a previously published procedure.[26] Commercially purchased monoclonal antibody (anti-CD11b, Cat#: BE0007, BioXcell) was dissolved in 0.1 M $NaHCO_3$ buffer (pH 8.5) to a final concentration 2 mg ml^{-1}. This solution was incubated with three equivalents of fluorescent succinimidyl ester (Alexa fluor 488, 680, or 750) for 3 h at 25 °C. After incubation, the antibody was purified by centrifuge filtration (Amicon centrifuge filter, Milipore) and stored in phosphate buffered saline (PBS). The concentration of antibody and the number of fluorescence dyes per antibody was confirmed by spectrophotometric analysis (Nanodrop, Thermo Fisher Scientific). All the ratio of antibody and fluorescence dye was tuned to one. To label the fluorescent antibody with *Trans*-Cyclooctene (TCO), the antibody was dissolved in 0.1 M $NaHCO_3$ buffer solution and incubated with TCO-PEG4-NHS (9 equivalents, Click Chemistry Tools) for 13 h at 4 °C. In advance, amine-

reactive TCO-PEG4-NHS was dissolved in anhydrous DMF to a make stock solution (5 mg ml^{-1}). After reaction, the antibodies were purified by centrifuge filtration using PBS and stored at 4ºC. To determine number of TCO moiety per antibody, anti-CD11b-TCO was diluted with PBS (1 mg ml^{-1}) and reacted with Cy3-Tz (2 equivalents, Click chemistry tools) that dissolved in DMF in advance (1mg ml^{-1}). After reaction for 1 h at room temperature, the resulting antibody was purified by centrifuge filtration using PBS. The absorption of the labeled antibody was measured with Uv-Vis absorption spectroscopy (Spectro V-550, Jasco).

4.2.3 Characterization of MSNs-Tz and anti-CD11b-TCO

Transmission electron microscopy (TEM) was performed by using a JEOL JEM-2100F (JEOL) microscope at an acceleration voltage of 200 kV. Fourier-transform infrared (FT-IR) analysis was conducted by a VERTEX80v FT-IR spectrophotometer (Bruker, Germany). Sinapinic acid (Sigma-Aldrich) was used as the MALDI matrix, which was prepared by dissolving 1 mg in 0.1 mL 70:30 acetonitrile/water with 0.1% trifluoroacetic acid. Unmodified and TCO-modified antibodies were diluted to 150 μg mL^{-1} with PBS, combined at a 2:1 ratio with sinapinic acid solution, and 1 μL was dried onto a MALDI sample plate. MALDI-

TOF mass spectrometry was performed on a Voyager-DETM STR Biospectrometry Workstation manufactured by Applied Biosystems Inc. in National Center for inter-University Research Facilities. Hydrodynamic sizes and zeta potentials were measured by dynamic light scattering (Malvern).

To analyze the molecular interaction between anti-CD11b-TCO and MSNs-Tz under physiological conditions, FCCS experiments were performed in 100% FBS at room temperature.[32] 0.5 μM of FITC-labeled anti-CD11b-TCO and 1 μM of RITC-labeled MSNs-Tz dispersed in 100% FBS were incubated for 1 h to induce the click reaction, and cross correlation curves (i.e. two auto correlation curves and one cross correlation curve) based on RITC and FITC were obtained. TCO-omitting group and Tz-omitting group were used as control groups. To study reaction kinetics, 10-fold-diluted anti-CD11b-TCO and MSNs-Tz were mixed and sampled every 10 min. The correlation curves of the samples were immediately obtained by FCCS. Conjugation efficiency of the reaction was measured by calculating the value of relative cross-correlation amplitudes (RCA). Varying the concentration of the antibody from 0.49 μM to 0.12 μM, the RCA value depending on the concentration of the antibody was also measured.

4.2.4 *In vitro* study

Cell viability test: To examine the toxicity of DOX-loaded MSNs-Tz to $CD11b^+$ cells, cell viability was assessed using MTS cell proliferation assay (G3582, Promega). After RAW cells were incubated with various concentrations of anti-CD11b-TCO and DOX-loaded MSNs-Tz for 24 h, MTS solution was added to media and the absorbance was measured at 490 nm using a microplate reader (VICTOR, Perkin-Elmer)

Cell migration assay and phagocytosis assay: Cell migration assay was performed using transwell plates of 8 μm pore size (Corning). 4T1-conditioned media, which was obtained after 24 h incubation with 4T1 cells, was located in the lower compartment. After pre-incubation with anti-CD11b-TCO (0.1 mg ml^{-1}) and MSNs-Tz (0.4 mg ml^{-1}) for 2 h each, RAW cells were incubated on the upper compartment for 24 h. Then, the upper chamber was removed and the migrated cells in the under compartment were observed using microscopy. The relative migration activity was calculated by counting the cells on each group. The ratio of phagocytosed nanoparticles was calculated via trypan blue quenching method. First, RAW cells were incubated with anti-CD11b-TCO and

RITC-MSNs-Tz for 2 h each. After 24 h, RAW cells were washed with PBS several times and 0.4 mg ml^{-1} of trypan blue solution was added. Trypan blue solution was removed after 1 min, and the fluorescence intensity of RITC was measured using a microplate reader before and after trypan blue addition. The percentages of the nanoparticles on cell surface were measured by the ratio of fluorescence intensity differences.

BMDC labeling with click chemistry: Bone-marrow cells were obtained from femurs and tibias, and red cells were removed using ammonium chloride lysis buffer. One million bone marrow cells were cultured in RPMI 1640 medium supplemented with 10% FBS in the presence of 30% v/v 4T1 tumor-conditioned media. Cells (1×10^6/sample) were labeled with anti-CD11b-TCO (25 μg ml^{-1}) in 0.1 ml PBS for 30 min at room temperature. Following centrifugation and aspiration of the antibody solution, antibody-labeled cells were directly re-suspended in of MSNs-Tz (0.8 mg ml^{-1}), incubated for 30 min at room temperature. After washing twice by centrifugation with PBS, the samples were analyzed using FACS Calibur flow cytometer (BD Biosciences) and Flowjo software. For confocal microscopy studies, labeled cells were attached to glass slides with removable chamber wells (Corning). Rhodamine B in MSNs-Tz and fluorescein in anti-CD11b-TCO were

imaged using a multichannel upright laser-scanning confocal microscope (LSM 780 NLO; Carl Zeiss) with a 40× water immersion objective lens. Images were analyzed using ZEN software (Carl Zeiss).

3.2.5 *In vivo* study

Intravital imaging: A plastic frame chamber was produced to study growth and behavior of living cells and tumor implants using confocal microscope. Two plastic frames were implanted into extended double layers of dorsal skin. One layer of the skin was removed of approximately 12 mm in diameter. 4T1-luc2 cells (1×10^5) were implanted at the center of available layer. A cover glass (12 mm) was then placed on the chamber. Finally, the chamber is hermetically closed by second frame. The dorsal skinfold chamber was observed under an LSM 780 NLO microscope (Carl Zeiss, Germany; KBSI Chuncheon Center, Korea). The above 4T1 tumor mouse model for intravital imaging received i.v. injection of anti-CD11b-TCO (200 μg per mouse). After 24 h, MSNs-Tz (0.8 mg per mouse) were injected intravenously to label CD11b+ cells in tumor blood vessels and microenvironments.

In vivo whole-body fluorescence imaging: Balb/C nude mice (n = 4

animals per group) were inoculated with 1 x 10^6 4T1-luc2 cells at mammary gland and then received treatment of CRAIT strategy. The subcutaneous 4T1 tumor model mice were received i.v. injection of anti-CD11b-TCO (200 μg per mouse). After 24 h, MSNs-Tz (25mg kg^{-1}) were injected intravenously and whole-body fluorescence images were obtained over time. The *in vivo* fluorescence tissue imaging was conducted to track the location of cells by using whole body imaging system (IVIS200; Xenogen Corporation, Perkin-Elmer). All animals were anaesthetized in an induction chamber with 2.5% isoflurane in 100% oxygen at a flow rate of 1.0 L min^{-1} for 10 min. For analyses, mice were imaged simultaneously for 1 min using the IVIS system with a 2.0% mixture at 0.5 L min^{-1}, and the regions of interest were quantified with photon flux (p s^{-1}) using Living Image software 4.5 (Perkin-Elmer). The data represent fluorescent signals from an individual mouse, combined from at least two independent studies. For the ex vivo analyses, each organ (heart, lung, liver, spleen, kidney, and tumor) was dissected after completing euthanasia.

In vivo toxicity evaluation of MSNs-Tz: For *in vivo* toxicity studies, major organs including heart, lung, liver, spleen, kidney, and blood were

extracted from mice at 7 days after intravenous administration of the MSNs-Tz (n=5 animals per group). Organ toxicities were investigated by using hematoxylin and eosin (HHS16, HT110180, Sigma Aldrich) staining. After collecting 1 ml blood samples from mice heart, serum biochemistry was examined to assess liver function (ALP, AST and ALT), and kidney function (BUN, and CREA) by using blood chemical analyzer (BS400; Mindray).

4.3 Result and Discussion

4.3.1 Synthesis and Characterization of MSNs-Tz and anti-CD11b-TCO

MDSCs can have either a monocytic ($CD11b^+$ $Ly6^+$ $Ly6G^-$) or polymorphonuclear morphology ($CD11b^+$ $Ly6C^{low}$ $Ly6G^+$) with different levels of surface proteins.[33] To identify the antibody that targets the surface of MDSCs in tumor most efficiently, we functionalized anti-CD11b, anti-Ly6G and anti-Ly6C antibodies with near infrared (NIR) fluorescent dye, Alexa Fluor 680, and intravenously injected them into 4T1 breast tumor-bearing mice (**Figure 4.2a**). Among them, anti-CD11b antibodies showed the greatest accumulation in whole tumor regions after 24 h. *Ex vivo* immunohistochemical staining of the tumor slice showed that $CD11b^+$ cells distribute uniformly in both the periphery and interior of the tumor, suggesting that CD11b integrin on the surface of MDSCs is a good target for 4T1 breast tumor microenvironment (**Figure 4.2b**).

We synthesized MSNs-Tz using a multi-step procedure (**Figure 4.3a**). Fluorescent dyes for imaging were encapsulated within the silica

matrix of the MSN and DOX was loaded inside the mesopores. To prevent NP uptake by the mononuclear phagocyte system, the MSN surface was functionalized with a polyethylene glycol (PEG) layer. Subsequent addition of Tz molecules at the terminal end of the PEG layer allows quick access to the TCO-functionalized antibodies. All the MSN derivatives were characterized using zeta potential and Fourier transform infrared (FT-IR) spectroscopy (**Figure 4.3b, 4.3c**), confirming successful surface functionalization. Transmission electron microscopy images show that MSNs-Tz have spherical mesoporous nanostructures (**Figure 4.4a**), and the number average hydrodynamic diameter is 66 nm as determined by dynamic light scattering (**Figure 4.4b**). Because large number of Tz molecules decorating the surface can increase the hydrodynamic diameters of the MSN-Tz, the degree of Tz functionalization was optimized to keep the overall size below 100 nm. Colloidal stability of MSNs-Tz in biological media was investigated by fluorescence correlation spectroscopy (FCS).[32] MSN-Tz incubated for 24 h in 10% fetal bovine serum (FBS) cell media or PBS showed nearly identical FCS curves, demonstrating excellent colloidal stability of MSNs-Tz (**Figure 4.3d**). UV-Vis absorption spectroscopy confirms that the optimum number of Tz on the MSN surface that would allow TCO

molecules to react readily is 77 molecules per MSN particle (**Figure 4.4c, 4.4d**). Fluorescent MSNs-Tz were prepared by encapsulating rhodamine B isothiocyanate in the silica matrix of MSN, and the synthesized MSNs-Tz show typical absorption and emission peaks at 561 nm and 587 nm, respectively (**Figure 4.4e, 4.4f**). DOX was incorporated into MSNs-Tz by physical adsorption. Under simulated *in vivo* conditions, the DOX payload was released slowly and gradually over a 12 h period (**Figure 4.5**).

Anti-CD11b antibodies were modified with TCO and fluorescent dye (Alexa Fluor 488, **Figure 4.6a**). Each antibody was functionalized with three TCO groups as confirmed by matrix-assisted laser desorption/ionization time of flight (MALDI-TOF) mass spectrometry (**Figure 4.6b**). UV-Vis absorption spectroscopy shows that when anti-CD11b-TCO was incubated with excess amounts of Tz-Cy3 molecules, a fast and selective click reaction occurs between Tz and TCO (**Figure 4.6c**). To investigate click reaction between MSNs-Tz and anti-CD11b-TCO, they were mixed together and subsequently characterized by photoluminescence spectroscopy (**Figure 4.6d**). The emission intensity of MSNs-Tz before click reaction is low because the emission of rhodamine B within MSNs is partially quenched by Tz molecules on the

surface.[26] After click reaction with anti-CD11b-TCO, emission intensity increases 1.7 fold because the resulting cyclic alkene does not absorb the emission of rhodamine B dyes.

The kinetics of click reaction between MSNs-Tz and anti-CD11b-TCO was investigated using dual color fluorescence cross-correlation spectroscopy (FCCS), which can sensitively quantify the interactions between two spectrally distinct fluorophores[34] and analyze the kinetics of addition reactions in real time, where chemical linkages are formed.[35] To investigate the bioorthogonal reaction in the presence of serum proteins, fluorescent MSNs-Tz and anti-CD11b-TCO were reacted in 100% FBS at room temperature to simulate *in vivo* condition, followed by FCCS measurements every 10 min. Control reactions with MSNs without Tz (Tz-omitting MSNs, **Figure 4.7a**) and anti-CD11b without TCO (TCO-omitting, **Figure 4.7b**) showed very weak cross-correlation, because of the lack of specific reactions between MSNs and anti-CD11b. In contrast, strong cross-correlation was observed between MSNs-Tz and anti-CD11b-TCO, providing a clear evidence for selective reaction in complex biological media (**Figure 4.7c**). The antibody-MSN conjugates exhibit a diffusion coefficient (D = 1.42 $\mu m^2\ s^{-1}$) that is similar to MSNs-Tz (D = 1.24 $\mu m^2\ s^{-1}$), suggesting that no aggregation

occurred. During the click reaction, the relative cross-correlation amplitude increased successively within 1 h and subsequently remained constant (**Figure 4.7d**). Using this technique, we also verified *in vitro* reaction kinetics of MSNs-Tz by incubating them with different concentrations of anti-CD11b-TCO. Initial reaction rates increased as anti-CD11b-TCO was added (**Figure 4.7e**), and the relative cross-correlation amplitude approached a plateau value after 40 min, indicating that click reaction was complete within 40 min (**Figure 4.7f**). These FCCS results suggest that anti-CD11b-TCO decorated on the surfaces of the $CD11b^+$ myeloid cell can be coupled with MSNs-Tz rapidly via bioorthogonal click reaction.

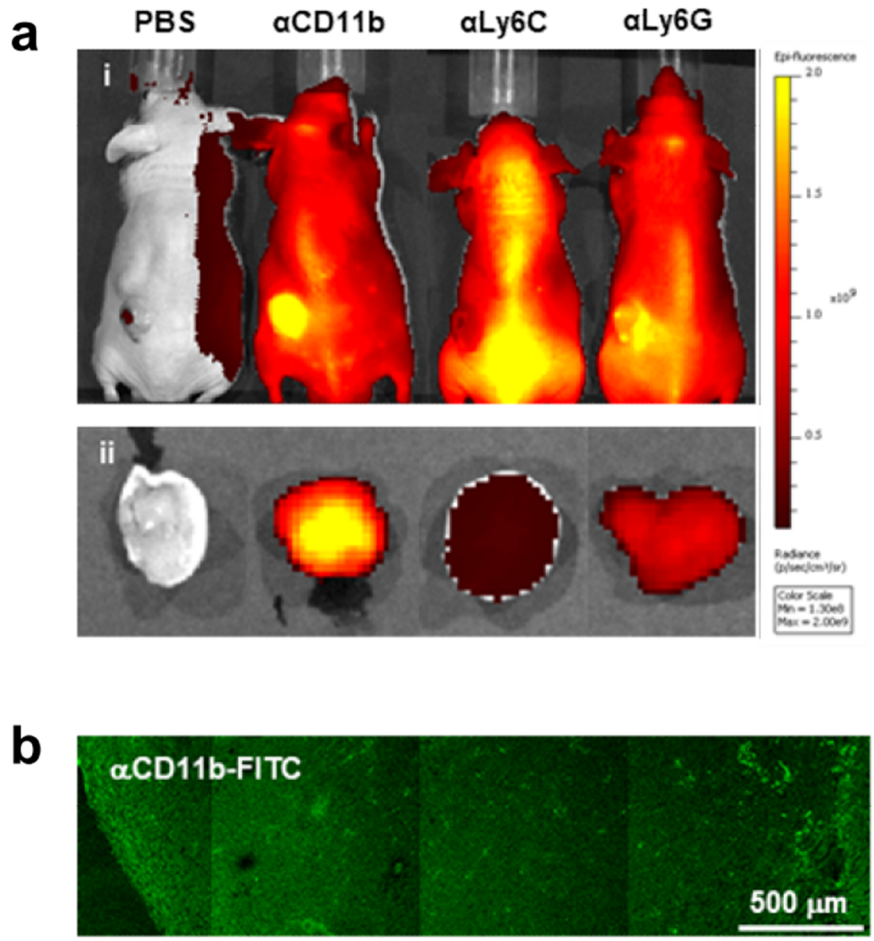

Figure 4.2 (a) IVIS images of subcutaneous 4T1 tumor-bearing mice which were i.v. injected with Alexa Fluor 680-labeled αCD11b, αLy6C, and αLy6G antibodies. (b) *Ex vivo* immunohistochemistry analysis of 4T1 tumor slices that show $CD11b^{+}$ cells are uniformly distributed from tumor periphery to interior regions.

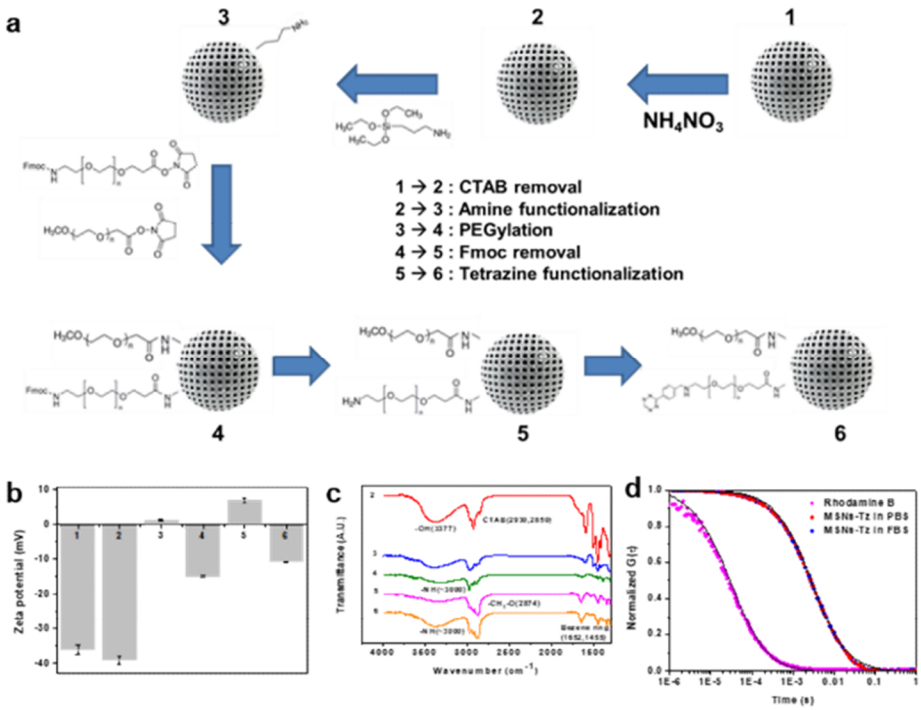

Figure 4.3 (a) Synthetic procedure of MSNs-Tz. (b) Zeta potentials and (c) FT-IR spectra of MSNs-Tz for each synthetic step, demonstrating the successful surface functionalization. (d) Normalized FCS curves of free rhodamine B dye and MSNs-Tz 24 h after in PBS and FBS, showing the excellent colloidal stability of MSNs-Tz.

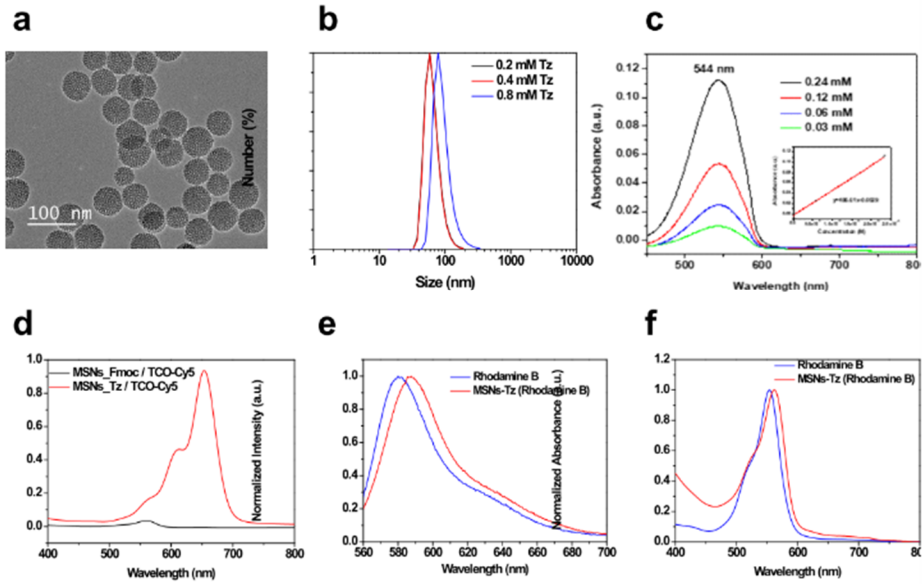

Figure 4.4 (a) TEM image of MSNs-Tz. (b) Number average hydrodynamic diameters of MSNs-Tz functionalized with different concentration of Tz molecules. (c) Quantitative analysis of the number of Tz molecules on the surface of MSNs, as determined by UV-Vis absorption spectroscopy. (d) Absorption spectra of MSNs after treatment of excess Cy5-labeled TCO molecules. (e) Photoluminescence and (f) absorption spectra of free rhodamine B and rhodamine B-incorporated MSNs-Tz.

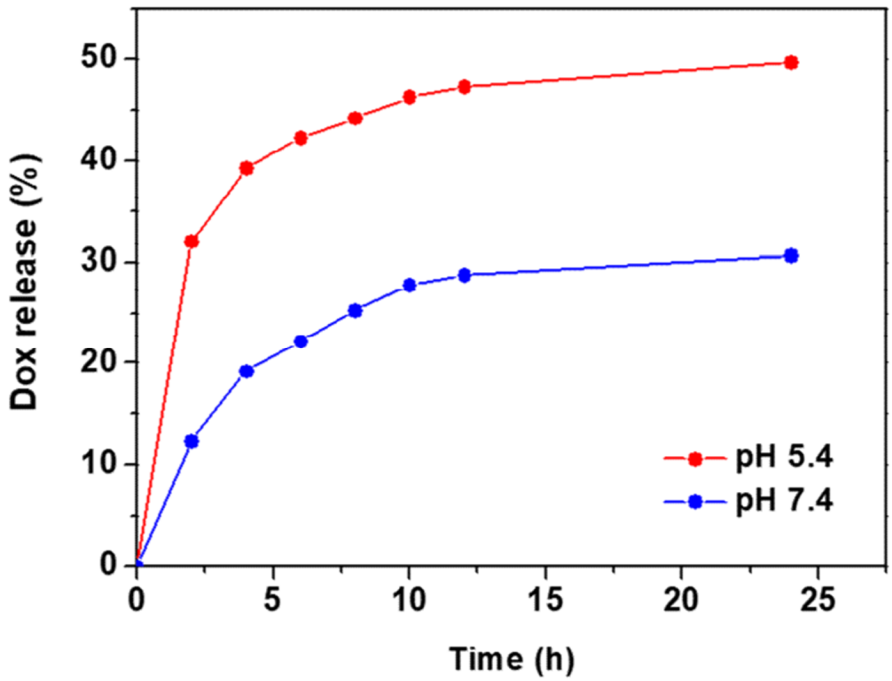

Figure 4.5 Cumulative release profile of DOX from DOX-loaded MSNs-Tz under pH 7.4 and pH 5.4.

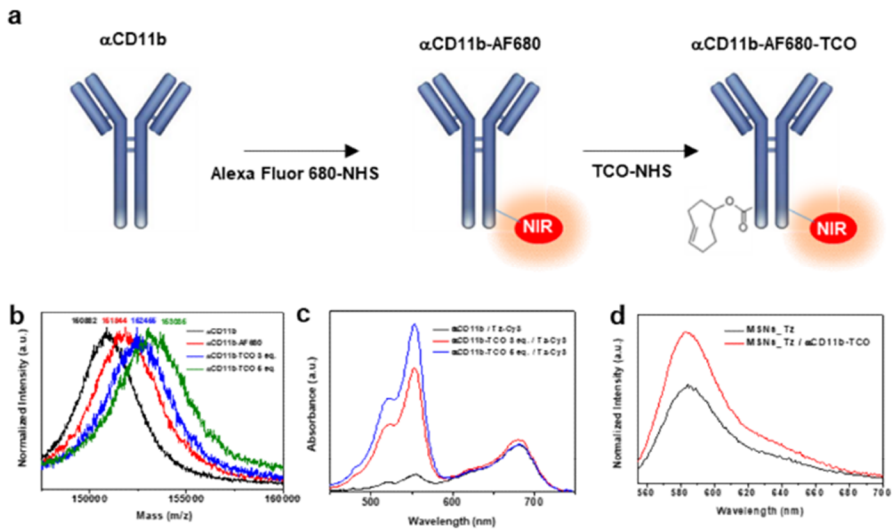

Figure 4.6 (a) Synthetic procedure of anti-CD11b antibodies functionalized with NIR dye and TCO. (b) MALDI-TOF analysis of anti-CD11b-TCO for each synthetic step. (c) Absorption spectra of anti-CD11b-TCO incubated with excess amount of Cy3-labeled Tz molecules. (d) Emission spectra of MSNs-Tz before and after the click reaction.

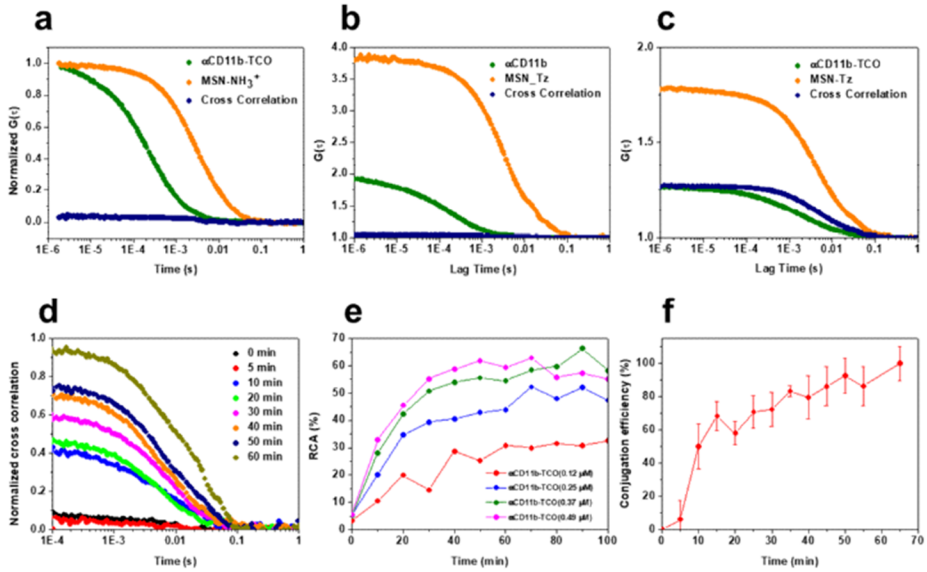

Figure 4.7 (a) Cross correlation curve between anti-CD11b-TCO and MSN-NH3+. Cross correlation curves between anti-CD11b-TCO and MSNs in the (b) absence and (c) presence of Tz molecules under 100% FBS media. (d) Changes of the cross correlation curve between anti-CD11b-TCO and MSNs-Tz in a time-dependent manner. (e) Time changes of relative cross correlation amplitude (RCA) values obtained from cross correlation curves between MSNs-Tz and anti-CD11b-TCO. (f) Time-dependent conjugation efficiency as determined by relative RCA value.

4.3.2 Targeting CD11b$^+$ cells using the CRAIT strategy

Because DOX molecules can be toxic to normal cells, we investigated whether CD11b$^+$ myeloid cells tagged with DOX-loaded MSNs-Tz remain viable and protected from any DOX molecules that may be released before reaching the tumor microenvironment. RAW 264.7 cells were tagged with anti-CD11b-TCO and subsequently conjugated with DOX-loaded MSNs-Tz. The DOX-loaded MSNs-Tz have negligible toxicity toward RAW cells at DOX concentration as high as 2 μg ml^{-1} (**Figure 4.8a**), demonstrating that CD11b$^+$ myeloid cells can carry therapeutic doses of DOX without suffering from apoptosis themselves. Trypan blue quenching experiments show that around 80% of MSNs-Tz bound to the RAW cells localized at the cell surface even after 6 h incubation (**Figure 4.8b**). This reduced and delayed internalization capability of phagocytic RAW cells is likely due to the surface CD11b/CD18 integrin, which is known to promote the internalization of various extracellular pathogens during infection.[36-37] Although the CD11b antibodies appear to delay the uptake of MSNs-Tz, most of MSNs-Tz were internalized after 24 h. We also investigated the influence of the CRAIT method on RAW cell transmigration, which is a key capability of drug-loaded cells to infiltrate tumor microenvironments.

The well-established *in vitro* transwell co-culture system was used to evaluate the migration of RAW cells conjugated with MSNs-Tz in response to chemo-attractants derived from 4T1 tumor cells. The conjugated cells exhibited similar migration capability to unmodified cells, showing that conjugation with MSNs-Tz does not affect cell migration (**Figure 4.8c**).

To investigate the feasibility of the CRAIT strategy *in vitro*, we performed confocal microscopy on endogenous bone marrow cells of 4T1-tumor bearing mouse because the number of $CD11b^+$ MDSCs increases in the bone marrow as tumor progresses.[33] Co-localization of fluorescent signals from anti-CD11b-TCO and MSNs-Tz were detected on the surface of bone marrow cells (**Figure 4.8d**). Control experiments using antibodies without TCO or MSNs without Tz exhibited only fluorescent signals from antibodies on the cell surface, demonstrating minimal nonspecific binding of MSNs-Tz to the bone marrow cells.

Using real-time fluorescence intravital microscopy in a dorsal window chamber, we studied the feasibility of the CRAIT strategy *in vivo*. After the window chamber implantations, 4T1-tumor cells with firefly luciferase gene (4T1-Luc2) were implanted under the window, and the exact position of tumor cells was confirmed by *in vivo*

fluorescence imaging (**Figure 4.9a**). Mice bearing 4T1-Luc2 tumors were intravenously injected first with anti-CD11b-TCO. After 24 h to allow the antibodies to pre-target $CD11b^+$ cells or to be cleared from blood circulation, the mice were administered with MSNs-Tz via tail vein (25 mg kg^{-1}). Intravital imaging after the injection of MSNs-Tz clearly reveals abnormal tumor vessels including irregular and distorted structures owing to excessive angiogenesis (**Figure 4.9b**).[8] Furthermore, because CD11b antibody recognizes a heterogeneous population of myeloid cells, including monocytes, neutrophils, and macrophages, two types of motile behaviors were observed in $CD11b^+$ cells. One population, which has low motility, clustered mainly in delimited foci adjacent to the tumor vasculatures, and these cells can be assigned to TAMs (**Figure 4.9c**).[19] The other population of cells showed highly motile behavior and can be assigned to monocyte or neutrophil. Real-time intravital imaging observations demonstrate that motile $CD11b^+$ cells in blood vessels are brightly stained with both fluorescent antibodies and MSNs-Tz (**Figure 4.10a**), indicating a chemo-selective and bioorthogonal reaction *in vivo*. Fluorescence from MSNs-Tz in blood vessels was undetectable 24 h after injection of MSNs-Tz but accumulated in TAMs, which are major phagocytic cells responsible for

significant uptake of injected NPs (**Figure 4.10b**).[19] Notably, the $CD11b^+$ cells tagged with MSNs-Tz continued to roll in tumor vasculature past 24 h, suggesting that the cell-mediated delivery of MSNs-Tz is possible even after the NPs are cleared from circulation (**Figure 4.10c**). Considering that $CD11b^+$ myeloid cells are continuously recruited into the tumor during tumor progression, delivery of MSNs-Tz using the CRAIT method appears to be independent of the EPR effect and circulation time of MSNs-Tz. When the mice received an injection of antibodies without the TCO moiety in a control experiment, no co-localization of the CD11b antibodies and MSNs-Tz was observed. Instead, vascular bursts followed by eruption of MSNs-Tz into the tumor interstitial space were seen as reported previously and described as the underlying mechanism of the EPR effect (**Figure 4.10d**).[38] Similar to the previous reports, MSNs-Tz extravasate into the tumor interstitial space with a penetration depth of up to ~40 μm from the blood vessel.[4, 38] Together, these confocal and intravital imaging data show that pretargeting with CD11b antibodies and subsequent conjugation of MSNs-Tz by click reaction can selectively target circulating $CD11b^+$ cells *in vitro* and *in vivo*. Furthermore, MSNs-Tz can be delivered to tumor sites via both the EPR effect and tagged $CD11b^+$ cells.

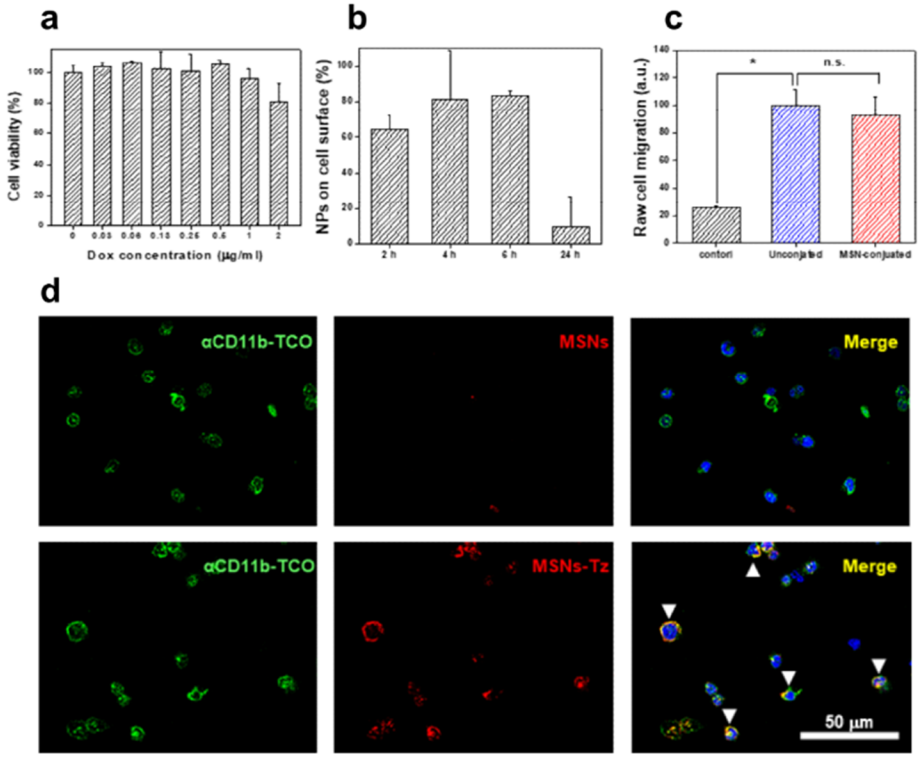

Figure 4.8 (a) Evaluation of in vitro cytotoxicity of DOX-loaded MSNs-Tz on RAW cells using MTS assay. (b) Trypan blue assay showing that 80% of MSNs-Tz remained on the cell surface after 6 h incubation. (c) Evaluation of transmigration capability of RAW cells tagged with anti-CD11b-TCO and MSNs-Tz using transwell chamber. (d) CLSM images demonstrating the targeting of MSNs-Tz (red) to anti-CD11b-TCO (green) on the surface of bone marrow cells (bottom row). Data represent the mean ± S.D. and *$P < 0.05$ by one-way ANONA with Tukey post-hoc test, n.s., not significant, $P = 0.684$.

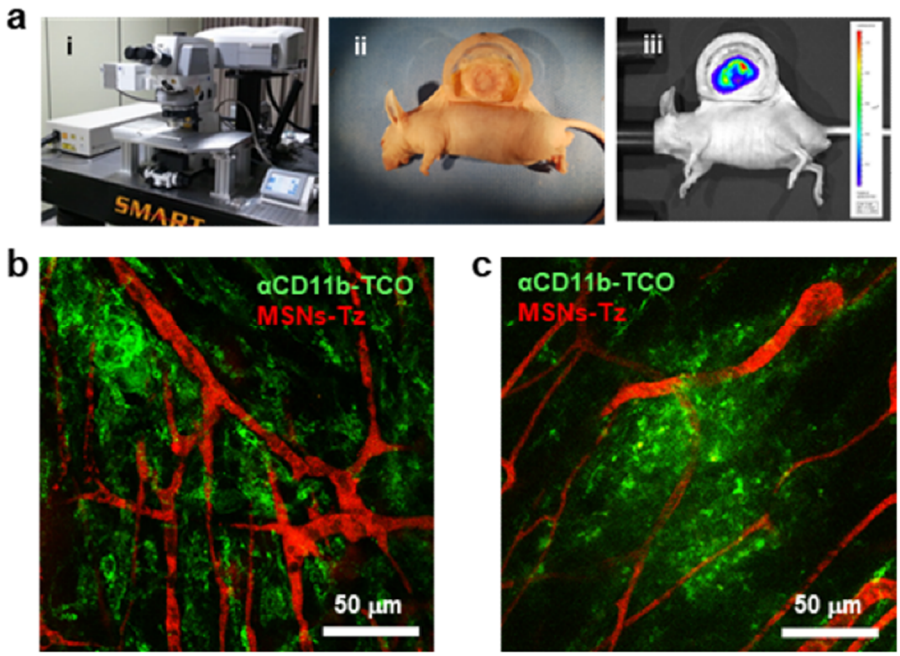

Figure 4.9 (a) Experimental setup for intravital microscopic imaging of 4T1-tumor cells implanted in the mouse. (b) Intravital imaging of abnormal tumor blood vessels that were stained with MSNs-Tz (red).

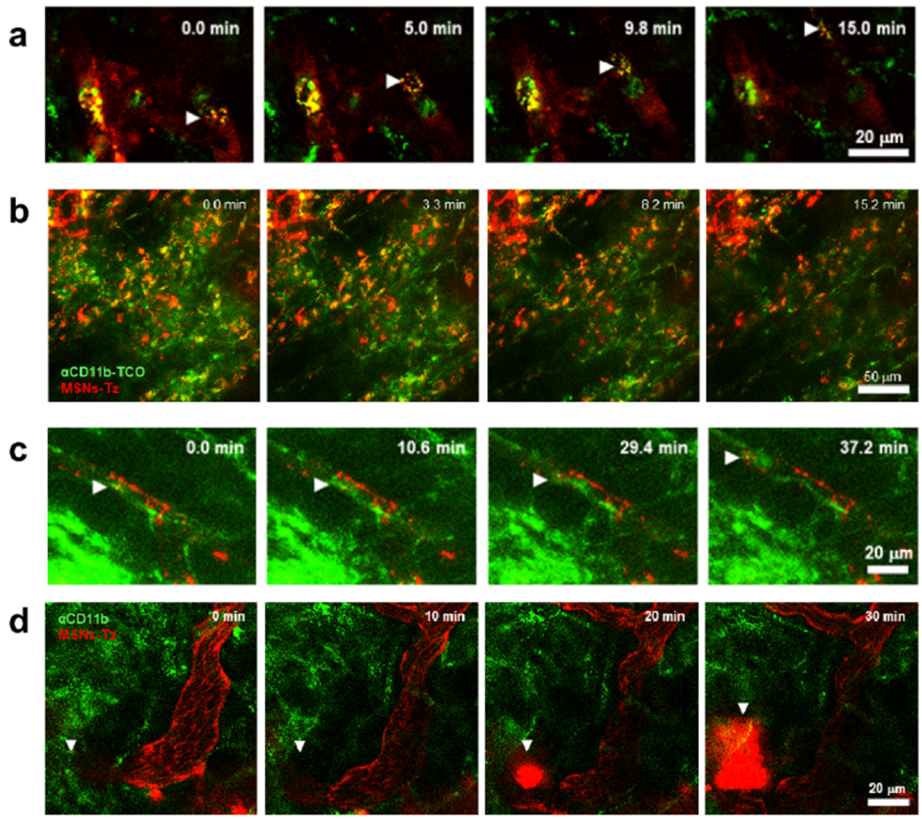

Figure 4.10 (a) Still frames from intravital imaging of tumor blood vessels in 4T1 tumor-bearing mice injected with anti-CD11b-TCO (green) followed by MSNs-Tz (red) after 3 h. (b, c) Intravital imaging 24 h after injection of MSNs-Tz in 4T1 tumor mouse model. (d) Vascular burst followed by an eruption of the MSNs-Tz into tumor interstitial space, which was observed in a 4T1-bearing mouse receiving anti-CD11b and subsequent MSNs-Tz.

4.3.3 Deep tissue penetration of DOX-loaded MSNs-Tz using the CRAIT method

We next tested whether $CD11b^+$ myeloid cells tagged by the CRAIT method can transport DOX-loaded MSNs-Tz into tumor *in vivo*. For more sensitive *in vivo* fluorescence imaging in the NIR range, the fluorophores of anti-CD11b-TCO and MSNs-Tz were modified with Alexa Fluor 750 and Cy5, respectively. Balb/c nude mice bearing orthotopic 4T1 tumor on mammary pads were systemically injected with (1) PBS/MSNs-Tz (nontargeted control group), (2) TCO::Tz complex (preconjugated group, Supplementary Fig. 11), (3) αCD11b/MSNs-Tz (TCO-omitting group), and (4) αCD11b-TCO/MSNs-Tz (CRAIT group) via tail vein. The interval between two successive injections is 24 h. After successive injections, *in vivo* biodistribution of the anti-CD11b-TCO (**Figure 4.11**) and MSNs-Tz (**Figure 4.12a**) were monitored by time-gated fluorescence imaging. Biodistribution studies on anti-CD11b and anti-CD11b-TCO show similar accumulation in tumor, spleen, and liver after 24 h, confirming that TCO modification does not affect the targeting capability of the antibody (**Figure 4.12b**). MSNs-Tz delivered by the CRAIT strategy accumulated in tumors at higher levels than the preconjugated group and TCO-omitting group, but showed similar

intratumoral accumulation to the nontargeted group (**Figure 4.12c**). This similar intratumoral accumulation of the nontargeted group and the CRAIT group indicates that the CRAIT strategy does not increase quantity of MSN-Tz delivery to tumor in comparison to delivery by the EPR effect. However, most of delivered MSN-Tz by the EPR effect is located near tumor periphery, because tumor blood vessels are more abundant at the tumor-host interfaces than in internal regions.[39] The preconjugated group, where MSNs-Tz react with anti-CD11b-TCO before the intravenous injection, showed the lowest tumor accumulation, which is likely due to rapid clearance by the reticuloendothelial system (RES).[1] Consequently, they fail to reach the tumor because covalent attachment of antibodies on the MSN surface can increase its overall size.[2] Furthermore, CD11b conjugation likely accelerates hepatic elimination because Kupffer cells in the liver also express CD11b integrin on their surface.[40] These results suggest that the CRAIT method delivers MSNs-Tz onto circulating $CD11b^+$ cells more effectively than active targeting strategies.

The lower tumor uptake of MSNs-Tz in TCO-omitting group compared to that of the CRAIT group can be attributed to neutralization effect of anti-CD11b on the phagocytic activity of TAMs.[19, 37] CD11b

antibodies used in this study are targeted to the α−subunit of the predominant β_2 integrin expressed mainly on monocytes, macrophages, and granulocytes.[41] Previously, it was shown that *in vivo* administration of the CD11b antibodies inhibits uptake of iron oxide NPs into monocytes and macrophages.[42] Because tumor accumulation of injected NPs increases with the level of TAMs in the tumor interstitium,[43] pre-targeting with anti-CD11b induces a negative effect on intratumoral accumulation of MSNs-Tz. In the case of the CRAIT group, the negative effect associated with pre-targeting was reduced by the improved binding between CD11b antibodies and MSNs-Tz via click chemistry. Because labeled CD11b antibody scaffold has an average of three anchoring sites for subsequent click chemistry reaction, multiple MSNs-Tz can be attached to one antibody, thereby amplifying the payload of NPs in the tumor mass. In addition, examining the difference in the fluorescence signal between the TCO-omitting and CRAIT groups 24 h after injection, we estimate that nearly 37% of MSNs-Tz that are accumulated in the tumor is delivered by the CRAIT method and the rest appears to depend on conventional mechanisms such as extravasation and/or phagocytosis by TAMs. *Ex vivo* fluorescence microscopy images obtained from tumor slices reveal that MSNs-Tz in the CRAIT group are

co-localized with anti-CD11b-TCO, whereas no co-localization is observed in the TCO-omitting group (**Figure 4.12d, 4.13**).

To evaluate tumor penetration and distribution of MSNs-Tz, tumors were excised after 24 h and accumulation profile analysis was performed on the *ex vivo* histological specimens (**Figure 4.13a**). From the representative tumor sections, MSNs-Tz in the CRAIT group exhibited more uniform distribution and deeper penetration than the nontargeted group (**Figure 4.13b**). MSNs-Tz delivered by the CRAIT method were found both in the peripheral and interior regions of tumors, while the nontargeted MSNs-Tz were predominantly localized at the tumor periphery (**Figure 4.14**). To quantify the penetration depth of MSNs-Tz, fluorescence intensities from tumor surface to central region were obtained (**Figure 4.13c**). In the case of the nontargeted group, about 55% of overall fluorescence intensity was detected between tumor surface and 1 mm from tumor surface. Only 14% was observed between 2 mm and 3 mm from tumor surface, suggesting that their penetration is limited to tumor periphery. In contrast, about 35% of overall fluorescence intensity was observed between 2 mm and 3 mm from tumor surface in the CRAIT group. Considering that tumor diameter is almost 5 mm, MSNs-Tz delivered by the CRAIT method can penetrate up to ~2.5 mm from the

tumor surface, corresponding to tumor interiors. At the tumor interior regions, MSNs-Tz delivered by the CRAIT method exhibited ~5-fold higher fluorescence intensity than that delivered by the nontargeted group. Deep tumor penetration of MSNs-Tz in the CRAIT group can be attributed to the infiltration of labeled $CD11b^+$ cells into tumor interiors, where hypoxic tumor cells secrete lysyl oxidase to recruit $CD11b^+$ myeloid cells[49]. This deep penetration implies that the CRAIT method can deliver drugs into hypoxic regions, which are not accessible by conventional passive- and active-targeting approaches. Finally, to exclude the possibility of MSNs-Tz displacement during the slide preparation, three dimensional confocal images were obtained. The image exhibited evenly dispersed MSNs-Tz in the volume, indicating that no displacement occurred (**Figure 4.13d**). Taken together, our results show that hijacking CD11b+ cells by the CRAIT strategy allows drugs to be delivered to hypoxic regions deep inside tumors. Furthermore, the amount of payload accumulated in the tumor using the CRAIT strategy is as large as passive targeting.

We examined the therapeutic efficacy of the CRAIT strategy against an orthotopic 4T1 tumor model. 4T1 tumor-bearing mice were treated with (1) PBS, (2) DOX as free drug, (3) the CRAIT method without DOX

(anti-CD11b-TCO/MSNs-Tz), (4) nontargeted MSNs-Tz with DOX (PBS/MSNs-Tz(DOX)), or (5) the CRAIT method with DOX (anti-CD11b-TCO/MSNs-Tz(DOX)). The amounts of DOX in four groups are equivalent at 5 mg kg^{-1}, and all mice received a total of four treatments once every 3 days (**Figure 4.15a**). Neither mice treated with free DOX nor with the CRAIT method without DOX had an effect on tumor progression. Notably, the nontargeted MSNs-Tz with DOX, which are mainly delivered by the EPR effect, failed to inhibit tumor growth during the therapy because the nontargeted MSNs-Tz are heterogeneously distributed at tumor periphery with limited penetration. By contrast, treatment with the CRAIT method with DOX induced a ~2-fold reduction in tumor burden relative to free DOX or untreated mice (**Figure 4.15b**). These results demonstrate that the CRAIT method enhances the therapeutic efficacy of DOX. $CD11b^+$ cells, which act as drug carriers, deliver DOX molecules deep inside the tumors, exposing large number of tumor cells to DOX molecules. Through tissue histology, we found no significant *in vivo* toxicity in the CRAIT method. Healthy mice injected with PBS or the CRAIT probe (anti-CD11b-TCO and MSNs-Tz) showed no inflamed foci or toxic damages in any of the major organs (**Figure 4.15c**). Furthermore, serum measurements, which are

indicative of liver and kidney toxicities, fell within the range of healthy animals, demonstrating the lack of toxicity at any time point (**Figure 4.15d**). Thus, the CRAIT method significantly improved the efficacy of DOX without toxic side effects.

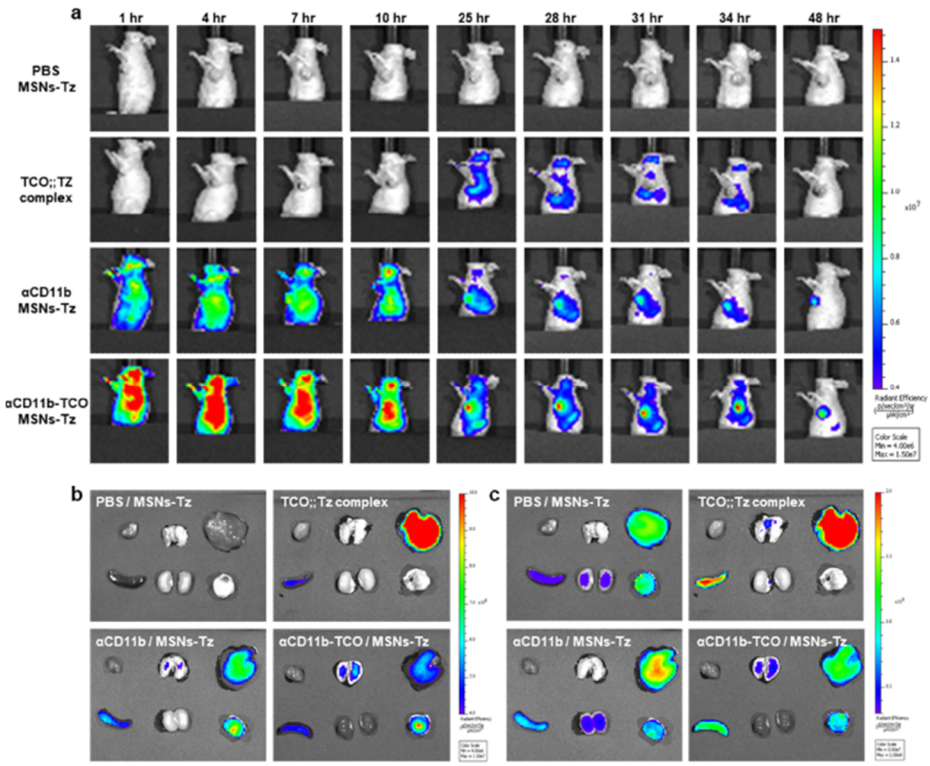

Figure 4.11 (a) Time-gated whole-body fluorescence images of orthotopic 4T1 tumor-bearing mice injected with AF50-labeled anti-CD11b-TCO and Cy5-labeled MSNs-Tz. *Ex vivo* fluorscence imaging of (b) anti-CD11b and (c) MSNs-Tz in major organs excised from mice bearing subcutaneous 4T1 tumors 48 h after injection of anti-CD11b and 24 h after injection of MSNs.

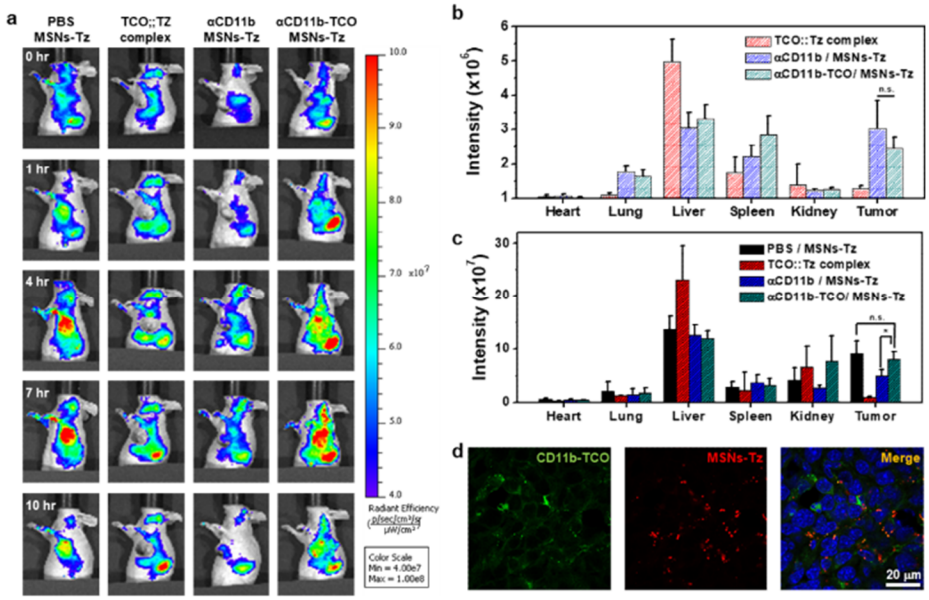

Figure 4.12 (a) Time-dependent *in vivo* fluorescence imaging showing the tumor accumulation of MSNs-Tz. *Ex vivo* biodistribution of (b) anti-CD11b and (c) MSNs-Tz obtained from the fluorescence intensity in each organ 48 h and 24 h after i.v. injection, respectively. (d) *Ex vivo* CLSM images of tumor tissues obtained from mice injected with the CRAIT strategy probes.

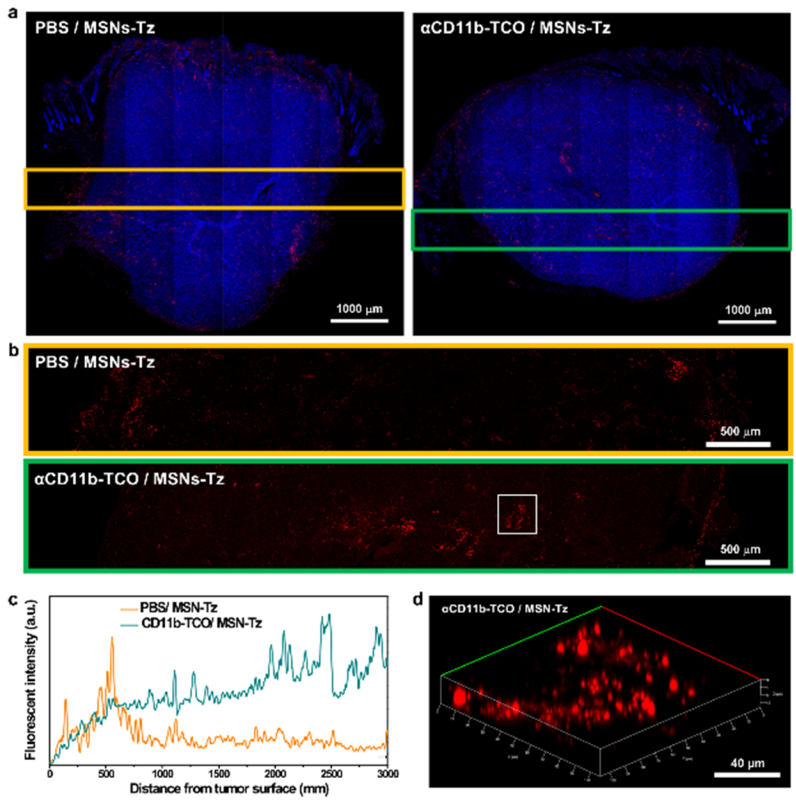

Figure 4.13 (a) Fluorescence images correspond to a low magnification map of a 17 μm thick sagittal cut of 4T1 tumor after intravenous injection of PBS and MSNs-Tz (non-targeted group, left), or the CRAIT strategy probes (anti-CD11b-TCO and MSNs-Tz, right). (b) High magnification images showing MSNs-Tz (red dots) in the tumor regions marked with orange and green rectangles in (a). (c) Fluorescence intensity profiles of MSNs-Tz distributed in the peripheral regions of tumors. (d) 3D CLSM image of the tumor section marked by white square in (b).

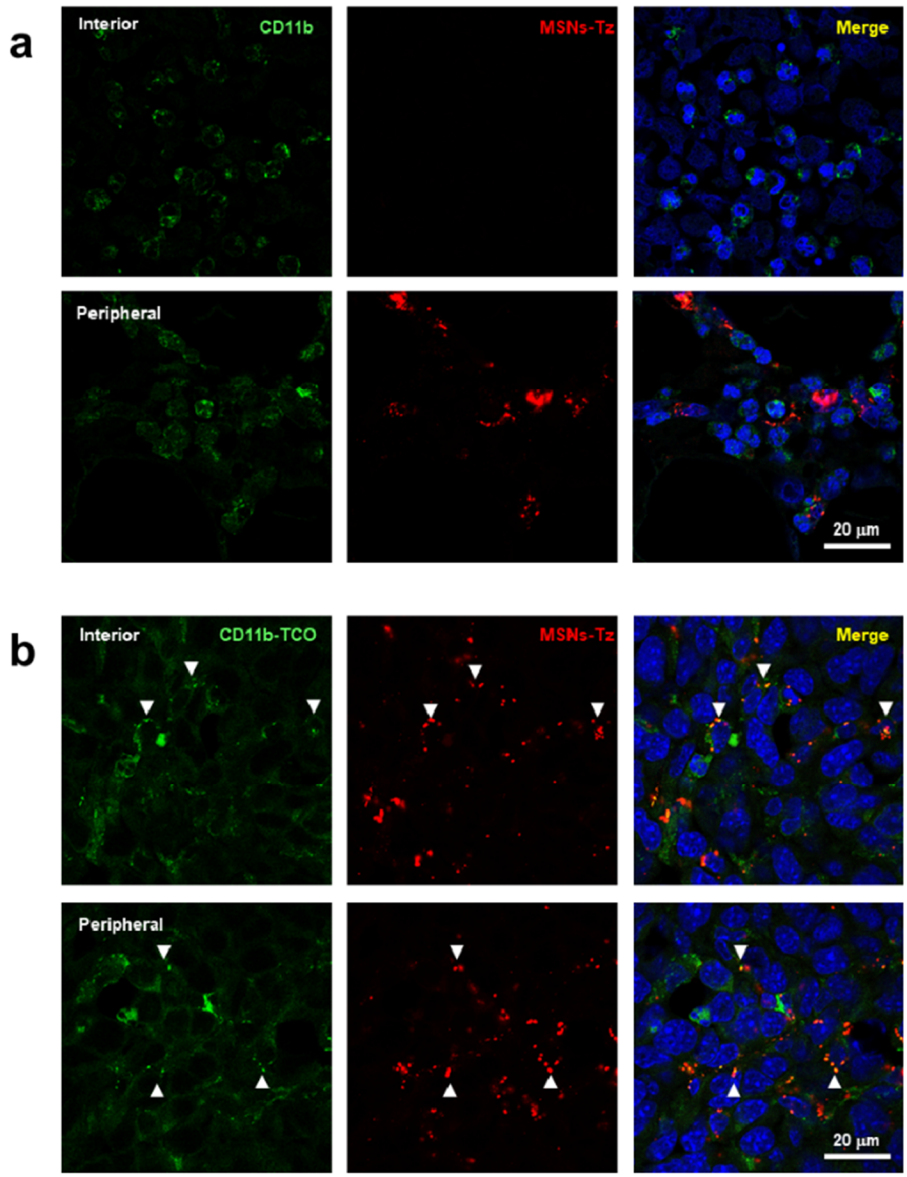

Figure 4.14 *Ex vivo* fluorescence images obtained from tumor tissues in (a) TCO-omitting group and (b) CRAIT group.

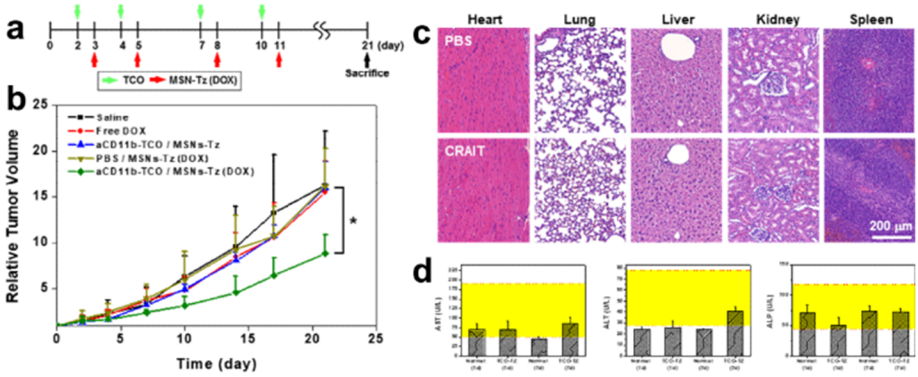

Figure 4.15 (a) Schedule for 4T1 cancer treatment based on the CRAIT strategy. Mice were inoculated with 4T1-Luc2 cells at mammary gland on day 0 and then received four treatments of each group. (b) Tumor growth inhibition by the CRAIT strategy in 4T1 tumors. (c) H&E-stained tissues from major organs 7 days after treatment with the CRAIT strategy probes show no detectable changes compared to healthy control mice (n=5). (d) On day 1 and 7 after administration, serum was collected to investigate the toxicity of the CRAIT strategy on liver function including AST, ALT, and ALP. Yellow regions indicate reference healthy ranges.

4.4 Conclusion

In summary, we have developed an anti-cancer drug delivery system using autologous myeloid cells as "Trojan horses" to enhance the therapeutic potential of DOX for aggressive breast cancer treatment. We demonstrate that pretargeting of TCO-conjugated CD11b antibodies to $CD11b^+$ myeloid cells in blood vessels and tumors leads to *in vivo* conjugation of MSNs-Tz via bioorthogonal click chemistry. By exploiting the intrinsic homing ability of $CD11b^+$ myeloid cells to infiltrate tumor interiors, the $CD11b^+$ cell-mediated delivery enables NPs to penetrate tumors more deeply (up to 2.5 mm deep) compared to traditional targeting strategies (100-300 μm deep). The "Trojan horse" approach reduced tumor burden significantly after four treatments, whereas free DOX and DOX-loaded MSNs alone were ineffective. Unlike conventional adoptive cell transfer methods that require complicated *ex vivo* labeling, the CRAIT method only requires simple modification of antibodies using well-known bioconjugate chemistries and two intravenous injections during the treatment.

**Most of the contents of this chapter were published in the article, “Enhanced tumor penetration of drug-loaded nanoparticles by click reaction-assisted immune cell targeting strategy.” (*In preparation.*)

4.5 References

[1] Wilhelm, S.; Tavares, A. J.; Dai, Q.; Ohta, S.; Audet, J.; Dvorak, H. F.; Chan, W. C. W., *Nature Reviews Materials* **2016,** *1*, 16014.

[2] Bertrand, N.; Wu, J.; Xu, X.; Kamaly, N.; Farokhzad, O. C., *Advanced Drug Delivery Reviews* **2014,** *66*, 2.

[3] Prabhakar, U.; Maeda, H.; Jain, R. K.; Sevick-Muraca, E. M.; Zamboni, W.; Farokhzad, O. C.; Barry, S. T.; Gabizon, A.; Grodzinski, P.; Blakey, D. C., *Cancer Research* **2013,** *73*, 2412.

[4] Cabral, H.; Matsumoto, Y.; Mizuno, K.; Chen, Q.; Murakami, M.; Kimura, M.; Terada, Y.; Kano, M. R.; Miyazono, K.; Uesaka, M.; Nishiyama, N.; Kataoka, K., *Nature Nanotechnology* **2011,** *6*, 815.

[5] Farokhzad, O. C.; Langer, R., *ACS Nano* **2009,** *3*, 16.

[6] Wong, C.; Stylianopoulos, T.; Cui, J.; Martin, J.; Chauhan, V. P.; Jiang, W.; Popović, Z.; Jain, R. K.; Bawendi, M. G.; Fukumura, D., *Proceedings of the National Academy of Sciences* **2011,** *108*, 2426.

[7] Waite, C. L.; Roth , C. M., **2012,** *40*, 21.

[8] Chauhan, V. P.; Jain, R. K., *Nature Materials* **2013,** *12*, 958.

[9] Su, Y.; Xie, Z.; Kim, G. B.; Dong, C.; Yang, J., *ACS Biomaterials Science & Engineering* **2015,** *1*, 201.

[10] Hanahan, D.; Coussens, Lisa M., *Cancer Cell* **2012,** *21*, 309.

[11] Xue, J.; Zhao, Z.; Zhang, L.; Xue, L.; Shen, S.; Wen, Y.; Wei, Z.; Wang, L.; Kong, L.; Sun, H.; Ping, Q.; Mo, R.; Zhang, C., *Nature Nanotechnology* **2017,** *12*, 692.

[12] He, X.; Cao, H.; Wang, H.; Tan, T.; Yu, H.; Zhang, P.; Yin, Q.; Zhang, Z.; Li, Y., *Nano Letters* **2017,** *17*, 5546.

[13] Choi, M.-R.; Stanton-Maxey, K. J.; Stanley, J. K.; Levin, C. S.; Bardhan, R.; Akin, D.; Badve, S.; Sturgis, J.; Robinson, J. P.; Bashir, R.; Halas, N. J.; Clare, S. E., *Nano Letters* **2007,** *7*, 3759.

[14] Huang, B.; Abraham, W. D.; Zheng, Y.; Bustamante López, S. C.; Luo, S. S.; Irvine, D. J., *Science Translational Medicine* **2015,** *7*, 291ra94.

[15] Gabrilovich, D. I.; Nagaraj, S., *Nature Reviews Immunology* **2009,** *9*, 162.

[16] Bayne, Lauren J.; Beatty, Gregory L.; Jhala, N.; Clark, Carolyn E.; Rhim, Andrew D.; Stanger, Ben Z.; Vonderheide, Robert H., *Cancer Cell* **2012,** *21*, 822.

[17] Corzo, C. A.; Condamine, T.; Lu, L.; Cotter, M. J.; Youn, J.-I.; Cheng, P.; Cho, H.-I.; Celis, E.; Quiceno, D. G.; Padhya, T.; McCaffrey, T. V.; McCaffrey, J. C.; Gabrilovich, D. I., *The Journal of Experimental Medicine* **2010,** *207*, 2439.

[18] Kelly, P. M.; Davison, R. S.; Bliss, E.; McGee, J. O., *British Journal of Cancer* **1988,** *57*, 174.

[19] Miller, M. A.; Zheng, Y.-R.; Gadde, S.; Pfirschke, C.; Zope, H.; Engblom, C.; Kohler, R. H.; Iwamoto, Y.; Yang, K. S.; Askevold, B.; Kolishetti, N.; Pittet, M.; Lippard, S. J.; Farokhzad, O. C.; Weissleder, R., *Nature Communications* **2015,** *6*, 8692.

[20] Rosenberg, S. A.; Restifo, N. P., *Science* **2015,** *348*, 62.

[21] Marrache, S.; Tundup, S.; Harn, D. A.; Dhar, S., *ACS Nano* **2013,** *7*, 7392.

[22] Pillay, J.; den Braber, I.; Vrisekoop, N.; Kwast, L. M.; de Boer, R. J.; Borghans, J. A. M.; Tesselaar, K.; Koenderman, L., *Blood* **2010,** *116*, 625.

[23] Segers, V. F. M.; Lee, R. T., *Nature* **2008,** *451*, 937.

[24] Jewett, J. C.; Bertozzi, C. R., *Chemical Society Reviews* **2010,** *39*, 1272.

[25] Kolb, H. C.; Sharpless, K. B., *Drug Discovery Today* **2003,** *8*, 1128.

[26] Devaraj, N. K.; Weissleder, R., *Accounts of Chemical Research* **2011,** *44*, 816.

[27] Heebeom, K.; Sangmin, L.; Hee, N. J.; Hwa, K. S.; Kwang, H. S.; Kuiwon, C.; Chan, K. I.; Young, J. S.; Kwangmeyung, K., *Angewandte Chemie International Edition* **2012,** *51*, 11836.

[28] Xie, R.; Dong, L.; Du, Y.; Zhu, Y.; Hua, R.; Zhang, C.; Chen, X., *Proceedings of the National Academy of Sciences* **2016,** *113*, 5173.

[29] Hua, W.; Marianne, G.; R., K. J.; J., M. R.; Ming, X.; D., O. B. W.; Jianjun, C., *Angewandte Chemie International Edition* **2016,** *55*, 5452.

[30] Devaraj, N. K.; Thurber, G. M.; Keliher, E. J.; Marinelli, B.; Weissleder, R., *Proceedings of the National Academy of Sciences* **2012,** *109*, 4762.

[31] Raffaella, R.; Pascal, R. V.; M., v. d. B. S.; M., V. R. C.; Iris, V.; Johan, L.; S., R. M., *Angewandte Chemie International Edition* **2010,** *49*, 3375.

[32] Pack, C. G.; Song, M. R.; Lee Tae, E.; Hiroshima, M.; Byun, K. H.; Kim, J. S.; Sako, Y., *Journal of Controlled Release* **2012,** *163*, 315.

[33] Youn, J.-I.; Kumar, V.; Collazo, M.; Nefedova, Y.; Condamine, T.; Cheng, P.; Villagra, A.; Antonia, S.; McCaffrey, J. C.; Fishman, M.; Sarnaik, A.; Horna, P.; Sotomayor, E.; Gabrilovich, D. I., *Nature Immunology* **2013,** *14*, 211.

[34] Kettling, U.; Koltermann, A.; Schwille, P.; Eigen, M., *Proceedings of the National Academy of Sciences* **1998,** *95*, 1416.

[35] Schwille, P.; Meyer-Almes, F. J.; Rigler, R., *Biophysical Journal* **1997,** *72*, 1878.

[36] Zhou, H.; Liao, J.; Aloor, J.; Nie, H.; Wilson, B. C.; Fessler, M. B.; Gao, H.-M.; Hong, J.-S., *The Journal of Immunology* **2013,** *190*, 115.

[37] van Spriel, A. B.; Leusen, J. H. W.; van Egmond, M.; Dijkman, H. B. P. M.; Assmann, K. J. M.; Mayadas, T. N.; van de Winkel, J. G. J., *Blood* **2001,** *97*, 2478.

[38] Matsumoto, Y.; Nichols, J. W.; Toh, K.; Nomoto, T.; Cabral, H.; Miura, Y.; Christie, R. J.; Yamada, N.; Ogura, T.; Kano, M. R.; Matsumura, Y.;

Nishiyama, N.; Yamasoba, T.; Bae, Y. H.; Kataoka, K., *Nature Nanotechnology* **2016,** *11*, 533.

[39] Nagy, J. A.; Chang, S. H.; Dvorak, A. M.; Dvorak, H. F., *British Journal of Cancer* **2009,** *100*, 865.

[40] Nishiyama, K.; Nakashima, H.; Ikarashi, M.; Kinoshita, M.; Nakashima, M.; Aosasa, S.; Seki, S.; Yamamoto, J., *PLOS ONE* **2015,** *10*, e0136774.

[41] Arnaout, M., *Blood* **1990,** *75*, 1037.

[42] von zur Muhlen, C.; von Elverfeldt, D.; Bassler, N.; Neudorfer, I.; Steitz, B.; Petri-Fink, A.; Hofmann, H.; Bode, C.; Peter, K., *Atherosclerosis* **2007,** *193*, 102.

[43] Miller, M. A.; Gadde, S.; Pfirschke, C.; Engblom, C.; Sprachman, M. M.; Kohler, R. H.; Yang, K. S.; Laughney, A. M.; Wojtkiewicz, G.; Kamaly, N.; Bhonagiri, S.; Pittet, M. J.; Farokhzad, O. C.; Weissleder, R., *Science Translational Medicine* **2015,** *7*, 314ra183.

Bibliography

1. Journal Publication

1) **Jonghoon Kim** (*co-first author*), **Han Young Kim**, Seuk Young Song, Seok-hyeong Go, Hee Su Sohn, Seungmin Baik, Min Soh, Hyo-Cheol Kim, Nohyun Lee, Byung-Soo Kim, Taeghwan Hyeon

"Synergistic Oxygen Generation and ROS Scavenging by Nanoparticles of Manganese Ferrite and Ceria Induce M2 Polarization of Macrophages for Rheumatoid Arthritis Treatment."

ACS Nano **2019**, in revision.

2) **Soo Hong Lee**, **Ok Kyu Park**, **Jonghoon Kim** (*co-first author*), Kwangsoo Shin, Chan Gi Pack, Nohyun Lee, Seung-Hae Kwon, Taeghwan Hyeon

"Enhanced Tumor Penetration of Drug-Loaded Nanoparticles by Click Reaction-Assisted Immune Cell Targeting Strategy."

2019, in preparation.

3) Vinayak S. Kale, Minsik Hwang, Hogeun Chang, Jeongmin Kang, Sue In Chae, Youngmoo Jeon, Jiwoong Yang, **Jonghoon Kim**, Yoon-Joo Ko, Yuanzhe Piao, Taeghwan Hyeon

"Microporosity-Controlled Synthesis of Heteroatom Codoped Carbon Nanocages by Wrap-Bake-Sublime Approach for Flexible All-Solid-State-Supercapacitors."

Adv. Funct. Mater. **2018**, *28*, 1803786.

4) Dokyoon Kim, **Jonghoon Kim**, Yong Il Park, Nohyun Lee, Taeghwan Hyeon

"Recent Development of Inorganic Nanoparticles for Biomedical Imaging."

ACS Cent. Sci. **2018**, *4*, 324.

5) Hyek Jin Kwon, Kwangsoo Shin, Min Soh, Hogeun Chang, **Jonghoon Kim**, Jisoo Lee, Giho Ko, Byung Hyo Kim, Dokyoon Kim, Taeghwan Hyeon

"Large-Scale Synthesis and Medical Applications of Uniform-Sized

Metal Oxide Nanoparticles."

Adv. Mater. **2018**, *30*, 1704290.

6) **Jonghoon Kim**, Nohyun Lee, Taeghwan Hyeon

"Recent Development of Nanoparticles for Molecular Imaging."

Phil. Trans. R. Soc. A **2017**, *375*, 20170022.

7) **Jonghoon Kim**, Hye Rim Cho, Hyejin Jeon, Dokyoon Kim, Changyeong Song, Nohyun Lee, Seung Hong Choi, Taeghwan Hyeon

"Continuous O_2-Evolving $MnFe_2O_4$ Nanoparticle-Anchored Mesoporous Silica Nanoparticles for Efficient Photodynamic Therapy in Hypoxic Cancer."

J. Am. Chem. Soc. **2017**, *139*, 10992.

8) Yang Lu, Yun-Jun Xu, Guo-bing Zhang, Daishun Ling, Ming-quan Wang, Yong Zhou, Ya-Dong Wu, Tao Wu, Michael J. Hackett, Byung Hyo Kim, Hogeun Chang, **Jonghoon Kim**, Xin-Tian Hu, Liang Dong, Nohyun Lee, Fangyuan Li, Jia-Cai He, Li Zhang, Hui-Qin Wen, Bo Yang, Seung Hong Choi, Taeghwan Hyeon, Duo-Hong Zhou

"Iron Oxide Nanoclusters for T_1 Magnetic Resonance Imaging of Non-Human Primates."

Nat. Biomed. Eng. **2017**, *1*, 637.

9) Donghee Son, Jongha Lee, Dong Jun Lee, Roozbeh Ghaffari, Sumin Yun, Seok Joo Kim, Ji Eun Lee, Hye Rim Cho, Soonho Yoon, Shixuan Yang, Seunghyun Lee, Shutao Qiao, Daishun Ling, Sanghun Shin, Jun-Kyul Song, Jaemin Kim, Taeho Kim, Hakyong Lee, **Jonghoon Kim**, Min Soh, Nohyun Lee, Cheol Seong Hwang, Sangwook Nam, Nanshu Lu, Taeghwan Hyeon, Seung Hong Choi, Dae-Hyeong Kim

"Bioresorbable Electronic Stent Integrated with Therapeutic Nanoparticles for Endovascular Diseases"

ACS Nano, **2015**, *9*, 5937.

2. International Conference Presentation

1) **Jonghoon Kim**, Nohyun Lee, Seung Hong Choi, Taeghwan Hyeon
"Oxygen-Generating Manganese Ferrite Nanoparticles for Enhanced Therapeutic Efficiency of Photodynamic Therapy in Hypoxic Cancer"
2018 MRS Spring Meeting & Exhibit, Phoenix, USA, April 2-6, 2018

2) **Jonghoon Kim**
"Continuously Oxygen-Evolving MnFe2O4 Nanoparticle-Anchored Mesoporous Silica Nanoparticles for Efficient Photodynamic Therapy in Hypoxic Cancer"
The 10th International Conference on Advanced Materials and Devices (ICAMD) 2017, Jeju, Korea, December 5-8, 2017

3) Dong Jun Lee, **Jonghoon Kim**, Dae-Hyeong Kim, Taeghwan Hyeon
"Biodegradable Stent Integrated with Therapeutic Nanoparticles and Electronic Device for Endovascular Diseases"
IUPAC 2015, Busan, Korea, August 9-14, 2015

초 록

무기 나노입자는 특유의 우수한 물리화학적 특성으로 인해 미래 생의학 분야의 새로운 이미징, 진단 및 치료제로 각광받고 있다. 특히, 다양한 조합의 무기 나노입자를 이용하면 신체의 질병 부위에서 발견되는 저산소 염증성 미세환경을 쉽게 조절할 수 있다. 촉매 무기 나노입자는 저산소성 환경에서 세포 내의 과산화수소를 이용하여 지속적으로 산소를 생성할 수 있을 뿐만 아니라, 염증성 미세환경에서 대식세포의 표현형을 조절하여 조직의 염증을 완화시킬 수 있다. 또한 표적화 분자가 결합된 기능성 나노입자를 사용하면 면역 세포를 쉽게 표적화 할 수 있어, 염증성 미세환경으로 다양한 기능을 가진 나노입자를 전달할 수 있다. 이 학위 논문에서는 저산소 염증성 미세환경의 조절을 위한 다기능성 무기 나노입자의 응용에 대해 기술하였다.

첫 번째로, 망간 산화철 나노입자와 다공성 실리카 나노입자를 결합하여 종양 내의 저산소증을 완화시키고 암

치료법 중 하나인 광역학 치료법의 효율을 크게 증대시켰다. 망간 산화철 나노입자가 펜톤 반응을 통해 산소를 지속적으로 생성할 수 있다는 특성을 이용하여 종양 세포 내의 저산소 환경을 완화시킬 수 있었다. 또한, 나노입자의 자기적 성질로 인해 자기공명영상 (MRI)을 이용한 생체 내의 추적이 가능하였다.

두 번째로, 망간 산화철 나노입자와 세리아 나노입자의 시너지 효과를 이용해 대식세포의 표현형을 M1 형에서 M2 형으로 유도하여 류마티스 관절염의 치료효과를 확인하였다. 망간 산화철의 펜톤 반응 중에 발생하는 하이드록실 라디칼을 세리아 나노입자가 제거해주는 효과로 인해, 산소 발생과 활성산소 제거를 더욱 효율적으로 실행할 수 있었다. 이를 류마티스 관절염을 앓는 실험 쥐에 투여해 저산소증, 염증의 완화 및 여러 병리학적 특성들이 개선됨을 확인하였다.

마지막으로, 약물이 들어있는 나노입자를 종양 내부로 전달하기 위한 클릭 반응을 이용한 면역 세포 표적화 전략을 개발하였다. 면역 세포를 표적화할 수 있는 CD11b 항체와 다공성 실리카 나노입자에 각각 클릭 반응이 가능한 분자를 결합시켜, 생체 내에서 이들의 클릭 반응을 가능하게 하였다. 24시간 간격으로 항체와 나노입자를 주입하여 면역 세포를

성공적으로 표적화하였고, 이를 이용해 기존의 방법으로는 힘들었던 나노입자의 깊은 종양 조직으로의 침투를 확인하였다. 이 전략을 이용하여 약물이 들어있는 나노입자를 유방암을 앓는 실험 쥐에 투여했을 때 더 효과적으로 종양의 성장을 억제함을 확인하였다.

주요어: 나노입자, 약물전달, 암 치료, 종양 저산소증, 클릭 반응, 나노의학

학번: 2013-22521